5-2019

Time-Lapse Monitoring of Two-Dimensional Non-Uniform Unsaturated Flow Processes Using Ground Penetrating Radar

Blake Lytle
Clemson University, balytle@g.clemson.edu

TIME-LAPSE MONITORING OF TWO-DIMENSIONAL NON-UNIFORM UNSATURATED FLOW PROCESSES USING GROUND PENETRATING RADAR

A Thesis
Presented to
the Graduate School of
Clemson University

In Partial Fulfillment
of the Requirements for the Degree
Master of Science
Hydrogeology

---

by
Blake Andrew Lytle
May 2019

Accepted by:
Dr. Ronald W. Falta, Committee Chair
Dr. Stephen M.J. Moysey
Dr. Christophe J.G. Darnault

ABSTRACT

Unsaturated flow in the vadose zone often manifests as preferential flow resulting in transport of water and solutes through the soil much faster than would occur for uniform matrix flow. Time-lapse ground penetrating radar (TLGPR) shows promise as a non-invasive means to monitor unsaturated flow and here is used to monitor lab-scale forced infiltration events for capturing evidence of non-uniform and preferential flow phenomena directly from arrivals in the GPR images while simultaneously characterizing parameters of the flow system, such as bulk water content and rates of wetting front movement. This was accomplished by 1) directly interpreting transient arrivals in GPR profiles for evidence of ono-uniform flow and 2) with the aid of migration processing techniques to improve the quality of GPR images for identification and tracking of transient arrivals related to wetting in the soil. A novel method is described and evaluated to characterize the 2D velocity structure of a soil and used to migrate the GPR images. This method incorporates multi-offset measurements to characterize the depth to a potentially unknown static reflector and root mean square (RMS) velocity above the reflector with incremental changes in travel time to the static reflector and a transient reflector (i.e. the wetting front) determined from single-offset constant offset profiles to determine incremental changes in velocity above and below the transient arrival. The method is applied to TLGPR data during infiltration experiments in a 60 cm deep sand-filled tank and monitored with water content probes. To verify the approach the methodology is applied to GPR data simulated using transient water contents generated by the unsaturated flow simulator HYDRUS 2D given lab-measured hydraulic properties

of the soil. For both the empirical and simulated data, we found that the 2D velocity analysis was effective in monitoring changes in the wetting front and that migration of the reflection profiles was able to improve the interpretation of non-uniform flow.

DEDICATION

For Lorraine and Ralph, Farrel and Manetta.

TABLE OF CONTENTS

Page

Table of Contents (Continued) Page

LIST OF TABLES

LIST OF FIGURES

List of Figures (Continued)

Figure Page

CHAPTER 1

GROUND PENETRATING RADAR FOR NON-INVASIVE MONITORING OF HYDROLOGIC PROCESSES IN THE VADOSE ZONE

1.1 Background and Motivation

Unsaturated flow through the vadose zone involves the interaction of multiple phases and is influenced by capillary forces. As a result, flow and transport of fluids is strongly influenced by the exact shape, arrangement, and connectivity of pore spaces. Variability in the porous matrix can cause preferential flow to occur, which is defined as "all phenomena where water and solute move along certain pathways, while bypassing a fraction of the porous matrix" (Hendrickx et al., 2001). Preferential flow is caused primarily by three factors: the presence of pores with dimensions much larger than within the rest of the medium (macropores), the lateral redirection of downward-moving water along inclined layers and boundaries (funnel flow), and the development of unstable flow due to air entrapment, which can cause a flat wetting front to separate into individual "fingers" (Hendrickx et al., 2001). Models of unsaturated flow in a homogenous medium, such as those based on the Richards equation (Richards, 1931), predict that wetting fronts will be horizontal and uniform, yet unstable flow is a common feature of laboratory and field studies (Geiger and Durnford, 2000; Hendrickx et al., 1993; Selker et al., 1992; Yao and Hendrickx, 1996). Unstable flow within a homogenous medium cannot be predicted with classic flow models based on the Richards equation (Richards, 1931). It is similarly difficult to monitor flow (preferential or matrix) *in situ*. Instruments which describe

hydrologic conditions (e.g. gravimetric water content sensors, TDR probes, soil matric potential sensors, tensiometers) or estimate unsaturated hydraulic conductivity do so at point locations, and the distribution of parameters between sampling points is unknown (Vereecken et al., 2008). Preferential pathways, such as macropores or funneling features, may not be properly identified or sampled from punctual measurements, or the natural soil conditions may be disrupted when installing such instruments.

The transport of water and solutes along preferential pathways is consequential in many areas of concern. The impact on ecosystem functions and health can be evaluated by thinking of soil as a filter for ground and surface water, and the ability of a soil to act as a filter is altered by preferential flow. In this case, Clothier, et. al. found that certain ecosystem functions benefit from preferential flow at a value of $304 billion dollars annually, while others functions were negatively impacted by preferential flow processes (Clothier et al., 2008). Models of aquifer recharge which neglect the influence of preferential flow have been shown to be erroneous. In one case, recharge assumed to originate as uniform unsaturated flow is inconsistent with groundwater level measurements in tropical Uganda and preferential flow mechanisms are thought to be the controlling factor in recharge (Cuthbert and Tindimugaya, 2010). The recharge occurring within semi-arid aquifers along preferential pathways was found in two cases in India to be at least as important as the dominant mechanism (Sukhija et al., 2000) and comprised 33%-75% of the total recharge (Sukhija et al., 2003) and may be as much as 90% of total (de Vries and Simmers, 2002). The significance for societies in semi-arid regions assessing sustainability of agricultural practices, thus, is quite high (Sukhija et al., 2003).

The use of fertilizers and pesticides on agricultural lands can have a significant impact on surface and ground water quality as the nutrients and chemicals are transported along preferential pathways. The study of Perkins, et. al., determined that 43% of recharge in an agricultural field in Mississippi was as fingers (Perkins et al., 2011), resulting in greater chemical loading of the underlying aquifer than previously thought. Hendrickxs et al. found during natural precipitation experiments that non-reactive tracer concentrations in groundwater were 6 to 13 times higher under unstable flow conditions than the stable flow case (Hendrickx et al., 1993).

The limited sampling from standard hydrologic sampling methods has necessitated the development of methods for monitoring *in situ* flow at larger scales. Geophysical methods which are sensitive to subsurface contrasts in electrical properties have been frequently applied to describe hydrologic conditions in the soil and as a way of monitoring flow and calibrating flow model parameters. Ground penetrating radar (GPR), in particular, has been utilized due to its sensitivity to variability in the subsurface volumetric water content. Surface-based GPR surveys are performed by generating an electromagnetic (EM) wave with a source antenna located on the ground surface which propagates into the ground. Energy which is directly transmitted to a receiver antenna as well as reflected from interfaces with contrasting electrical properties is sampled in time (Jol, 2009). Methods which use GPR data to quantitatively describe subsurface water content do by estimating the velocity of the EM wave and have been the focus of numerous studies, with an excellent summary from Huisman et al., (2003). The wave velocity in the subsurface is a function of the electromagnetic properties: electrical

conductivity (σ), magnetic permeability (μ), and dielectric permittivity (ε). In scenarios where electrical conductivity is high, the emitted energy dissipates and the low signal penetration makes GPR ineffective. Therefore, GPR is often utilized when earth materials are generally non-conductive and non-magnetic, in which case the wave velocity (V) is related to the real part of the relative dielectric permittivity (ε) by:

$$V = \frac{c}{\sqrt{\varepsilon}} \tag{1.1}$$

where c is the speed of light in a vacuum. As the relative permittivity of air is 1, mineral grains generally from 3-10, and water is 81 (Buchner et al., 1999), the material permittivity is strongly related to the volumetric water content in unsaturated materials and porosity in saturated materials. Additionally, contrasts in the water content of materials create strong permittivity contrasts which manifest as reflections in the GPR data. Petrophysical relationships can then be used which relate the water content (θ) of the medium from the relative permittivity, such as the well-known Topp equation (Topp et al., 1980).

The wave velocity and bulk water content can be estimated using surface-based GPR with a variety of methods, each with unique advantages and limitations. When a single antenna separation, or offset, is used, the velocity can be determined if a reflecting interface at a known depth is contained within the profiled area (Grote et al., 2005; Lunt et al., 2005; Stoffregen et al., 2002). This method is limited by the spatial distribution of

reflecting interfaces with known depth. However, data can often be rapidly collected by use of equipment which keeps the antennas at a fixed offset as they are moved. Another method of velocity analysis uses the collection of data with multiple source-receiver offsets, which has been successfully used to characterize soil moisture in a variety of scenarios (Becht et al., 2006; Garambois et al., 2002; Jacob and Hermance, 2004; Steelman and Endres, 2012; Steelman et al., 2012; Turesson, 2006). The multi-offset method allows for reflector depth to be determined from the analysis directly, but accurately positioning the antennas is significantly more time- and labor-intensive than the constant offset method. Multi-offset data analysis incorporates assumptions about subsurface geometry, such as reflecting interfaces are horizontal, the ratio between offset and reflector depth is small, and velocity within a layer is uniform (Yilmaz, 2001).

Time-lapse GPR (TLGPR) measurements have been utilized to characterize changes in subsurface water content and estimate hydraulic parameters of soils in a variety of spatial scales. A multi-year study which characterized water content and vadose zone dynamics was performed by Steelman et al., (2012) which assessed seasonal and annual variations in the arrival time of reflectors in single-offset data to infer changes in the volumetric water content and used multi-offset velocity estimation methods to characterize fluctuations in velocities between reflecting interfaces to estimate vertical soil water fluxes. Steelman and Endres (2012) collected multi-offset GPR data using several antennas of varying frequency (225 MHz, 450 MHz, 900 MHz) to monitor the seasonal changes in vertical moisture distribution in a sand, sandy loam, and silt loam and to assess the trade-off between signal penetration and image resolution and the

consequent impact on soil moisture estimates. They were able to delineate intervals of variable velocity to the decimeter scale and noted higher frequency antennas were better able to resolve velocity variations. Moysey (2010) showed that wetting and drying events in homogenous sand created distinct transient arrivals in time-lapse GPR traces. The author used the trajectory of these arrivals through the time-lapse data to constrain an unsaturated flow model to determine the hydraulic parameters. The work of Mangel et al. (2012) demonstrates how automation of antenna placement could enable rapid time-lapse estimates of bulk water content every 30-60 seconds during single infiltration events with good agreement to water content probe measurements ($\leq$ 0.03 vol/vol). The authors identified transient arrivals in the GPR data associated with wetting of the soil were and demonstrated how multiple projections of the data (multi-offset and time-lapse constant offset plots) enhanced interpretation of GPR images (Mangel et al., 2012).

The collection of TLGPR data has been demonstrated as a viable method to monitor dynamic hydrologic processes, such as infiltration, by analyzing changes in replicate data sets. The potential for tracking of wetting fronts and inferring preferential flow has been long recognized. Vellidis et al. (1990) describe a forced infiltration experiment into sands of the Georgia Coastal Plain and tracked the wetting front with GPR for 25 hours and note the possibility of identifying preferential flow paths, but did not observe any occurrence in their data. Truss, et al. (2007) performed an infiltration experiment into the Miami limestone and observed a number of diffraction features in the GPR data. The authors attributed diffractions to preferential flow through the root zone, rubble, and dissolution fingers in the unsaturated rock. A dye-tracer experiment was performed by

Haarder, et al. (2011) in sandy deposits in which fingered flow was observed in the dye-stain patterns in excavated trenches following infiltration. The authors simulated the GPR response from an unstable front and flow fingers, but these features were not observed in the data collected during infiltration. Recently, Allroggen, et al. (Allroggen et al., 2015) performed a similar dye-staining experiment and observe flow fingers in the excavated soil cross-sections but no not report detection of fingered flow in the GPR data. Increases in the travel time to specific reflecting interfaces were interpreted to be caused by the preferential movement of water and verified in the observed dye-staining.

These studies demonstrate the mixed success of detecting preferential flow using GPR. Analysis of patterns in the GPR data, such as travel time shifts, has suggested preferential flow yet the limitations in temporal sampling and image resolution prevent individual fingers related to non-uniform or preferential flow from being imaged directly. Discrete sub-wavelength features (e.g. flow fingers) scatter energy and manifest in GPR profiles as diffraction hyperbolas, such as those observed by Truss, et al. (2007), which can obscure the image and hinder interpretation. The interpretability of infiltration images may be improved by post-processing of GPR data using migration methods which relocate recorded energy to its true subsurface position and collapse diffraction hyperbolas (Yilmaz, 2001). Migration may also be a viable method of converting the GPR profiles from the travel time domain to the depth domain when velocity varies significantly within the profiled area.

TLGPR studies demonstrate a trade-off between their ability to quantitatively describe changes in the bulk water content and capturing non-uniform and preferential

flow features. Multi-offset studies have shown good agreement between instrumental and gravimetric water content sampling and GPR-based estimates but have not imaged preferential flow and neglect its effects by assuming the flow system is 1-D (Mangel et al., 2012; Steelman et al., 2012). Studies attempting to visualize preferential flow have tracked relative changes in water content during infiltration experiments which correlate with the volume of applied water, though remained unable to find direct evidence of preferential flow in the GPR data (Allroggen et al., 2015; Haarder et al., 2011). Truss, et al. (2007) observed scattering in their GPR data indicative of preferential flow and verified presence of unique flow channels but did not quantify the changes in water content of the system.

1.2 Research Objectives

This thesis will investigate the potential for TLGPR for monitoring of non-uniform and preferential flow processes and quantification of system parameters, such as volumetric water content. An automated antenna positioning system is to be used which is expected to help reduce the disparity between quantitatively describing changes to a flow system, such as bulk water content, and capturing evidence of non-uniform and preferential flow phenomena. The following hypotheses are proposed to be tested:

- Evidence for non-uniform and preferential infiltration of water through a homogenous medium can be interpreted directly from arrivals in the time-lapse GPR profiles.

- Migration processing of time-lapse GPR data sets collected during infiltration can improve the interpretation of flow phenomena and quantitatively describe changes in the flow system.
- A single-offset velocity analysis method can be used to determine the velocity structure and bulk water content of the soil under non-uniform flow conditions.
- The velocity structure derived from single-offset analysis can be used to migrate data from the time-domain to depth-domain to quantify flow system parameters, such as wetting front depth.

These hypotheses are to be investigated with lab scale forced-infiltration experiments performed in a vadose zone analog consisting of a sand-filled tank. The tank can be easily fitted with water content probes for characterization of soil moisture during infiltration. The infiltration experiments will be monitored with time-lapse GPR coupled with an automated gantry for rapid and precise positioning of antennas. The empirical TLGPR data will be interpreted for evidence of non-uniform and preferential flow and analyzed to quantify the velocity structure and estimate hydrologic characteristics of the soil during infiltration. Numerical simulations of the experimental conditions will be analyzed using the same methodology as the empirical data to assess the accuracy of the velocity analysis methods developed, the ability of migrated GPR profiles to describe the flow system, and the accuracy of bulk water content estimations.

1.3 Analysis Methods

1.3.1 Fundamentals of Surface-Based GPR Surveys

Surface-based GPR surveys emit an electromagnetic wave in the radio frequency range from a source antenna which travels through the ground, and energy reflected from contrasts in the electrical properties are recorded in time at the receiver antenna (Jol, 2009). Signal paths from the source to the receiver can be conceptualized as rays shown in Figure 1.1. Surveys are performed as either a constant offset profile (COP) or a multi-offset survey as shown in Figure 1.1. During constant offset profiling, the source and receiver antennas are moved along a line with a single, fixed offset and a unique time-series measurement, termed a trace, is recorded at distinct locations. The recorded traces are then plotted with respect to their relative position to generate a 2D image of subsurface reflectivity with time as the vertical axis (typically denoted as travel time). Multi-offset surveys are performed specifically for wave velocity estimation and are not generally interpreted directly. In a common midpoint (CMP) survey, the offset between source and receiver is varied about a central point such that transmitted waves reflect from the same locations. Surface-based GPR surveys rely on the travel time of reflected waves to estimate the subsurface wave velocity. In Figure 1.1, the geometry of a COP and CMP collected over a single layer with a velocity V and reflecting interface at depth of h are shown.

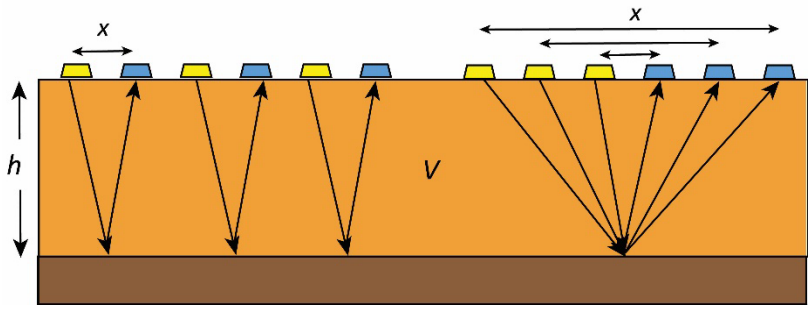

Figure 1.1. Data collection geometry for a constant offset profile (COP) (left) and multi-offset common midpoint (CMP) survey (right).

1.3.2 Velocity Analysis Methods

With single offset data, the velocity can be determined if a reflecting interface at a known depth is contained within the profiled area (Grote et al., 2005; Lunt et al., 2005; Stoffregen et al., 2002). The two-way travel time of the reflected arrival (t) is related to the reflector depth (h), offset (x), and medium velocity (V) by:

$$V = \frac{2\sqrt{h^2 + \left(\frac{1}{2}x\right)^2}}{t} \tag{1.2}$$

If offset is very small compared to reflector depth, the equation simplifies to:

$$V = \frac{2\,h}{t} \tag{1.3}$$

This method is limited by the spatial distribution of reflecting interfaces with known depth. However, data can often be rapidly collected by use of equipment which keeps the antennas at a fixed offset as they are moved.

Reflected arrivals from a horizontal reflector in a multi-offset gather display an increase in travel time with increasing offset following a hyperbolic trajectory known as the normal move out (NMO) (Yilmaz, 2001). The curvature of the trajectory is related to the apparent velocity of the medium, known as the root mean square (RMS) velocity. Often, the squares of two-way travel time (t), source-receiver offset (x), reflector depth (h), and velocity of the medium (V_{RMS}) are related through the equation:

$$t^2 = \frac{x^2}{V_{RMS}^2} + \frac{4h^2}{V_{RMS}^2} \tag{1.4}$$

Thus, the square of the two-way travel time is linearly proportional to the inverse of V_{RMS} squared. A least-squares best-fit line can be fit to the travel time picks of a reflector in the x^2-t^2 domain with slope and intercept yielding V_{RMS} and reflector depth, respectively. In a multi-layered system, the moveout of deeper arrivals is affected by the interval velocity within each layer. Once the apparent velocity for each reflection is determined using Equation 4, the Dix equation can be used to determine the unique interval velocity of each layer (Dix, 1955). The interval velocities ($V_{n\text{-}int}$) for a series of n horizontal, flat layers can are related to the RMS velocities (V_n) and reflection arrival times (t_n) from reflections originating from the top and bottom of the nth layer by:

$$V_{n-int} = \left(\frac{V_n^2 t_n - V_{n-1}^2 t_{n-1}}{t_n - t_{n-1}}\right)^{1/2} \tag{1.5}$$

The multi-offset method allows for the reflector depth to be determined from the analysis directly, but accurately positioning the antennas is significantly more time and labor intensive than the constant offset method. Assumptions inherent to NMO velocity are that offsets are small relative to the reflector depth, that reflectors are horizontal, and velocities within a layer do not vary (Yilmaz, 2001).

Applying these methods of velocity analysis to the vadose zone during transient conditions presents unique challenges, particularly if flow is heterogenous. Non-uniform propagation of a wetted low velocity layer through the soil would result in a more complicated geometry than is assumed in NMO analysis. A simple method is therefore proposed here to estimate spatial and temporal velocity variations associated with the wetting front migration through time within an otherwise uniform soil layer. This procedure consists of two steps. First, average lateral velocity variations across the tank over the course of the infiltration event are to be estimated using shifts in travel-time for a reflector at a fixed (but potentially unknown) depth. This step of the procedure combines the initial, i.e. prior to infiltration, average velocity (and reflector depth if unknown) obtained with multi-offset NMO analysis with local travel-time differences observed in repeated constant-offset profiles during infiltration. In the second step of the procedure, the Dix equation (Dix, 1955) is to be used to estimate the velocity of the wetted zone at any time and location along the profile.

The initial V_{RMS} values for the dry soil layer (i.e., the sand in the experimental tank) estimated from the CMPs can then be assigned to all the points in the profiled area. The difference between the travel-time to the interface prior to wetting (t_0) and the travel-

time ($t_k(x)$) observed in a profile collected at a later time during the infiltration event (T) can be used to estimate an incremental change in velocity at any location and time during the experiment ($\Delta V(x,T)$):

$$\Delta V(x,T) = 2\left(\frac{1}{t_k(x)} - \frac{1}{t_0}\right)\left(h^2 + \left(\frac{1}{2}d\right)^2\right)^{1/2} \quad (1.6)$$

The velocity $V(x,T)$ at time T is found by adding the change in velocity $\Delta V(x,T)$ to the initial (V_0):

$$V(x,T) = V_0 + \Delta V(x,T) \quad (1.7)$$

This step of the procedure results in a 1D distribution of the RMS velocity for each position in the profiled area. The Dix equation (Dix, 1955; Yilmaz, 2001) is used to estimate the interval (i.e., layer) velocities ($V_{n\text{-}int}$) for a series of n horizontal, flat layers from the RMS velocities (V_n) and reflection arrival times (t_n) from reflections originating from the top and bottom of the nth layer:

$$V_{int}^{n}(x,T) = \left(\frac{V_n^2 t_n - V_{n-1}^2 t_{n-1}}{t_n - t_{n-1}}\right)^{1/2} \quad (1.8)$$

An assumption that the initial velocity conditions in the sand profile are uniform prior to irrigation allows the initial RMS velocity to represent the dry sand velocity ahead of the wetting front. The travel times to the bottom of the dry layer and wetted zone are tracked in replicate COPs, allowing the unknown wetted interval velocity to be determined using Equation 8. Once the interval velocity of the wetted zone is known,

petrophysical relationships can be utilized to estimate the water content (θ) in this region. In this study, the relationship given by Ferre, et. al. which, for a broad range of water contents gives similar results to the Topp equation, is used (Ferre et al., 1996):

$$\theta = 0.1181 \frac{c}{V_{int}^{n}(x,T)} - 0.1841 \tag{1.9}$$

1.3.3 Migration Processing

GPR images of the subsurface from reflection profiles are visualizations of energy recorded at the surface. Due to irregularities in reflecting surfaces, the presence of scattering objects, and other structural features, the energy recorded at the surface does not strictly come from directly underneath the receiver. The result is that GPR images will often have features that obscure features of interest and decrease the resolution of the image, such as diffraction hyperbolas. Migration is a process which relocates recorded energy in time or space to its true position and improves the image resolution by collapsing diffraction hyperbolas and moving dipping reflections to their proper location (Yilmaz, 1987). This is a standard practice in the seismic exploration industry, where complex geological structures with strong velocity contrasts (e.g. salt bodies) often distort images severely, and many of the migration techniques have been applied to GPR data. The conditions required to migrate GPR data are that the wave propagation kinematics are described by principles of geometrical optics and that wave propagation is non-dispersive (Fisher et al., 1992b).

The improper placement of reflections originates when traces are plotted in their relative positions which contain reflected events not originating from directly beneath the source-receiver pair. For example, the permittivity model in Figure 1.2a contains an inclined interface separating low- and high-permittivity layers from 5-8 m depth and two high-permittivity anomalies at 2-3 m depth. Simulated GPR measurements, plotted as a constant-offset profile with amplitudes plotted relative to their lateral position and two-way travel time, show the characteristic diffraction hyperbolas created by objects below the resolving power of the emitted wave. The depth migrated profile in Figure 1.2c shows the collapse of the diffraction hyperbolas to their proper depth and lateral position.

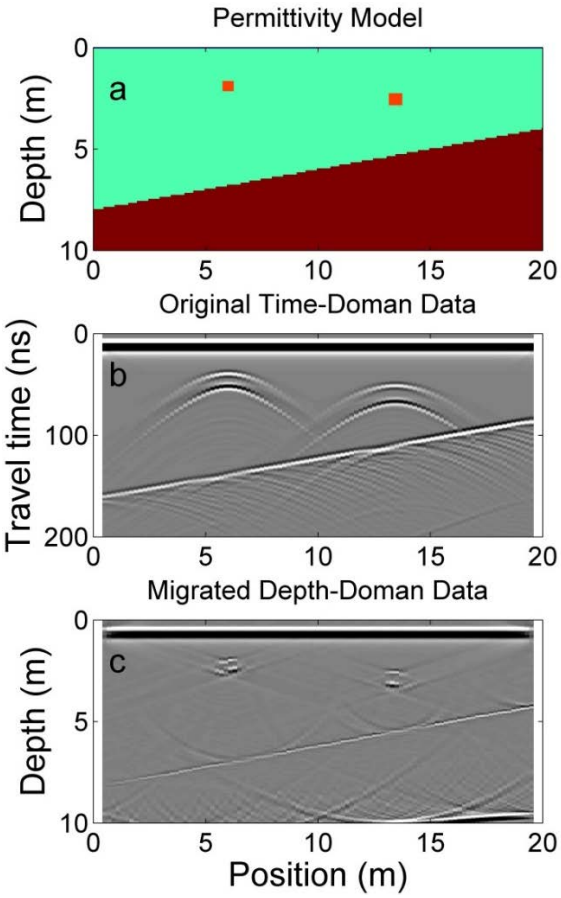

Figure 1.2. Migration example: (a) A permittivity model of the subsurface showing two contrasting layers, the shallower layer having embedded anomalies with contrasting permittivity, (b) the resulting constant offset profile, and (c) a depth migrated profile.

Many migration processing algorithms convert the data from the time-domain to the depth-domain. Time-domain data, as the COP in Figure 1.2b, plot recorded amplitudes relative to their ground position and the travel time of the emitted wave. Depth-domain profiles, such as Figure 1.2c show the recorded amplitudes relative to their true depth. In this work, it is proposed to use the split-step algorithm of Stoffa, et al. (1990) as implemented in Seismic Un*x. This method is an enhancement of frequency-

wavenumber (*f*-k) migration which accounts for lateral velocity variation (Stoffa et al., 1990) and has been demonstrated as an applicable method for GPR (Fisher et al., 1992a).

1.4 Experimental Setup

A wooden tank measuring 4 m x 4 m and filled with 0.60 m of homogenous river sand constructed in the laboratory will be used for performing the forced-infiltration experiments in a simulated vadose zone (Figure 1.3). An impermeable liner separates the sand from a gravel-filled zone. The tank is equipped with a drainage system consisting of 16 – 1 m x 1 m cells which drain independently to the exterior of the tank. Irrigation for the experiments can be applied in a variety of configurations using two 1.5 m-long sprayer arrays consisting of micro-sprayers mounted to PVC pipes. The micro sprayers will be used to collectively spray into a central area measuring approximately 2.25 m^2 at the center of the tank. Soil moisture probes will be buried in the sand at a variety of locations and depths to provide measurements of the system prior to, during, and following irrigation.

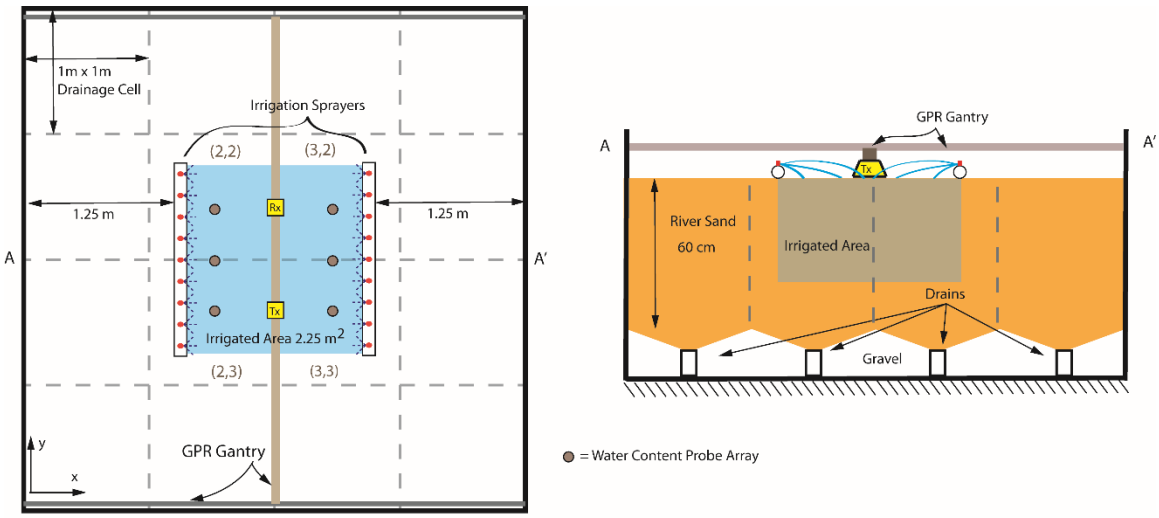

Figure 1.3. A sand tank used as a vadose zone analog for forced-infiltration experiments monitored with time-lapse GPR collected with an automated gantry system.

Time-lapse GPR data will be collected within and beyond the irrigated area using an automated gantry system to automatically position the antennas. This system enables measurements to be made quickly and repeatedly, thus giving the best chance for capturing transient flow phenomena during the experiments. A detailed description of the system can be found in (Mangel et al., 2015). Sensors and Software 1000 MHz shielded antennas will be used to obtain the highest-resolution data possible. The GPR data will be collected continuously during the infiltration as both common midpoint profiles for NMO analysis of velocity as well as constant offset profiles for imaging of spatial changes in arrivals during infiltration and for the proposed single-offset velocity analysis.

1.4.1 Numerical Experiments

Simulations of the forced-infiltration experiments and the TLGPR will be performed for to aid in interpration of GPR profiles and validate results. The flow system will be simulated using an unsaturated (Richard's equation) flow model in HYDRUS 2D (Simunek et al., 1999) coupled to a 2D finite-difference time-domain code implemented in MATLAB (Irving and Knight, 2006) to model the GPR response to the system. The flow model domain will match the dimensions of the sand tank, i.e. 4.0 m x 0.6 m [width x height]. Drains in the tank are to be simulated using seepage face boundary nodes along the bottom of the model in which water leaves the model domain from the node upon reaching saturation (i.e. the pressure head is zero along the seepage face). Constant flux nodes are assigned to the top boundary to represent the irrigated portion of the sand tank.

The water content distributions output from HYDRUS-2D are interpolated to a regular grid to form the GPR model domain. Additions to the model domain allow for interaction of GPR waves with the tank boundaries and consist of a region 0.20 m thick added to the top and sides to simulate air and a region 0.30 m thick added to the bottom to simulate the gravel underlying the sand within the tank. Beyond these regions absorbing perfectly matched layer (PML) boundary conditions are used to remove the effect of reflections from the edge of the simulated domain (Irving and Knight, 2006). Dielectric permittivity values of 1 and 4.5 are to be used in the air and gravel regions, respectively, and held constant. The water content values output from HYDRUS-2D are converted to dielectric permittivity using Ferre's approximation of the Topp equation (Ferre et al., 1996). As this model is focused on wave kinematics and not on preserving exact amplitude information, electrical conductivity and magnetic permeability are assumed constant.

1.5 Works Cited

2009. Ground Penetrating Radar Theory and Applications. Elsevier Science, 1-526 pp.

Allroggen, N., van Schaik, N., Tronicke, J., 2015. 4D ground-penetrating radar during a plot scale dye tracer experiment. Journal of Applied Geophysics, 118: 139-144. DOI:10.1016/j.jappgeo.2015.04.016

Arcone, S.A., Peapples, P.R., Liu, L.B., 2003. Propagation of a ground-penetrating radar (GPR) pulse in a thin-surface waveguide. Geophysics, 68(6): 1922-1933. DOI:10.1190/1.1635046

Becht, A., Appel, E., Dietrich, P., 2006. Analysis of multi-offset GPR data: a case study in a coarse-grained gravel aquifer. Near Surface Geophysics, 4(4): 227-240.

Binley, A., Cassiani, G., Middleton, R., Winship, P., 2002a. Vadose zone flow model parameterisation using cross-borehole radar and resistivity imaging. Journal of Hydrology, 267(3-4): 147-159. DOI:10.1016/s0022-1694(02)00146-4

Binley, A., Winship, P., Middleton, R., Pokar, M., West, J., 2001. High-resolution characterization of vadose zone dynamics using cross-borehole radar. Water Resources Research, 37(11): 2639-2652. DOI:10.1029/2000wr000089

Binley, A., Winship, P., West, L.J., Pokar, M., Middleton, R., 2002b. Seasonal variation of moisture content in unsaturated sandstone inferred from borehole radar and resistivity profiles. Journal of Hydrology, 267(3-4): 160-172. DOI:10.1016/s0022-1694(02)00147-6

Booth, A.D., Clark, R., Murray, T., 2010. Semblance response to a ground-penetrating radar wavelet and resulting errors in velocity analysis. Near Surface Geophysics, 8(3): 235-246. DOI:10.3997/1873-0604.2010008

Bradford, J.H., 2006. Applying reflection tomography in the postmigration domain to multifold ground-penetrating radar data. Geophysics, 71(1): K1-K8. DOI:10.1190/1.2159051

Bradford, J.H., 2008. Measuring water content heterogeneity using multifold GPR with reflection tomography. Vadose Zone Journal, 7(1): 184-193. DOI:10.2136/vzj2006.0160

Bradford, J.H., Harper, J.T., 2005. Wave field migration as a tool for estimating spatially continuous radar velocity and water content in glaciers. Geophysical Research Letters, 32(8): 4. DOI:10.1029/2004gl021770

Brosten, T.R. et al., 2009. Multi-offset GPR methods for hyporheic zone investigations. Near Surface Geophysics, 7(4): 247-257.

Buchner, R., Barthel, J., Stauber, J., 1999. The dielectric relaxation of water between 0°C and 35°C. Chemical Physics Letters, 306(1–2): 57-63. DOI:http://dx.doi.org/10.1016/S0009-2614(99)00455-8

Cassiani, G., Binley, A., 2005. Modeling unsaturated flow in a layered formation under quasi-steady state conditions using geophysical data constraints. Advances in Water Resources, 28(5): 467-477. DOI:10.1016/j.advwatres.2004.12.007

Clothier, B.E., Green, S.R., Deurer, M., 2008. Preferential flow and transport in soil: progress and prognosis. European Journal of Soil Science, 59(1): 2-13. DOI:10.1111/j.1365-2389.2007.00991.x

Cuthbert, M.O., Tindimugaya, C., 2010. The importance of preferential flow in controlling groundwater recharge in tropical Africa and implications for modelling the impact of climate change on groundwater resources. Journal of Water and Climate Change, 1(4): 234-245. DOI:10.2166/wcc.2010.040

Davis, J.L., Annan, A.P., 1989. GROUND-PENETRATING RADAR FOR HIGH-RESOLUTION MAPPING OF SOIL AND ROCK STRATIGRAPHY. Geophysical Prospecting, 37(5): 531-551. DOI:10.1111/j.1365-2478.1989.tb02221.x

de Vries, J.J., Simmers, I., 2002. Groundwater recharge: an overview of processes and challenges. Hydrogeology Journal, 10(1): 5-17. DOI:10.1007/s10040-001-0171-7

Deiana, R., Cassiani, G., Villa, A., Bagliani, A., Bruno, V., 2008. Calibration of a vadose zone model using water injection monitored by GPR and electrical resistance tomography. Vadose Zone Journal, 7(1): 215-226. DOI:10.2136/vzj2006.0137

Dix, C.H., 1955. Seismic velocities from surface measurements. Geophysics, 20: 68-86.

Ferre, P.A., Rudolph, D.L., Kachanoski, R.G., 1996. Spatial averaging of water content by time domain reflectometry: Implications for twin rod probes with and without

dielectric coatings. Water Resources Research, 32(2): 271-279. DOI:10.1029/95wr02576

Fisher, E., McMechan, G.A., Annan, A.P., 1992a. ACQUISITION AND PROCESSING OF WIDE-APERTURE GROUND-PENETRATING RADAR DATA. Geophysics, 57(3): 495-504. DOI:10.1190/1.1443265

Fisher, E., McMechan, G.A., Annan, A.P., Cosway, S.W., 1992b. EXAMPLES OF REVERSE-TIME MIGRATION OF SINGLE-CHANNEL, GROUND-PENETRATING RADAR PROFILES. Geophysics, 57(4): 577-586. DOI:10.1190/1.1443271

Garambois, S., Senechal, P., Perroud, H., 2002. On the use of combined geophysical methods to assess water content and water conductivity of near-surface formations. Journal of Hydrology, 259(1-4): 32-48. DOI:10.1016/s0022-1694(01)00588-1

Geiger, S.L., Durnford, D.S., 2000. Infiltration in homogeneous sands and a mechanistic model of unstable flow. Soil Science Society of America Journal, 64(2): 460-469.

Gomez-Ortiz, D. et al., 2006. Characterization of volcanic materials using ground penetrating radar: A case study at Teide volcano (Canary Islands, Spain). Journal of Applied Geophysics, 59(1): 63-78. DOI:10.1016/j.jappgeo.2005.07.007

Grote, K., Hubbard, S., Harvey, J., Rubin, Y., 2005. Evaluation of infiltration in layered pavements using surface GPR reflection techniques. Journal of Applied Geophysics, 57(2): 129-153. DOI:10.1016/j.jappgeo.2004.10.002

Grote, K., Hubbard, S., Rubin, Y., 2003. Field-scale estimation of volumetric water content using ground-penetrating radar ground wave techniques. Water Resources Research, 39(11): 14. DOI:10.1029/2003wr002045

Grote, K., Hubbard, S.S., Rubin, Y., 2002. GPR monitoring of volumetric water content in soils applied to highway construction and maintenance. The Leading Edge, pp. 482-485.

Guo, L., Chen, J., Lin, H., 2014. Subsurface lateral preferential flow network revealed by time-lapse ground-penetrating radar in a hillslope. Water Resources Research, 50(12): 9127-9147. DOI:10.1002/2013wr014603

Haarder, E.B., Looms, M.C., Jensen, K.H., Nielsen, L., 2011. Visualizing Unsaturated Flow Phenomena Using High-Resolution Reflection Ground Penetrating Radar. Vadose Zone Journal, 10(1): 84-97. DOI:10.2136/vzj2009.0188

Hendrickx, J.M.H., Dekker, L.W., Boersma, O.H., 1993. UNSTABLE WETTING FRONTS IN WATER-REPELLENT FIELD SOILS. Journal of Environmental Quality, 22(1): 109-118.

Hendrickx, J.M.H., Flury, M., Xx, 2001. Uniform and preferential flow mechanisms in the vadose zone. Conceptual Models of Flow and Transport in the Fractured Vadose Zone: 149-187.

Hillel, D., Hatfield, J.L., 2005. Encyclopedia of Soils in the Environment. Elsevier Amsterdam.

Huisman, J.A., Hubbard, S.S., Redman, J.D., Annan, A.P., 2003. Measuring Soil Water Content with Ground Penetrating Radar: A Review. Vadose Zone Journal, 2(4): 476-491.

Irving, J., Knight, R., 2006. Numerical modeling of ground-penetrating radar in 2-D using MATLAB. Computers & Geosciences, 32(9): 1247-1258. DOI:10.1016/j.cageo.2005.11.006

Jacob, R.W., Hermance, J.F., 2004. Assessing the precision of GPR velocity and vertical two-way travel time estimates. Journal of Environmental and Engineering Geophysics, 9(3): 143-153.

Looms, M.C., Jensen, K.H., Binley, A., Nielsen, L., 2008. Monitoring unsaturated flow and transport using cross-borehole geophysical methods. Vadose Zone Journal, 7(1): 227-237. DOI:10.2136/vzj2006.0129

Lunt, I.A., Hubbard, S.S., Rubin, Y., 2005. Soil moisture content estimation using ground-penetrating radar reflection data. Journal of Hydrology, 307(1-4): 254-269. DOI:10.1016/j.hydrol.2004.10.014

Mangel, A.R., Lytle, B.A., Moysey, S.M.J., 2015. Automated high-resolution GPR data collection for monitoring dynamic hydrologic processes in two and three dimensions. The Leading Edge, 34(2): 190-196. DOI:http://dx.doi.org/10.1190/tle34020190.1

Mangel, A.R., Moysey, S.M.J., Ryan, J.C., Tarbutton, J.A., 2012. Multi-offset ground-penetrating radar imaging of a lab-scale infiltration test. Hydrology and Earth System Sciences, 16(11): 4009-4022. DOI:10.5194/hess-16-4009-2012

Mount, G.J., Comas, X., Cunningham, K.J., 2014. Characterization of the porosity distribution in the upper part of the karst Biscayne aquifer using common offset ground penetrating radar, Everglades National Park, Florida. Journal of Hydrology, 515: 223-236. DOI:10.1016/j.jhydrol.2014.04.048

Moysey, S.M.J., 2010. Hydrologic trajectories in transient ground-penetrating-radar reflection data. Geophysics, 75(4): WA211-WA219. DOI:10.1190/1.3463416

Neal, A., Roberts, C.L., 2001. Internal structure of a trough blowout, determined from migrated ground-penetrating radar profiles. Sedimentology, 48(4): 791-810. DOI:10.1046/j.1365-3091.2001.00382.x

Perkins, K.S., Nimmo, J.R., Rose, C.E., Coupe, R.H., 2011. Field tracer investigation of unsaturated zone flow paths and mechanisms in agricultural soils of northwestern Mississippi, USA. Journal of Hydrology, 396(1-2): 1-11. DOI:10.1016/j.jhydrol.2010.09.009

Richards, L.A., 1931. CAPILLARY CONDUCTION OF LIQUIDS THROUGH POROUS MEDIUMS. Journal of Applied Physics, 1(5): 318-333. DOI:doi:http://dx.doi.org/10.1063/1.1745010

Selker, J., Steenhuis, T., Parlange, J.-Y., 1992. Wetting front instability in homogeneous sandy soils under continuous infiltration. Soil Science Society of America Journal, 56(5): 1346-1350.

Simunek, J., Sejna, M., van Genuchten, M.T., 1999 The Hydrus-2D software package for simulating two-dimensional movement of water, heat, and multiple solutes in variably saturated media. Version 2.0. International Ground Water Modeling Center, Colorado School of Mines, Golden, Colorado, pp. 251.

Steelman, C.M., Endres, A.L., 2012. Assessing vertical soil moisture dynamics using multi-frequency GPR common-midpoint soundings. Journal of Hydrology, 436: 51-66. DOI:10.1016/j.jhydrol.2012.02.041

Steelman, C.M., Endres, A.L., Jones, J.P., 2012. High-resolution ground-penetrating radar monitoring of soil moisture dynamics: Field results, interpretation, and comparison with unsaturated flow model. Water Resources Research, 48: 17. DOI:10.1029/2011wr011414

Stoffa, P.L., Fokkema, J.T., Freire, R.M.D., Kessinger, W.P., 1990. SPLIT-STEP FOURIER MIGRATION. Geophysics, 55(4): 410-421. DOI:10.1190/1.1442850

Stoffregen, H., Yaramanci, U., Zenker, T., Wessolek, G., 2002. Accuracy of soil water content measurements using ground penetrating radar: Comparison of ground penetrating radar and lysimeter data. Journal of Hydrology, 267: 201-206.

Sukhija, B.S., Reddy, D.V., Nagabhushanam, P., Hussain, S., 2000. Natural groundwater recharge assessment: Role of preferential flow in semi-arid fractured aquifers. Groundwater: Past Achievements and Future Challenges: 331-336.

Sukhija, B.S., Reddy, D.V., Nagabhushanam, P., Hussain, S., 2003. Recharge processes: piston flow vs preferential flow in semi-arid aquifers of India. Hydrogeology Journal, 11(3): 387-395. DOI:10.1007/s10040-002-0243-3

Topp, G.C., Davis, J.L., Annan, A.P., 1980. Electromagnetic Determination of Soil-Water Content - Measurements in Coaxial Transmission Lines. Water Resources Research, 16(3): 574-582. DOI:10.1029/WR016i003p00574

Truss, S., Grasmueck, M., Vega, S., Viggiano, D.A., 2007. Imaging rainfall drainage within the Miami oolitic limestone using high-resolution time-lapse ground-penetrating radar. Water Resources Research, 43(3): 15. DOI:10.1029/2005wr004395

Turesson, A., 2006. Water content and porosity estimated from ground-penetrating radar and resistivity. Journal of Applied Geophysics, 58(2): 99-111. DOI:10.1016/j.jappgeo.2005.04.004

Vellidis, G., Smith, M.C., Thomas, D.L., Asmussen, L.E., 1990. Detecting wetting front movement in a sandy soil with ground-penetrating radar. Transactions of the Asae, 33(6): 1867-1874.

Vereecken, H. et al., 2008. On the value of soil moisture measurements in vadose zone hydrology: A review. Water Resources Research, 44: 21. DOI:10.1029/2008wr006829

Yao, T.-m., Hendrickx, J.M., 1996. Stability of wetting fronts in dry homogeneous soils under low infiltration rates. Soil Science Society of America Journal, 60(1): 20-28.

Yilmaz, O., 1987. Seismic Data Analysis: Processing, Inversion, and Interpretation of Seismic Data. Society of Exploration Geophysicists, Tulsa, OK.

Yilmaz, O., 2001. Seismic Data Analysis: Processing, Inversion, and Interpretation of Seismic Data. Society of Exploration Geophysicists, Tulsa, OK, 2065 pp.

CHAPTER 2

TIME-LAPSE MONITORING OF NON-UNIFORM FLOW IN A HOMOGENOUS MEDIUM USING GROUND PENETRATING RADAR

2.1 Abstract

Use of time-lapse ground penetrating radar (GPR) is a promising method for studying non-uniform and preferential flow of water through the vadose zone. This chapter presents the results of two forced infiltration experiments in a homogenous sand-filled tank monitored with GPR and water content probes embedded in the sand. The patterns of wetting front propagation evident in the water content probes generally reflects the distribution of applied fluxes to the sand surface, though there is evidence of rapid transport of water and bypass flow through significant portions of the sand in one corner of the experimental area indicating flow is non-uniform through the homogenous sand. Time-lapse GPR profiles were collected along 12 lines within and beyond the irrigated area. Transient arrivals in the GPR images related to the propagation of the wetting front through the sand show considerable spatial non-uniformity in their increased travel time that is consistent with the applied fluxes and water content probe data. The GPR profiles are interpreted to contain evidence of a complex wetted zone geometry through the sand tank and, in particular, evidence of non-uniform flow features such as channeling and fingering is presented.

2.2 Introduction

The sensitivity of ground penetrating radar (GPR) to variations in water content as well as its potential for rapid sampling of the subsurface have led to investigations into its utility for monitoring dynamic hydrologic processes, such as individual infiltration events (Binley et al., 2001; Haarder et al., 2011; Truss et al., 2007; Vellidis et al., 1990) or seasonal variability in hydrologic state (Binley et al., 2002; Steelman and Endres, 2012; Steelman et al., 2012). The potential for monitoring preferential flow *in situ* with GPR has been recognized for some time. Vellidis et al. (1990) describe a forced infiltration experiment into sands of the Georgia Coastal Plain and tracked the wetting front with GPR for 25 hours and note the possibility of identifying preferential flow paths, but did not observe any occurrence in their data. Truss, et al. (2007) performed an infiltration experiment into the Miami limestone and observed a number of diffraction features in the GPR data. The authors attributed diffractions to preferential flow through the root zone, rubble, and dissolution fingers in the unsaturated rock. A dye-tracer experiment was performed by Haarder, et al. (2011) in sandy deposits in which fingered flow was observed in the dye-stain patterns in excavated trenches following infiltration. The predicted GPR response from fingered flow was simulated, but these features were not observed in the data collected during infiltration. Allroggen, et al. (Allroggen et al., 2015) performed a similar dye-staining experiment and observe flow fingers in the excavated soil cross-sections but do not detect fingered flow with GPR. Increases in the travel time to specific reflecting interfaces were interpreted to be caused by the preferential movement of water and verified in the observed dye-staining. These studies demonstrate

the mixed success of detecting preferential flow using GPR. Analysis of patterns in the GPR data suggesting preferential flow were verified in excavations, yet the limitations in temporal sampling and image resolution indicate that individual fingers related to non-uniform or preferential flow may not be resolved.

Recent developments in automated positioning of antennas improve the capability of GPR for monitoring complex flow systems. Rapid time-lapse monitoring of single infiltration events has been utilized for estimation of soil hydraulic parameters (Moysey, 2010). By coupling GPR with automated positioning systems it has been possible to quantify rapid changes in bulk water content within a soil profile in 1-D (Mangel et al., 2012) and observe spatial variations in wetting and fluid flow in 2-D and 3-D (Glaser et al., 2012; Mangel et al., 2015; Versteeg and Birken, 2001).

This paper continues the approach of these studies by presenting the results from two irrigation experiments conducted within homogenous sand that was monitored with time-lapse GPR as well as soil moisture sensors. Changes in the arrivals within the GPR profiles from the first experiment suggest instances of non-uniform flow through an ostensibly homogenous medium.

2.2 Methods

The experiments were conducted in a wooden tank measuring 4 m x 4 m and filled with 0.60 m of homogenous river sand (Figure 2.1a,b). The tank is equipped with a drainage system consisting of 16 – 1 m x 1 m cells which drain independently to the exterior of the tank, and an impermeable liner separates the sand from a gravel-filled

zone used to support the drains. Irrigation for the experiments was applied using two 1.5 m-long sprayer arrays consisting of micro-sprayers mounted to PVC pipes.

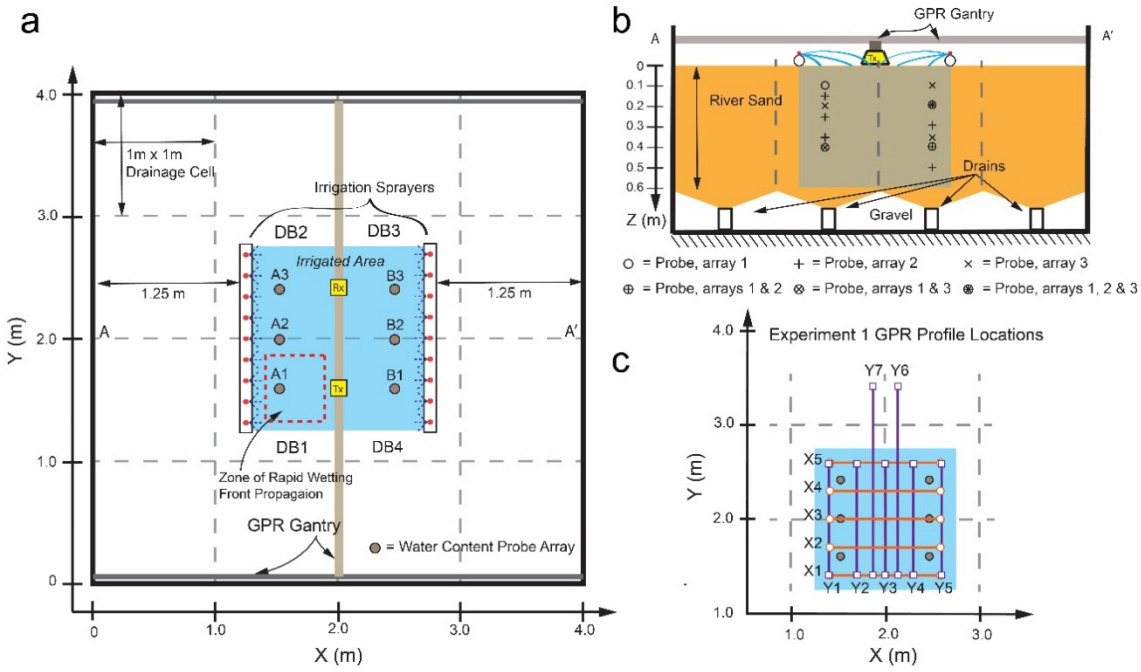

Figure 2.1. Experiment 1 setup. a) Plan view of the tank showing positions of the irrigation sprayers, drainage bays (DB1-DB4), automated GPR gantry, and six vertical arrays of water content probes at various depths in the sand (A1-B3). The zone of rapid wetting front propagation described in the text is labeled. b) Cross-section through the tank center illustrating the probe locations. c) Detail of the irrigated area and positions of GPR profiles collected in Experiment 1 (X1-X5 and Y1-Y7).

The micro sprayers collectively irrigate a central area measuring approximately 2.25 m^2. The volumetric flux applied to the sand surface was controlled at 8 liters/min, or an effective flux of 3.56 mm/min across the irrigated area. The volumetric water content of the sand was monitored using Decagon EC-5 water content probes placed horizontally in the sand as vertical arrays in six locations with various depths shown in Figure 2.1a, Figure 2.1b and summarized in Table 2.1. The array positions within the irrigated area

were selected to minimize interference of reflections from water content probes in the GPR profiles. Water content measurements at each probe were recorded at 10-second intervals in both experiments. The irrigation pattern of the sprayers is not strictly uniform, thus the spatial pattern of the flux application was characterized by spraying into an array of plastic cups for five minutes. The mass of water in each cup was used to estimate the volume of water applied, and dividing the volume of water by the effective area of each cup results in the irrigation flux.

Table 2.1. Locations of water content probe arrays and probe depths within the experimental tank.

Array	X-Y Position (m)	Probe Depths (m)	Array	X-Y Position (m)	Probe Depths (m)
A1	[1.50, 1.60]	0.10, 0.40	B1	[2.50, 1.60]	0.20, 0.40
A2	[1.50, 2.00]	0.15, 0.25, 0.35	B2	[2.50, 2.00]	0.20, 0.30, 0.40, 0.50
A3	[1.50, 2.40]	0.20, 0.40	B3	[2.50, 2.40]	0.10, 0.20, 0.35

Time-lapse GPR data were collected within and beyond the irrigated area using an automated gantry system to automatically position the antennas. A detailed description of the system can be found in (Mangel et al., 2015). These experiments were performed with an updated version of the gantry system utilizing a fiberglass central rail, rather than aluminum, to minimize interference. Sensors and Software 1000 MHz shielded antennas were used to obtain the highest-resolution data possible. A time sampling window of 25 ns was used along with 4 stacks per trace. Prior to irrigation, the sand surface was raked flat to ensure good coupling of the radar antennas with the ground. Post-processing included a static time-zero correction to all traces.

Table 2.2. Positions of COPs collected during Experiment 1.

Initial X-Y position (m)	Final X-Y Position (m)	Name	Initial X-Y position (m)	Final X-Y Position (m)	Name
[1.40, 1.40]	[2.60, 1.40]	X1	[1.70, 1.40]	[1.70, 2.60]	Y2
[1.40, 1.70]	[2.60, 1.70]	X2	[2.00, 1.40]	[2.00, 2.60]	Y3
[1.40, 2.00]	[2.60, 2.00]	X3	[2.30, 1.40]	[2.30, 2.60]	Y4
[1.40, 2.30]	[2.60, 2.30]	X4	[2.60, 1.40]	[2.60, 2.60]	Y5
[1.40, 2.60]	[2.60, 2.60]	X5	[2.20, 1.40]	[2.20, 3.50]	Y6
[1.40, 1.40]	[1.40, 2.60]	Y1	[1.80, 1.40]	[1.80, 3.50]	Y7

Experiment 1 was monitored with time-lapse GPR as a sequence of constant offset profiles (COPs) in the X and Y directions listed in Table 2.2. Two profiles (Y6 & Y7) collected data beyond the irrigated area. Source-receiver offset was 0.16 m for all profiles. Irrigation began concurrent with the start of data collection and terminated after 26 minutes. The 12-profile cycle was repeated fifteen times over approximately 26 minutes, with 1.75 minutes between repeated traces and a total of 156,815 traces collected.

2.3 Results

2.3.1 Irrigation Flux Characterization

The results of the spatial flux characterization are illustrated in Figure 2.2. The mean flux was 2.20 mm/min with standard deviation of 1.76 mm/min, i.e. substantially less than the target applied flux of 3.56 mm/min. Fluxes are generally higher (1.0 – 7.0 mm/min) in a zone from 1.30 m – 1.85 m Y position, with several hot spots receiving up to 13.4 mm/min flux (600% of mean). Fluxes are lower in the center of the irrigated area,

receiving 0.05 – 0.20 mm/min. The flux applied to the moisture probe locations varied and was highest in the area surrounding the A1 probe array.

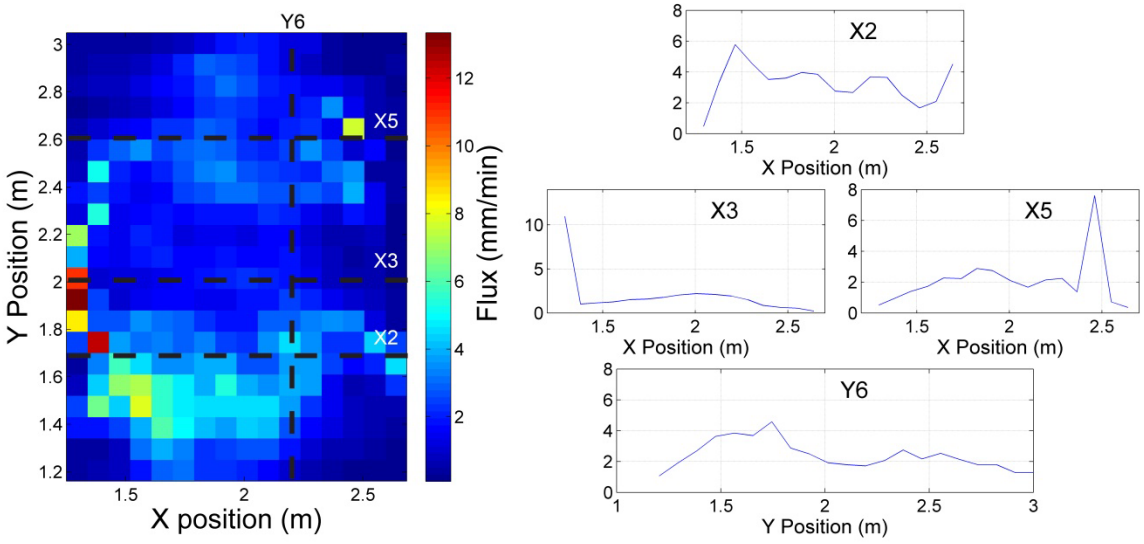

Figure 2.2. Irrigation flux distribution, in mm/min, within the irrigated area. Positions are relative to the tank. Irrigation flux profiles for specific GPR lines discussed in the text are shown.

2.3.2 Water Content Probe Measurements

Patterns of wetting in water content probe data are generally similar between the two irrigation experiments, though significant differences are present. Probe data are grouped by position and shown in Figure 2.3 for Experiment 1 and Figure 2.4 for Experiment 2. Initial water content values in both experiments do not display a clear trend with depth or position and varied from 0.026 vol/vol to 0.069 vol/vol in Experiment 1 and from 0.034 to 0.083 vol/vol in Experiment 2. Water content behind the wetting front was also variable from probe to probe, but generally similar between experiments. The Experiment 1 mean was 0.192 vol/vol and ranged from 0.11 to 0.27 vol/vol, and Experiment 2 had a

mean of 0.188 vol/vol and varied from 0.13 to 0.27 vol/vol The sand did not approach the saturation value of 0.35 at any location or depth. In both experiments the wetting front generally advanced more rapidly in the A1-A3 probe arrays than in the B1-B3 probe arrays, and was fastest in the A1 array. Water content behind the wetting front is often higher in arrays A1-A3 as well (e.g. Figure 2.3b,e; Figure 2.4b,e), which is consistent with the generally higher fluxes in this region. Two probes display rapid fluctuations in water content (probe B3 in Figure 2.3d, probe B1 in Figure 2.4f) indicative of instrument errors.

The wetting front arrival trends in Experiment 1 consistently show shallower probes experiencing the wetting front sooner than deeper probes in each array (Figure 2.3), though the wetting front advances at a greater observed rate in the A1, A2, and B3 probe arrays.

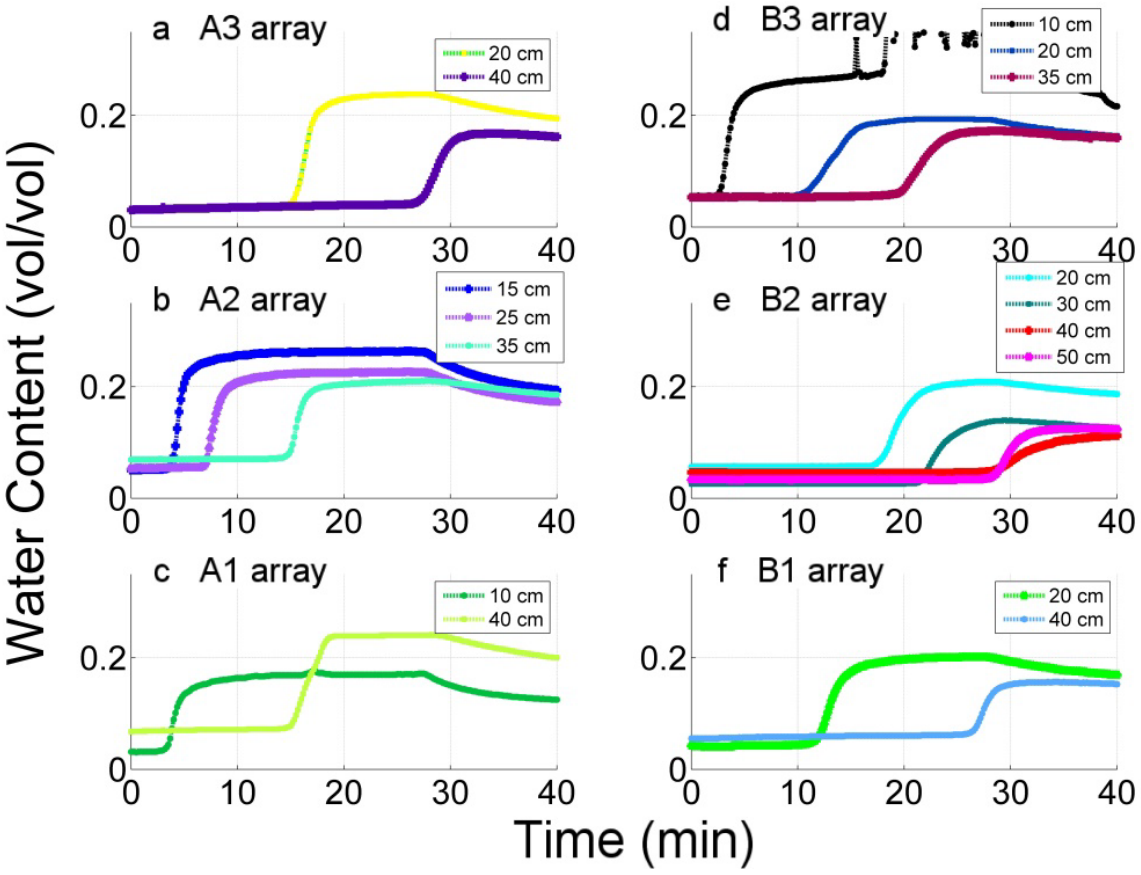

Figure 2.3. Experiment 1 water content probe measurements grouped by location.

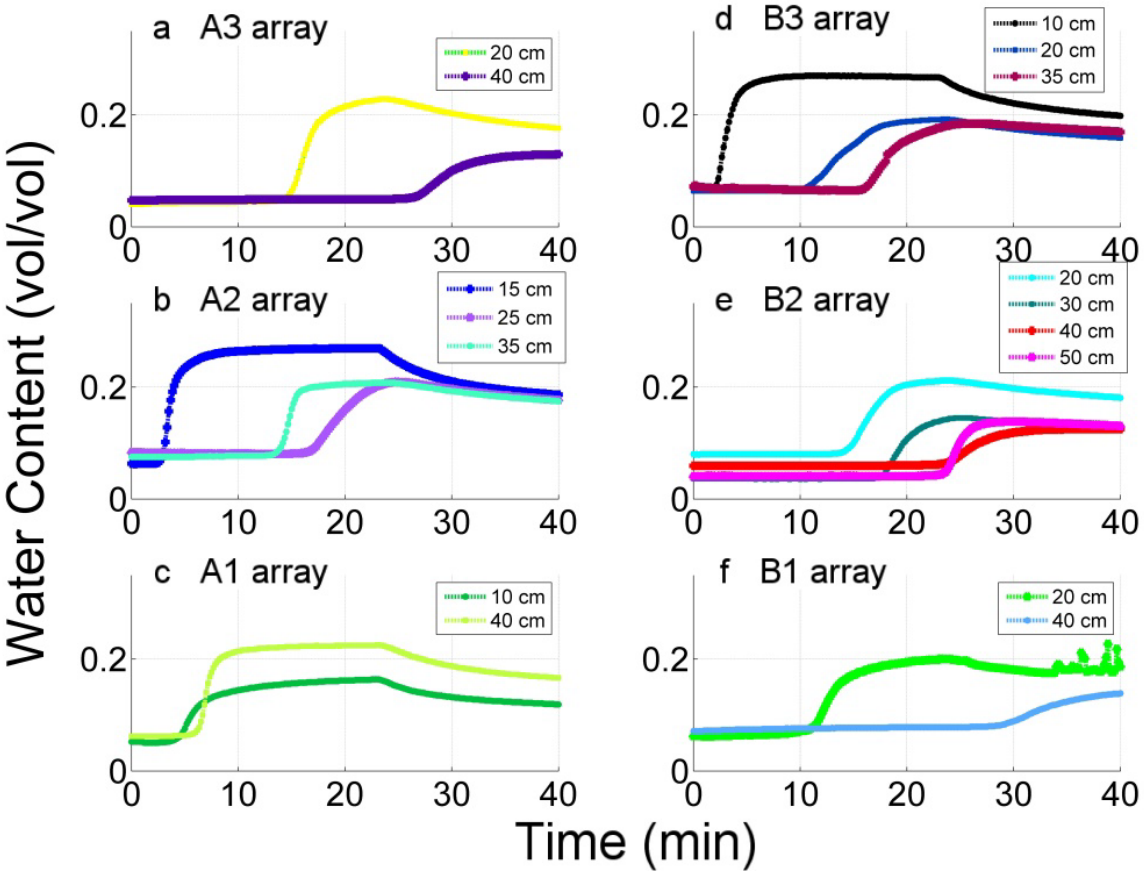

Figure 2.4. Experiment 2 water content probe measurements grouped by location.

The wetting front reached the shallow probes (0.10 – 0.15 m) after 2.6 to 3.0 minutes, 0.20 m depth after 9.8 to 17.2 minutes, and 0.25 – 0.35 m between 7.2 and 21.5 minutes. The A1(0.4m) probe measured the wetting front significantly ahead of the other deep probes at 14.8 minutes, with the others sensing the wetting front from 26.3 to 28.0 minutes.

The water content probe measurements from Experiment 2 indicate a more complicated flow system than Experiment 1. The wetting front passed the shallow probes (≤ 0.15 m depth) from 2.3 to 4.8 minutes, 0.20 m depth after 9.5 to 14.2 minutes, 0.25 –

0.35 m depth between 13.3 and 17.5 minutes, and 0.40 – 0.50 m depth between 5.3 and 28 minutes. The wetting front reached the A1(0.1m) probe at 4.3 minutes and the A1(0.4m) probe shortly after at 5.3 minutes. The rapid flow to 0.40 m depth observed in the A1 array during Experiment 2 was much faster than Experiment 1. Preferential flow was evident in array A2 as the wetting front bypassed the 0.25 m probe, arriving at 16 minutes, while the shallower 0.25 m probe measured the wetting front at 13 minutes. Wetting was slower in array A3 than A1 and A2 and was more consistent with arrays B1-B3. Contrasting Experiment 1 is probe B1(0.4m) in Figure 2.4f,which displayed a gradual increase in water content from 28 to 40 minutes (c.f. Figure 2.3f).

Table 2.3. Wetting front velocities from surface to water content probe.

Experiment 1				Experiment 2			
Probe	Wetting velocity (mm/min)	Probe	Wetting velocity (mm/min)	Probe	Wetting velocity (mm/min)	Probe	Wetting velocity (mm/min)
A1(0.10m)	28.6	B1(0.40m)	14.7	A1(0.10m)	20.8	B1(0.40m)	13.9
A1(0.40m)	26.1	B2(0.20m)	10.9	A1(0.40m)	60.0	B2(0.20m)	13.2
A2(0.15m)	37.5	B2(0.30m)	13.9	A2(0.15m)	47.5	B2(0.30m)	16.8
A2(0.25m)	34.9	B2(0.40m)	13.1	A2(0.25m)	14.6	B2(0.40m)	16.3
A2(0.35m)	23.1	B2(0.50m)	17.1	A2(0.35m)	25.4	B2(0.50m)	20.8
A3(0.20m)	12.9	B3(0.10m)	40.0	A3(0.20m)	12.9	B3(0.10m)	42.9
A3(0.40m)	15.6	B3(0.20m)	19.1	A3(0.40m)	15.6	B3(0.20m)	16.2
B1(0.20m)	16.2	B3(0.35m)	18.0	B1(0.20m)	18.5	B3(0.35m)	21.7
Experiment 1 Mean		21.4 mm/min		Experiment 2 Mean		23.6 mm/min	

Estimates of the wetting front velocity in each array location were determined from the elapsed time from the sand surface to each probe and are contained in Table 2.3. The mean velocity for both experiments was 22.5 mm/min, and velocities were consistently higher in the A arrays than B arrays in both experiments, though velocities were overall greater in Experiment 2 than Experiment 1. The A1 probe array recorded the highest

propagation velocity of 60 mm/min during Experiment 2. The trends in the Table 2.3 velocities are consistent with the flux patterns in Figure 2.2. Flux is highest above the A1 probes and propagation velocities are highest in this location during Experiment 2. Fluxes above the other probe arrays are more uniform, though the influence of a "hot-spot" at [2.45 m, 2.64 m] receiving 7.6 mm/min may account for the greater wetting front velocity observed in the B3 probes of 18.0 – 42.9 mm/min.

Table 2.4. Elapsed time between start of irrigation and observed drainage from the tank.

Experiment 1		Experiment 2	
Drainage Bay	Drainage Observed (min)	Drainage Bay	Drainage Observed (min)
DB1	25 min	DB1	21 min
DB2	38 min	DB2	31 min
DB3	52 min	DB3	40 min
DB4	40 min	DB4	35 min

Observed drainage sequences from the tank, contained in Table 2.4, describe trends of infiltration averaged over a larger volume than the water content probes and are less exact in time. However, they illustrate propagation of percolated water most rapidly in DB1 and DB2 consistent with the greater wetting velocities in the A1-A3 probe arrays. Drainage from DB1 was first in both experiments: at 25 min and 21 min for Experiments 1 and 2, respectively. Drainage was last observed at approximately twice these times from DB3, at 52 min in Experiment 1 and 40 min in Experiment 2. Drainage from DB4 closely followed DB2, with 2 minutes elapsed time in Experiment 1 and 4 minutes during Experiment 2.

The water content probe data, observed drainage sequence, and wetting front propagation velocities describe a flow regime in which wetting of the sand and

propagation of a wetting front is spatially non-uniform and strongly determined by the applied flux. The zone around water content probe array A1 and drainage bay DB1 (shown in Figure 2.1a) reliably demonstrates the fastest transport of water through the sand, and wetting fronts in water content probes are generally sharp and suggest flow of water was downward with little lateral flow. However, the Experiment 2 probes demonstrate that flow bypassed portions of the sand, though the mechanism by which this occurred cannot be inferred directly from the data. The GPR data from Experiment 1 offer insight into these occurrences of non-uniform flow.

2.3.3 Ground Penetrating Radar Profiles

A consistent feature of the GPR profiles is a sub-horizontal reflection from the base-of-sand/gravel interface located at 0.60 m depth. Numerous sub-horizontal reflecting interfaces of short extent (0.05 – 0.25 m) are present within the sand but diffractions from discrete objects are not detected prior to irrigation. Transient arrivals in the time-lapse images suggest faster wetting front propagation through the sand in the (southwest) corner of the tank shown in Figure 2.1a, which is located around probe array A1 and drainage cell B1 (i.e., x-position between 1.40 m – 1.80 m and y-position from 1.40 – 1.90 m). This observation is consistent with the water content probe data and observations of drainage from the tank.

Early in the experiment, reflections from the wetting front generally appear continuously across the profiles and exhibit greater increases in travel time at locations receiving higher flux. Arrivals in the GPR data which suggest the presence of non-uniform flow features and lateral redistribution of water along reflecting interfaces within

the sand are abundant within the data, though only a few sets of time-lapse profiles are presented for brevity. Arrivals referenced in the text are labeled sequentially by order of presentation, and if transient arrivals cannot be directly tracked between sequential time-lapse profiles a new label is assigned.

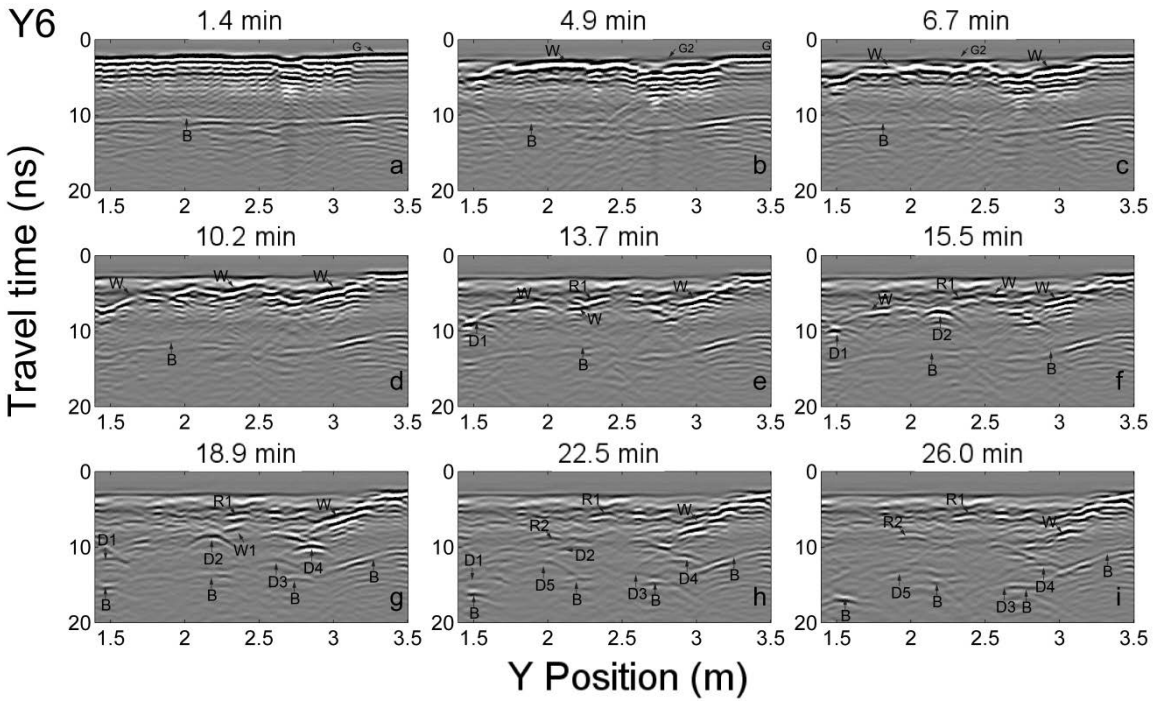

Figure 2.5. Profile set Y6, collected along X = 2.20 m, demonstrates numerous diffraction hyperbolas from discrete portions of the wetted zone.

Evidence for non-uniform propagation of a distinct wetting front is most easily observed in the profiles collected parallel to the irrigation sprayer arrays. Profile Y6 was collected along X = 2.20 m and representative images are shown in Figure 2.5. Initially, the base of sand reflection (labeled B) is present across the profiled area at 10 ns. In the first profile collected at 1.4 minutes (panel a) it is possible to identify the direct ground wave arrival at 1.2 ns (G). Arrival G is followed by high amplitude arrivals at 2-5 ns from

1.4 m to 3.1 m and a number of diffraction tails originating within this zone, likely due to water infiltrating unevenly into the sand. At 4.9 min (panel b) it is possible to identify a distinct and sub-horizontal reflection (W) between 1.4 m and 3.2 m. As the only change in the system state is from irrigation, arrival W is interpreted as a reflection from the wetting front as it propagates downward through the sand. From 1.4 m to 1.6 m and 2.6 m to 3.0 m position, the wetting front arrival is about 1 ns later than the other positions, where depressed direct ground wave is now visible with a later arrival time (lebeled G2). The travel time of the groundwave has almost doubled (from 1.2 to 2 ns) in this zone of active flow, which is indicative of greater wetting in these areas. By 6.7 minutes (Figure 2.5c) the late arrival of the ground wave is visible across the entire irrigated area at 2 ns. Arrival B has an undulating character and the most depressed travel time (11.5 ns) from 1.4 m to 1.5 m and 2.4 m to 2.8 m, corresponding to where W arrives latest at 4.6 ns. Arrival W can be traced across the profile at 10.2 minutes and the spatial pattern of its arrival time is consistent with the applied flux curve in Figure 2.2, i.e. the largest increases in arrival time are evident where applied fluxes are greatest. From 1.4 m to 1.5 m, W arrives latest at 6.4 ns, from 1.7 m to 2.3 m arrives between 4.5 and 4.9 ns. The edge of the wetted zone decreases in travel time from 2.7 m to 3.3 m, above which arrivals are unchanged. B retains an undulating character which replicates the shape of W above.

The wetting front arrival begins to separate into discontinuous sets of arrivals at 13.7 minutes into Experiment 1. A distinct diffraction hyperbola (D1) is visible with an apex at 1.52 m position, 8 ns. Discrete W arrivals are present, for instance 1.60 m to 2.0 m, 6.5

ns; 2.80 m, 8.2 ns; 2.9 m to 3.1 m, 6.2 to 4.5 ns (Figure 2.5e). After 15.5 minutes (Figure 2.5f), D1 has increased travel time to 9.1 ns. W is visible as high amplitude arrivals from 1.7 m to 1.85 m and 2.6 to 3.2 m, 7 ns travel time. W arrives around 4.7 – 5.5 ns from 2.25 m to 2.65 m, and now a second hyperbola (D2) is apparent at 2.2 m, 6.7 ns. D2 appears to have separated from W between 13.7 and 15.5 minutes (panels e-f). W has been delayed relative to D2, and there is a lateral increase in the high amplitude arrival along a reflector (R1) at 5.2 ns travel time, from 2.2 m - 2.4 m at 13.7 minutes to 2.2 m - 2.62 m at 15.5 minutes. At 18.9 minutes (Figure 2.5g) the high amplitude arrivals have not increased travel time, though a new distinct arrival (W1) appears below R1 at 2.26 m to 2.40 m, 6.5-7 ns and earlier than D2, whose apex now arrives at 7.7 ns. New diffractions are visible with apices at 2.61 m, 11.2 ns (D3) and 2.85 m, 9.1 ns (D4). The evolution of the continuous W arrival into D4 can be traced along subsequent profiles, yet the D3 arrival emerges in the profile without a predecessor.

W remains continuous only as a tilted arrival at 22.5 minutes, from 2.85 m to 3.20 m, 7.6 to 3.9 ns. D1 has lost coherence and appears as a faint arrival at 13.7 ns, 1.4 m to 1.7 m position and above B at 15.4 ns, 1.45 m to 1.55 m position (Figure 2.5h). Similarly, D2 arrives at 2.1 m, 10 ns and is no longer a clear hyperbola. A static reflector (R2) remains at D2's former position and remains for the experiment duration. A new hyperbola (D5) has emerged at 2.0 m, 11.2 ns without a predecessor. The hyperbolic shape of D3 has been distorted, and the arrival is located at 2.6 m, 13 ns, just above B at 2.7 m, 13.9 ns. D4 is similarly distorted and arrives at 2.85 m, 10.7 ns. In the final profile at 26.0 minutes (Figure 2.5i), arrival W at 2.95 – 3.15 m, 7.7 - 6 ns has separated from a

stationary reflector above it, and it is now evident that this is R1 which, upon wetting, appears as a sub-horizontal, moderately continuous reflector from 1.8 m to 3.1 m. D3 arrives concurrently with B at 14.5 ns, 2.6 m, and D4 remains visible at 2.85 m, 11.9 ns adjacent to an inclined B arrival. D1 cannot be distinguished, though B at that position increases in amplitude, suggesting that water may be ponding slightly along the base of sand interface. Drainage from bay DB1 was first observed at 25 min and verifies that water had been transported entirely through the sand at this location.

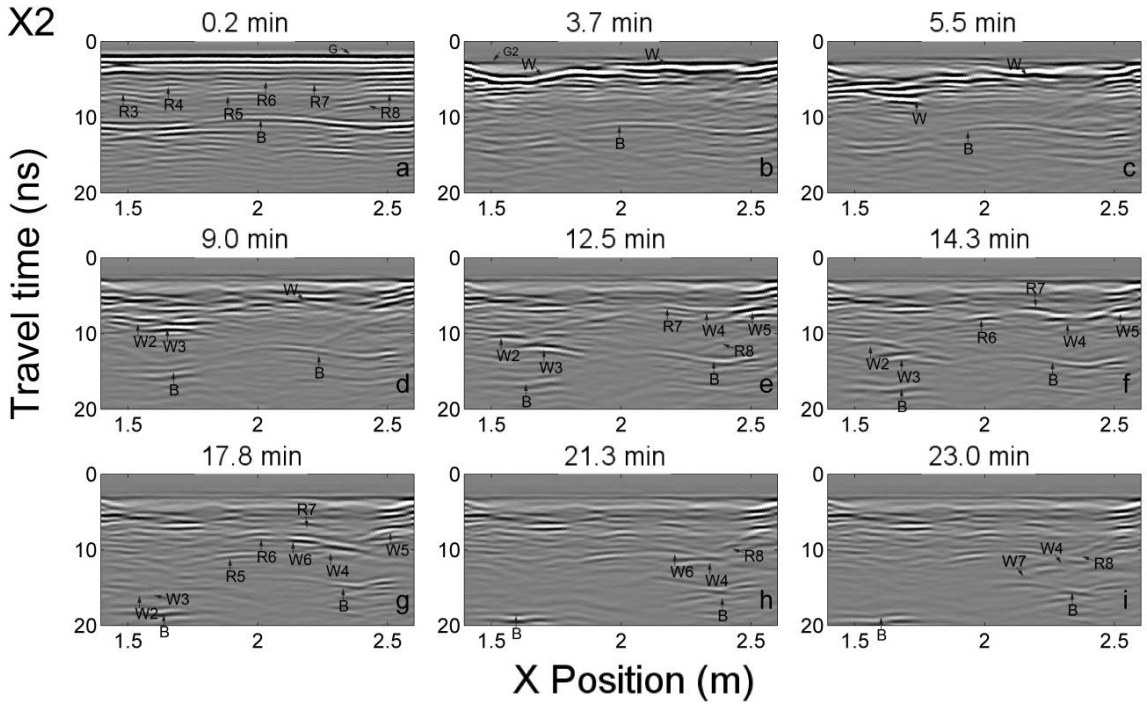

Figure 2.6. X2 profile set collected along Y = 1.70 m. Static reflectors within the sand influence wetting front propagation.

Many interactions between the propagating wetting front and sub-horizontal to inclined, discrete reflectors in the sand are visible in the profiles, such as the X2 profile set, shown in Figure 2.6, which was collected along Y = 1.70 m. Discrete reflecting

interfaces are present at 1.4 m – 1.6 m, 8 ns (labeled R3), 1.6 m – 1.7 m position, 6 ns travel time (R4), 1.8 m to 2.05 m position, 7 ns (R5), 2.0 m to 2.1 m and 5.5 ns (R6), 2.2 to 2.3 m, 6 ns (R7), and 2.4 m – 2.6 m position, 5-8 ns with an inclined bottom reflector extending out to 2.25 m position (R8). Initially, the wetting front (W) advances at a steady rate. Between 3.7 and 5.5 minutes, the front stalls from 1.5 – 1.65 m position as it approaches R4, but high amplitude arrivals continue to propagate laterally about this point. At 9.0 minutes, distinct arrival sets are visible at 1.5 m – 1.62 m, 8 ns (labeled W2) and from 1.55 m – 1.75 m, 9.5 ns (W3), and W3 continues to advance ahead of the earlier W2 arrival. From 12.5 to 14.3 minutes, the wetting front from 2.0 to 2.4 m has reached R7 and a discrete arrival (W4) continues to propagate, but the front stalls from 2.4 m to 2.6 m (W5). At 17.8 minutes, W2 and W3 arrive concurrently at 15 ns just above B at 17 ns. The wetting front has stalled around 2.0 m and 2.4 – 2.6 m (W5), though amplitudes increase in this location. The wetting front has passed R7 and a distinct arrival (W6) emerges adjacent to W4. W2 and W3 arrive concurrently with B at 21.3 minutes, and this set of arrivals does not increase in travel time in the final profile at 23.0 minutes. As W4 and W6 advance downward through the sand, a significant reduction in amplitude occurs after 17.8 minutes, and at 21.3 minutes W4 and W6 have intersected R8 at 2.3 m, 11 ns travel time. R8 is visible at 23.0 minutes, and a faint arrival (W7) has emerged at 2.15 m to 2.25 m, 13 ns. The amplitude reduction of W4 and W6 as they intersect R8 and the emergence of W7 at a lower position and later travel time suggest the lateral movement of water out of the profiled plane and along the R8 interface.

The Y6 and X2 profile sets establish the non-uniform propagation of transient arrivals through the sand, contain diffraction arrivals from discrete subwavelength-scale objects not present prior to irrigation, and illustrate interactions between the wetting front and static, discrete reflectors. The origins of discontinuous arrivals in time (e.g. D3 and D5 in Y6) can be examined along other perpendicular profiles. Figure 2.7 shows the the X3 profiles collected along Y = 2.0 m in which the origin of D5 can be observed due to lateral shifting of flow along a reflector (R9) at 2.0 to 2.2 m, 7 ns travel time (Figure 2.7a). W propagates in a fairly uniform manner until 5.7 mins, after which travel time increases more rapidly from 1.4 m to 1.8 m (not shown). W is continuous across the profile until 12.7 minutes, after which discrete high amplitude arrivals are present. At 17.9 minutes (Figure 2.7c), the wetting front reflection from 1.9 m – 2.0 m, 9.5 ns (W8) and at 2.08 m – 2.15 m, 7.5 ns (W9) are adjacent to R9. At 19.7 minutes brightening of R9 can be observed along 2.05 – 2.15 m, 9.5 ns concurrent with W8 and W9 reaching the reflector.

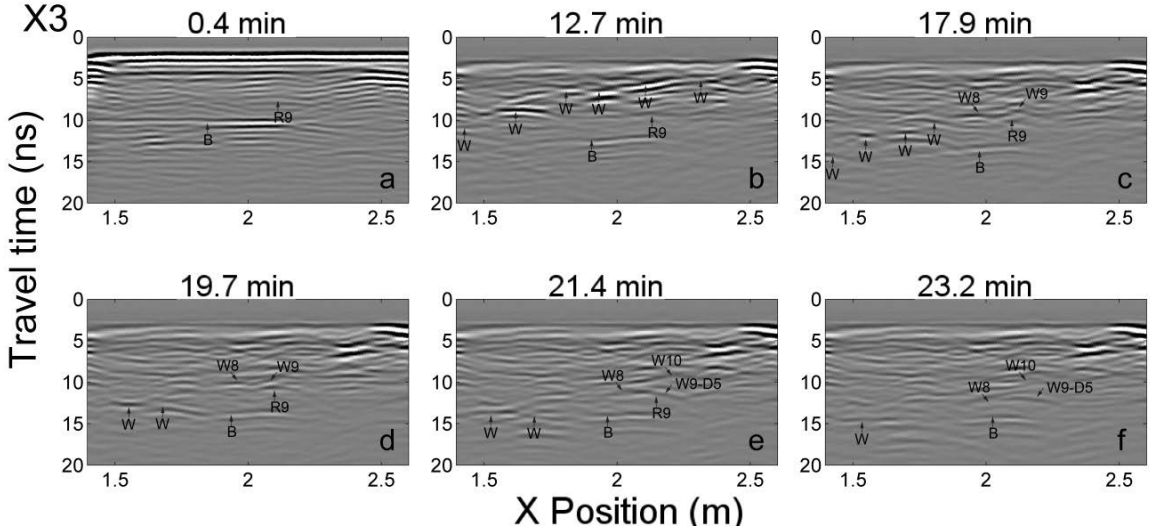

Figure 2.7. X3 profile set collected along Y = 2.0 m. Wetting front arrivals intersect a static reflector and manifest as a diffraction (D5) in the Y6 profiles.

The increase in amplitude along R9 at 21.4 min is seen at 2.15 m – 2.25 m, 11 ns. Inspection of Y6 at the corresponding time (Figure 2.5h) shows the emergence of D5 concurrent with W9 reaching R9. W9/R9 does not appear as a diffraction in the X3 profiles, indicating that the geometry of the anomalous body is likely linear along the X-direction and approximates a point-object in the Y-direction. The wetting front which advanced directly downward at 2.20 – 2.25 m (W10) is found at travel time of 9.6 ns (21.4 mins) and 10 ns (23.2), earlier than the W9/R9 arrivals, suggesting that water from W9 has travelled laterally along R9 in a finger-like manner and manifests as the D5 arrival in the Y-profiles.

The X5 profiles collected along Y = 2.70 m, shown in Figure 2.8, shows the origin of the D3 arrival to be lateral shifting of arrivals as they interact with static reflectors, similar to D5. Two intra-sand reflectors, the R10 reflector located at 1.65 m – 1.9 m, 6 ns

and the R11 reflector at 1.95 m – 2.2 m, 6.5 ns (Figure 2.8a), are adjacent to one another but not continuous. The wetting front progresses uniformly until 14.8 minutes (Figure 2.8b), at which point the wetting front reflection (W11) arrives simultaneously with R10 and another distinct reflection (W12) is evident from 1.95 m to 2.1 m, 8 ns.

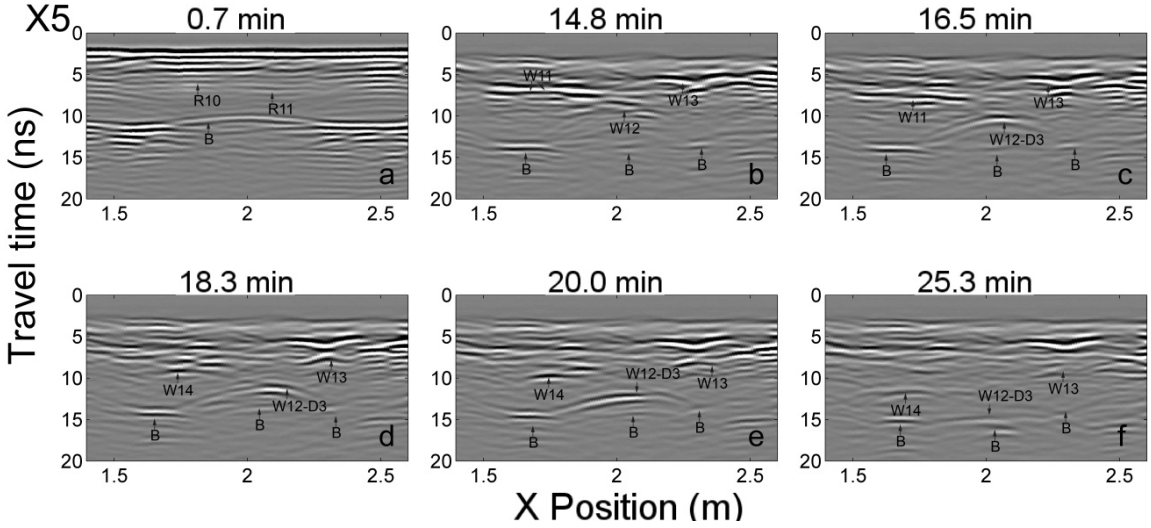

Figure 2.8. X5 profile set collected along Y = 2.60 m. A discrete transient wetting front arrival (W12) emerges in the center of the profile and is observed as a diffraction (D3) in the Y3 profile set.

Above 2.25 m position, the wetting front arrives earlier than W11 at 6 – 6.5 ns (W13). W12 increases in travel time from 14.8 to 16.5 minutes, while W11 remains at the R10 location. W11/R10 display a decrease in amplitude between 14.8 and 16.5 minutes and, interestingly, the W12 arrival now appears as a diffraction with a broad apex.

This pattern suggests that flow has been stalled along R10 and R11 and a discrete finger from 2.0 m to 2.1 m emerged, perhaps due to channeling of flow along R10 and R11. The emergence of W12 correlates with the appearance of D3 in the Y3 profiles at 17.2 minutes, though the arrival is faint until 18.9 minutes (Figure 2.5g). At 18.3 minutes,

W12/D3 increases in travel time to 10.5 ns and retains its hyperbolic appearance. As the wetting front passes R10, W11 is no longer distinct but discrete sub-horizontal wetting front arrivals (W14) develop under R10 and propagate with a slower change in travel time than W12/D3. The broad apex of W12/D3 increases in position from 1.95 m – 2.10 m at 16.5 minutes to 2.05 m – 2.16 m at 18.3 minutes, followed by high amplitudes appearing at lower position (1.85 m – 2.10 m) along the inclined portion of the arrival after 20.0 minutes (Figure 2.8e). At 25.3 minutes, W12-D3 arrives at 14.3 ns at 2.0 m position, concurrent with B arrivals at 1.7 and 2.3 m and earlier than B at 2.1 m position, 16 ns. The adjacent W13 and W14 arrivals are significantly earlier than W12-D3, and water content probe data indicates the front was around 0.30 – 0.40 m depth at X = 1.50 and X = 2.50. The B arrival directly under W12-D3 displays an amplitude increase, indicating water may be accumulating along the base-of-sand, though this interpretation cannot be verified from the probe data.

2.4 Discussion

The GPR data collected during Experiment 1 offer detailed insight into the complex nature of unsaturated flow. Evidence of non-uniform flow is abundant in the radar profiles. If a 1-D flow system with uniform water content behind the wetting front is assumed, then the two-way travel time to the base of sand will increase as a function of the wetted zone thickness. Extrapolating to 2-D and 3-D, the base of sand arrival would increase in travel time uniformly at all locations. Under variable applied flux and stable matrix flow, the shape of the wetting front is expected to be controlled by the applied flux and the corresponding GPR profile would capture a continuous reflecting interface

propagating with increased travel time (e.g. Vellidis, et al. 1990). This is generally observed for the GPR profiles (Figure 2.2, Figure 2.5 - Figure 2.8), yet the presence of diffractions and evidence of lateral movement of water suggests that non-uniform flow is a consistent feature of our infiltration experiments.

Numerous diffraction hyperbolas suggest that flow is occurring as discrete fingers beyond the resolution of the GPR. These results stand in contrast to Truss, et al., in which hyperbolic arrivals were observed only when rubble, tree roots, and sand-filled dissolution features in the oolitic limestone were present (2007) and to Haarder, et al. in which evidence of fingered flow through the sandy soil was observed in patterns of dye staining yet individual diffractions from flow fingers were absent in the GPR data (2011). Similarly, Allroggen, et al. (Allroggen et al., 2015) report the presence of flow fingers in soil profiles excavated during a dye-staining forced infiltration experiment but do not report phenomena in GPR data related to fingered flow. Here, the laboratory sand does not contain any material boundaries, yet from the abundance of diffraction hyperbolas the presence of discrete fingered flow can be inferred. The apparent delays and lateral shifts in transient wetting front arrivals as they interact with static reflectors may indicate shifts in flow along and around capillary barriers as sheets or as finger-like channels. For instance, arrival W9-D5's orientation-dependent appearance suggests that a reflecting body was planar with respect to the X-axis but approximated a point relative to the the Y-axis, i.e. a lateral finger. The observed elongation of W9-D5 along reflector R9 suggests channeling along the interface. Similar channeling of flow may explain the apparent bypass flow of Experiment 2, though it is unclear why it did not occur during Experiment

1. The Y1 profiles (not shown) display a strong lateral deflection of the wetting front at Y = 2.0 m toward lower Y positions, though the wetting front can be traced directly downward through the sand at Y = 2.00 m in Experiment 1 and no bypass is evident. The initial water content varied by less than 0.015 vol/vol between experiments, so it remains unclear if the rapid transport of water in probe array A1 during Experiment 2 was due to the slightly higher antecedent moisture, an uncharacterized anomaly in irrigation flux between experiments, or is the result of other factors.

The wealth of features suggesting non-uniform flow in this simple sand system give hope that the identification of preferential flow mechanisms is possible using time-lapse monitoring methods. Unfortunately, the source of the non-uniform flow features is left to interpretation and cannot be independently verified, as in a dye-staining experiment. Use of high-frequency 1000 MHz antennas in this study may have enabled such detailed capture of small-scale structure and flow phenomena, as similar work has utilized lower-frequency (250 – 500 MHz) antennas (Allroggen et al., 2015; Haarder et al., 2011; Truss et al., 2007). Monitoring with higher frequencies (1000+ MHz) may be more suitable for capturing details of complex flow systems, though the obvious limitation in signal penetration at higher frequencies may not be adequate in many circumstances.

Migration methods may help mitigate the resolution limitations by focusing energy to its proper place in the subsurface and collapsing diffraction hyperbolas (Yilmaz, 2001). A properly migrated GPR image could enhance interpretation of flow processes and may capture individual preferential flow phenomena and enable quantitative geometrical description of such features. Migration algorithms necessitate a model of wave velocity,

and due to the sharp lateral and vertical contrasts in velocity between wetted and dry zones in our data from non-uniform flow, constant velocity migration is likely inadequate. Velocity estimation from diffraction hyperbolas is problematic as diffractions are sparse and spread unevenly in space. The development of velocity estimation using changes in travel time and their application to migration of 2D GPR data is the focus of subsequent chapters.

This study demonstrates the necessity of time-lapse imaging for interpretation of flow phenomena. Proper identification of arrivals in a single profile with the aid of time-adjacent information can be difficult; without time-lapse information analysis of these dynamic events becomes guesswork. A trade-off exists between spatial and temporal coverage in time-lapse monitoring. In Experiment 1, profiles were collected along 12 lines in about 1.75 minutes with spacing of 0.10 – 0.30 m between adjacent lines, which is a significant achievement and results in the ability to identify the origin of anomalous arrivals as lateral flow between perpendicular profiles (e.g. W12-D3, W9-D5). The capture of these events was coincidental, however, and other arrivals in the data cannot be similarly investigated using adjacent perpendicular profiles. Pseudo-3D or full-3D data collection over the same area would certainly result in a richer data set and improve capture of flow features, but the time required to collect such data would increase and, in the case of our experiments, not approximate a static image of the subsurface. Even with the automated positioning system, attempts to image transient flow features in a highly dynamic system in 3D may fall short.

2.5 Conclusion

Time-lapse monitoring of hydrologic processes with GPR holds promise for identifying mechanisms of non-uniform and preferential flow through the vadose zone. Two infiltration experiments were performed in a tank filled with uniform sand and monitored with GPR. Patterns of flow in embedded water content probes reflect the distribution of flux to the sand surface, with quicker rates of wetting front movement associated with areas of higher flux. Rapid transport of water and bypass of portions of the sand are evident in moisture probe data from the second experiment, indicating that flow is non-uniform through the homogenous sand and is most rapid in one corner of the irrigated area.

The results of the first experiment show numerous arrivals in GPR data indicative of discrete flow fingers and lateral flow of water along intra-sand boundaries identifiable as static reflectors. Use of high-frequency 1000 MHz antennas may have enabled the identification of non-uniform flow features absent from other studies. Monitoring with perpendicular 2D profiles enables interpretation of anomalous arrivals in multiple dimensions and yields insights into the complexity of flow through the sand. The approach utilized here cannot independently verify these interpretations, so the method may be improved by performing dye-staining or other tracer tests or use of combined geophysical monitoring methods. The sparse spatial GPR sampling of Experiment 1 permits rapid temporal sampling while retaining plentiful information about the 3D flow system.

The wetting front in these experiments is not well approximated as a horizontal, continuous interface across the irrigated zone. The concentration of flux within the irrigated area creates significant 3D variability in the wetted zone geometry and the possibility for fingered flow indicates the wet-dry interface may be quite complex. Consequently, methods for quantifying wave velocity and soil water content based on these assumptions, such as NMO-based methods, may be problematic.

2.6 Works Cited

Allroggen, N., van Schaik, N., Tronicke, J., 2015. 4D ground-penetrating radar during a plot scale dye tracer experiment. Journal of Applied Geophysics, 118: 139-144. DOI:10.1016/j.jappgeo.2015.04.016

Binley, A., Winship, P., Middleton, R., Pokar, M., West, J., 2001. High-resolution characterization of vadose zone dynamics using cross-borehole radar. Water Resources Research, 37(11): 2639-2652. DOI:10.1029/2000wr000089

Binley, A., Winship, P., West, L.J., Pokar, M., Middleton, R., 2002. Seasonal variation of moisture content in unsaturated sandstone inferred from borehole radar and resistivity profiles. Journal of Hydrology, 267(3-4): 160-172. DOI:10.1016/s0022-1694(02)00147-6

Glaser, D.R., Werkema, D.D., Versteeg, R.J., Henderson, R.D., Rucker, D.F., 2012. Temporal GPR imaging of an ethanol release within a laboratory-scaled sand tank. Journal of Applied Geophysics, 86: 133-145. DOI:10.1016/j.jappgeo.2012.07.016

Haarder, E.B., Looms, M.C., Jensen, K.H., Nielsen, L., 2011. Visualizing Unsaturated Flow Phenomena Using High-Resolution Reflection Ground Penetrating Radar. Vadose Zone Journal, 10(1): 84-97. DOI:10.2136/vzj2009.0188

Mangel, A.R., Lytle, B.A., Moysey, S.M.J., 2015. Automated high-resolution GPR data collection for monitoring dynamic hydrologic processes in two and three dimensions. The Leading Edge, 34(2): 190-196. DOI:http://dx.doi.org/10.1190/tle34020190.1

Mangel, A.R., Moysey, S.M.J., Ryan, J.C., Tarbutton, J.A., 2012. Multi-offset ground-penetrating radar imaging of a lab-scale infiltration test. Hydrology and Earth System Sciences, 16(11): 4009-4022. DOI:10.5194/hess-16-4009-2012

Moysey, S.M.J., 2010. Hydrologic trajectories in transient ground-penetrating-radar reflection data. Geophysics, 75(4): WA211-WA219. DOI:10.1190/1.3463416

Steelman, C.M., Endres, A.L., 2012. Assessing vertical soil moisture dynamics using multi-frequency GPR common-midpoint soundings. Journal of Hydrology, 436: 51-66. DOI:10.1016/j.jhydrol.2012.02.041

Steelman, C.M., Endres, A.L., Jones, J.P., 2012. High-resolution ground-penetrating radar monitoring of soil moisture dynamics: Field results, interpretation, and comparison with unsaturated flow model. Water Resources Research, 48: 17. DOI:10.1029/2011wr011414

Truss, S., Grasmueck, M., Vega, S., Viggiano, D.A., 2007. Imaging rainfall drainage within the Miami oolitic limestone using high-resolution time-lapse ground-penetrating radar. Water Resources Research, 43(3): 15. DOI:10.1029/2005wr004395

Vellidis, G., Smith, M.C., Thomas, D.L., Asmussen, L.E., 1990. Detecting wetting front movement in a sandy soil with ground-penetrating radar. Transactions of the Asae, 33(6): 1867-1874.

Versteeg, R., Birken, R., 2001. An automated facility to study processes using 4D GPR, Symposium on the Application

of Geophysics to Engineering and Environmental

Problems (SAGEEP).

Yilmaz, O., 2001. Seismic Data Analysis: Processing, Inversion, and Interpretation of Seismic Data. Society of Exploration Geophysicists, Tulsa, OK, 2065 pp.

CHAPTER 3

COMBINED MULTI-OFFSET AND CONSTANT-OFFSET TIME-LAPSE MONITORING OF INFILTRATION USING GROUND PENETRATING RADAR

3.1 Abstract

Time lapse monitoring using surface-based ground GPR has been utilized for imaging non-uniform and preferential flow in the unsaturated zone and for estimation of bulk system parameters, such as volumetric water content, using a variety of single and multi-offset methods (Allroggen et al., 2015; Grote et al., 2002; Haarder et al., 2011; Lunt et al., 2005; Mangel et al., 2012; Steelman et al., 2012; Truss et al., 2007). This chapter evaluates a methodology which incorporates multi-offset velocity analysis with single offset velocity estimation to track spatial and temporal changes in the velocity during infiltration tests performed in a vadose zone analog consisting of a wooden tank filled with homogenous river sand. The sand was irrigated for 22 minutes using a system of micro-sprayers mounted to PVC pipes and monitored with an array of *in situ* water content probes as well as with automated time-lapse GPR profiling as repeated sets of common midpoint profiles (CMPs) for performing velocity analysis and constant offset profiles (COP's) for viewing changes in 2D distribution of reflectors. Estimates of the bulk GPR velocity and water content are made from the single-offset GPR profiles by tracking the changes in arrival time to reflectors and compared to the estimates from multi-offset gathers and water content probes. Collecting data as repeated CMPs and COPs, along with the single offset velocity analysis method, enables the identification

and interpretation of complex flow phenomena from the GPR images while providing the ability to describe bulk water content conditions within the measurement area more reliably than multi-offset methods and with good agreement to water content probe data.

3.2 Introduction

Unsaturated flow is influenced by variability in the pore structure, which can lead to preferential flows that are concentrated in discrete locations and bypass most of the soil matrix (Hendrickx et al., 2001). As standard models of flow (e.g. those based on Richards equation (1931)) cannot predict the occurrence of unstable wetting fronts in homogenous systems and traditional hydrologic measurements are generally invasive and limited in spatial extent, the application of noninvasive geophysical methods hold promise for monitoring, interpreting, and quantifying infiltration and preferential flow through soil. Ground penetrating radar (GPR) is a tool with a high sensitivity to soil moisture, thus GPR has been demonstrated as a non-invasive method for estimating volumetric soil water content in a variety of conditions (Bradford, 2008; Brosten et al., 2009; Garambois et al., 2002; Grote et al., 2005; Grote et al., 2002; Lunt et al., 2005; Mangel et al., 2012; Steelman et al., 2012; Turesson, 2006).

Time lapse monitoring using surface-based ground GPR has been utilized for imaging non-uniform and preferential flow in the unsaturated zone (Allroggen et al., 2015; Haarder et al., 2011; Truss et al., 2007). Past time-lapse studies listed vary in their ability to resolve and describe the geometry of preferential flow features and generally rely on destructive methods to verify interpretations of their data (e.g. excavation following dye-staining experiments). They also vary in the resolution of the spatial

distribution of water and verification of soil water estimates following infiltration events. Truss, et al. (2007) performed an infiltration experiment into the Miami limestone and observed a number of diffraction features in the GPR data which the authors attributed to preferential flow through the root zone, rubble, and dissolution fingers in the unsaturated rock. They estimated the bulk water content in the rock using diffraction hyperbolas present in GPR profiles, though their estimates were not corroborated with other data. A dye-tracer experiment was performed by Haarder, et al. (2011) in sandy deposits in which fingered flow was observed in the dye-stain patterns in excavated trenches following infiltration. The predicted GPR response from fingered flow was simulated, but these features were not observed in the data collected during infiltration. Water content was measured in several soil samples following excavation and compared to patterns in the GPR data, providing a description of the system at a single time. Allroggen, et al. (Allroggen et al., 2015) performed a similar dye-staining experiment. The authors tracked increases in the travel time to specific reflecting interfaces and used these to estimate the bulk water content. Changes in travel time were interpreted to be caused to be the preferential movement of water and was verified in the observed dye-staining patterns. Upon excavation of the soil, the authors observed flow fingers in the dyed soil cross-sections but did not detect fingered flow with GPR. These studies indicate that the simultaneous non-destructive monitoring and identification of preferential flow phenomena, analysis of the geometry of preferential flow features, and assessment of the distribution of soil moisture under these conditions remains a challenge.

Quantitative descriptions of soil water content using GPR are achieved using the relationship between radar wave velocity and volumetric water content. The transmitted electromagnetic wave from a radar antenna travels through the earth with a velocity defined by the electromagnetic properties. Commonly, earth materials are assumed to be non-conductive ($\sigma < 10$ mS/m), in which case the wave velocity (V) is related to the real part of the material's relative dielectric permittivity (k) and speed of light in a vacuum (c = 0.3 m/ns) by (Davis and Annan, 1989):

$$V = \frac{c}{\sqrt{\varepsilon_r}} \tag{3.1}$$

As the relative permittivity of air (ε_r = 1) and mineral grains (ε_r = 3-10) are lower than that of water (ε_r = 81) (Buchner et al., 1999), the bulk material permittivity of a soil is strongly related to the volumetric water content when unsaturated and porosity when saturated. Petrophysical relationships can then be utilized to estimate the water content (θ) of the medium from the relative permittivity, such as the well-known Topp equation (Topp et al., 1980) and variants of this relationship (Ferre et al., 1996) .

Velocity determination can be accomplished via several GPR analysis methods, each with accompanying strengths and limitations (see Huisman, et al. (2003) for a review). Estimation methods can generally be categorized by data collection geometry (single-offset or multi-offset) and whether measurements are surface-based or made within. Surface-based methods rely on reflected energy to characterize average water content to the depth of the reflector. In single offset data, the wave velocity can be estimated by fitting diffraction hyperbolas to observed scattering in a profile (Grote et al., 2002; Mount

et al., 2014) or the travel time to a reflector at known depth can be determined (Grote et al., 2005; Lunt et al., 2005; Stoffregen et al., 2002). These methods enable data to be collected rapidly but are limited by the spatial distribution of scattering objects reflectors at known depths within the survey area.

Multi-offset collection geometries have been successfully used to characterize soil moisture in a variety of scenarios (Becht et al., 2006; Garambois et al., 2002; Jacob and Hermance, 2004; Steelman and Endres, 2012; Steelman et al., 2012; Turesson, 2006). These methods typically analyze the velocity similar to seismic surveys (Yilmaz, 2001) in which the hyperbolic trajectory of reflected arrivals, termed the normal moveout (NMO), is analyzed in a multi-offset GPR gather to estimate the wave velocity. Though limited to areas in which subsurface reflectors are present, the depths of reflecting interfaces need not be known. These methods require increased time and effort to position the antennas for proper data collection, thus their use has been less common in time-lapse monitoring studies of unsaturated flow. Recent studies demonstrate that improvements in rapid automated positioning of antennas can overcome this limitation (Mangel et al., 2015; Mangel et al., 2012). In some cases, simplifying assumptions have been made to meet the necessary geometrical requirements of the velocity analysis (e.g. horizontal layers of broad extent) by representing flow as a 1-D system (Steelman 2012, Mangel 2012). Non-uniform and preferential flow would violate this geometry, and thus the water content values derived would be suspect.

Tracking travel time changes to specific interfaces has been demonstrated as a means to identify relative changes in bulk water content (Allroggen et al., 2015; Haarder

et al., 2011; Truss et al., 2007). Haarder et al. (2011) used the differences in travel time to specific interfaces before and after an irrigation experiment to infer the spatial distribution of water during infiltration and directly compared the travel time difference plots with moisture content samples. The authors mention that the travel time changes can be used to estimate water content directly but do not report any such results. The study results also suggest that reflecting interfaces are more suitable for velocity estimation than reliance on scattering objects, as discrete flow fingers were present in dye-staining patterns but caused no diffractions in the GPR data. Allroggen et al. (2015) similarly demonstrate that tracking changes in travel time to unique horizons during infiltration experiments can be used to map relative changes in the soil moisture between horizons and, from patterns in travel time data, infer the vertical extent of infiltrated water which was verified by dye staining. Estimates of the total infiltrated water volume were consistent with the actual value. The limitation is, again, the need for a priori information regarding reflector depths in order for accurate description of the subsurface geometry to quantify absolute water content and not strictly relative changes.

Multi-offset velocity estimation methods are less common in time-lapse monitoring studies of unsaturated flow due to the intensive data collection requirements, though recent studies demonstrate that improvements in rapid automated positioning of antennas can overcome this limitation (Mangel et al., 2015; Mangel et al., 2012). In some cases, simplifying assumptions have been made to meet the necessary geometrical requirements (e.g. horizontal layers of broad extent) by representing flow as a 1-D system (Steelman 2012, Mangel 2012). Non-uniform and preferential flow would violate this geometry, and

thus the water content values derived would be suspect. Steelman et al. (2012) investigated integrated single-offset and multi-offset monitoring of seasonal water content changes. The authors demonstrate that by combining these data collection methods the fluctuation of actual bulk water content within horizons in GPR data could be made with good agreement to model predicted values, though independent verification of water content at depth was not made. The study focuses on seasonal variability, thus replicate profiles were collected on the scale of days to weeks and the influence of non-uniform and preferential flow during individual infiltration events on the performance of combined monitoring is yet to be assessed.

The work presented here proposes and evaluates a methodology which incorporates multi-offset velocity analysis with single offset velocity estimation to track spatial and temporal changes in the velocity distribution during infiltration tests performed in a vadose zone analog. It is proposed that combining data collection in this way facilitates interpretation of complex flow phenomena while retaining the ability to accurately describe water content conditions within the measurement area. The single-offset profiles are analyzed for evidence of non-uniform flow by tracking the changes in transient arrivals during irrigation of the sand. Both the single- and multi-offset estimates of bulk water content are compared against *in situ* water content probe measurements. The multi-offset GPR profiles are examined to assess how non-uniform flow affects the accuracy of bulk water content estimates and how the flow system affects both the spatial and temporal patterns in water content estimates. Bulk water content estimates are made from

the single-offset GPR profiles by tracking the changes in arrival time to reflectors and compared to the estimates from multi-offset gathers.

3.3 Methods

3.3.1 Experimental Procedure

A forced infiltration experiment in which irrigation was applied to the surface of a large tank (4 m x 4 m x 2 m) filled with 0.60 m of homogenous river sand was monitored with time-lapse GPR The tank is equipped with a drainage system consisting of 16 – 1 m x 1 m cells which drain independently to the exterior of the tank, and an impermeable liner separates the sand from a gravel-filled zone used to support the drains. Irrigation for the experiments was applied using two 1.5 m-long sprayer arrays consisting of micro-sprayers mounted to PVC pipes. The micro sprayers collectively irrigate a central area measuring approximately 2.25 m^2. The volumetric flux applied to the sand surface was controlled at 8 liters/min, or an effective flux of 3.56 mm/min across the irrigated area.

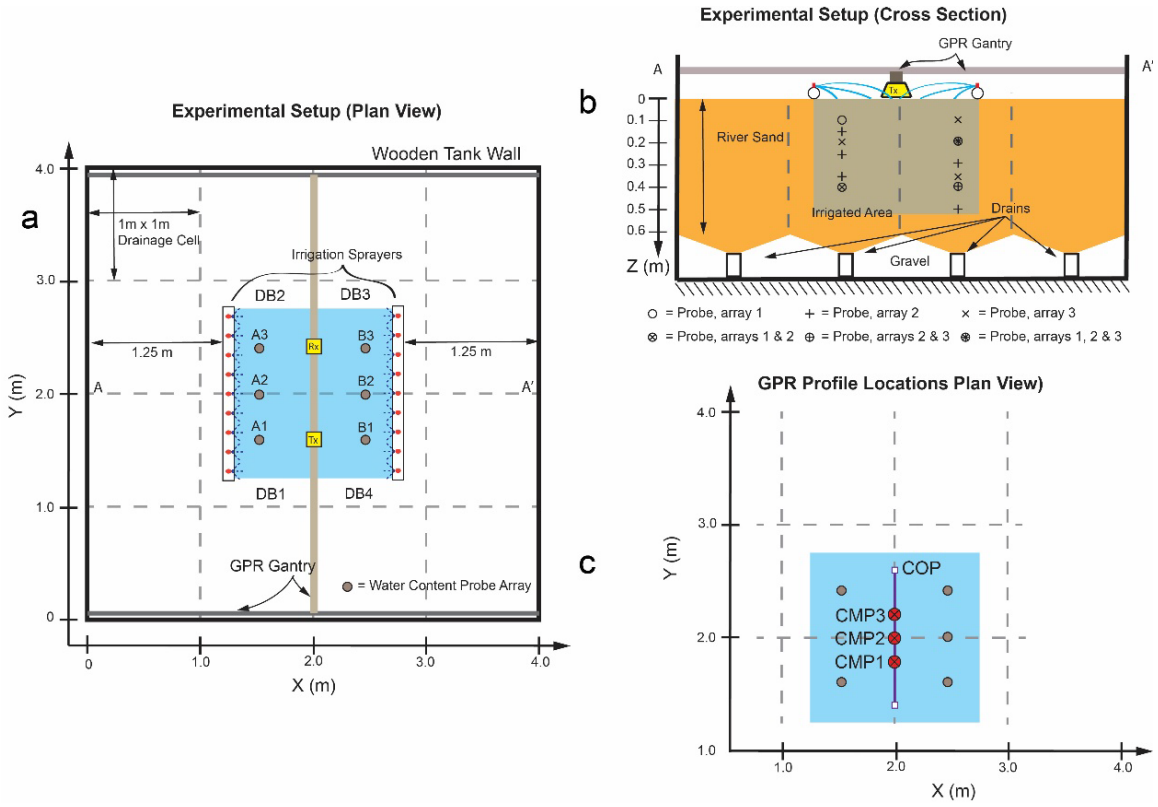

Figure 3.1. Experimental setup. a) Plan view of the tank showing positions of the irrigation sprayers, drainage bays (DB1-DB4), automated GPR gantry, and six vertical arrays of water content probes at various depths in the sand (A1-B3). b) Cross-section through the tank center illustrating the probe locations. c) Detail of the irrigated area and positions of GPR profiles collected during the experiment.

The volumetric water content of the sand was monitored using Decagon EC-5 water content probes placed horizontally in the sand as vertical arrays in six locations with various depths shown in Figures 3.1a-b and summarized in Table 3.1. The array positions within the irrigated area were selected to minimize interference of reflections from water content probes in the GPR profiles. Water content measurements at each probe were recorded at 10-second intervals.

Table 3.1. Locations of water content probe arrays and probe depths within the experimental tank.

Array	X-Y Position (m)	Probe Depths (m)	Array	X-Y Position (m)	Probe Depths (m)
A1	[1.50, 1.60]	0.10, 0.40	B1	[2.50, 1.60]	0.20, 0.40
A2	[1.50, 2.00]	0.15, 0.25, 0.35	B2	[2.50, 2.00]	0.20, 0.30, 0.40, 0.50
A3	[1.50, 2.40]	0.20, 0.40	B3	[2.50, 2.40]	0.10, 0.20, 0.35

Time-lapse GPR data were continuously collected within the irrigated area as a cycle of three common midpoint (CMP) surveys followed by one constant offset profile (COP) using an automated gantry system to automatically position the antennas as shown in Figure 3.1c and described in Table 3.2. Offsets for the CMPs varied from 0.16 to 1.00 m, and the COP offset was 0.16 m. Traces were collected every 0.01 m. The four-profile cycle was repeated 100 times over approximately 23 minutes, with 14-15 seconds elapsing per cycle and 142,695 traces collected in total.

Table 3.2. Positions of profiles collected during Experiment 1.

Initial X-Y position (m)	Final X-Y Position (m)	Offset (m)	Name
[2.00, 1.75]	[2.00, 1.75]	0.16 – 1.00	CMP1
[2.00, 2.00]	[2.00, 2.00]	0.16 – 1.00	CMP2
[2.00, 2.25]	[2.00, 2.25]	0.16 – 1.00	CMP3
[2.00, 1.50]	[2.00, 2.50]	0.16	COP

A detailed description of the automated gantry system can be found in (Mangel et al., 2015). These experiments were performed with an updated version of the gantry system utilizing a fiberglass central rail, rather than aluminum, to minimize interference. 1000 MHz shielded antennas (Sensors and Software) were used to obtain the highest-resolution data possible. A time sampling window of 25 ns was used along with 4 stacks per trace. Prior to irrigation, the sand surface was raked flat to ensure good coupling of

the radar antennas with the ground. Irrigation began one minute after the start of GPR data collection and terminated after 23 minutes.

3.3.2 Normal Moveout Velocity Analysis of CMPs

GPR arrivals from a horizontal reflector in a multi-offset gather increase in travel time with increasing offset following a hyperbolic trajectory known as the normal move out (NMO). The curvature of the trajectory is related to the average, i.e. root mean square (RMS) velocity of the medium. The squares of two-way travel time (t), source-receiver offset (d), reflector depth (h), and RMS velocity of the medium (V_{RMS}) are related through the equation:

$$t^2 = \frac{d^2}{V_{RMS}^2} + \frac{4h^2}{V_{RMS}^2} \tag{3.2}$$

In this work, the travel times of the first-break arrivals of a reflection from the sand-gravel interface at the bottom of the tank are picked to estimate the RMS velocity within the sand layer. Additionally, picks of a particular arrival were checked for consistency with respect to continuity across offset in CMPs, across position in COPs, and through experimental time as sets of replicate traces collected at the same position and offset, here termed trajectory images. This evaluation of reflection consistency across gathers improves interpretation of arrivals in noisy data. A least-squares best-fit line (Eq. 3.2) is fit to the travel time picks in the d^2-t^2 domain to obtain V_{RMS} and reflector depth.

Non-uniform propagation of a wetted low velocity layer through the soil would result in a more complicated geometry than is assumed in NMO analysis. A simple

method is therefore used here to estimate spatial and temporal velocity variations associated with the wetting front migration through time within an otherwise uniform soil layer. This procedure consists of two steps. First, average lateral velocity variations across the tank over the course of the infiltration event are estimated using shifts in travel-time for a reflector at a fixed (but potentially unknown) depth, which in this study is the sand-gravel interface at the base of the tank. This step of the procedure combines the initial, i.e. prior to infiltration, average velocity (and reflector depth if unknown) obtained with multi-offset NMO analysis with local travel-time differences observed in repeated constant-offset profiles during infiltration. In the second step of the procedure, the Dix equation (Dix, 1955) is used to estimate the velocity of the wetted zone at any time and location along the profile.

The initial V_{RMS} values for the dry soil layer (i.e., the sand in this experiment) estimated from the CMPs are assigned to all the points in the profiled area. We assume that this velocity is approximately homogenous prior to the infiltration event, though in this study, the initial V_{RMS} was interpolated across the profile from the initial RMS velocities determined from NMO analysis of the three CMPs. The difference between the travel-time to the interface prior to wetting (t_0) and the travel-time ($t_k(x)$) observed in a profile collected at a later time during the infiltration event (T) can be used to estimate an incremental change in velocity at any location and time during the experiment ($\Delta V(x,T)$):

$$\Delta V(x,T) = 2\left(\frac{1}{t_k(x)} - \frac{1}{t_0}\right)\left(h^2 + \left(\frac{1}{2}d\right)^2\right)^{1/2} \tag{3.3}$$

The velocity $V(x,T)$ at time T is found by adding the change in velocity $\Delta V(x,T)$ to the initial (V_0):

$$V(x,T) = V_0 + \Delta V(x,T) \tag{3.4}$$

This step of the procedure results in a 1D distribution of the RMS velocity for each position in the profiled area. The Dix equation (Dix, 1955; Yilmaz, 2001) is used to estimate the interval (i.e., layer) velocities ($V_{n\text{-}int}$) for a series of n horizontal, flat layers from the RMS velocities (V_n) and reflection arrival times (t_n) from reflections originating from the top and bottom of the nth layer:

$$V_{int}^{n}(x,T) = \left(\frac{V_n^2 t_n - V_{n-1}^2 t_{n-1}}{t_n - t_{n-1}}\right)^{1/2} \tag{3.5}$$

An assumption that the initial velocity conditions in the sand profile are uniform prior to irrigation allows the initial RMS velocity to represent the dry sand velocity ahead of the wetting front. The travel times to the bottom of the dry layer and wetted zone are tracked in replicate COPs, allowing the unknown wetted interval velocity to be determined using Equation 3.5. Once the interval velocity of the wetted zone is known, petrophysical relationships can be utilized to estimate the water content (θ) in this region. In this study, the relationship given by Ferre, et. al. which, for a broad range of water contents gives similar results to the Topp equation, is used (Ferre et al., 1996):

$$\theta = 0.1181 \frac{c}{V_{int}^{n}(x,T)} - 0.1841 \tag{3.7}$$

3.4 Results

3.4.1 Irrigation Flux Characterization

The results of the spatial flux characterization are illustrated in Figure 3.2. The mean flux was 2.20 mm/min with standard deviation of 1.76 mm/min, i.e. substantially less than the target applied flux of 3.56 mm/min. Fluxes are generally higher (1.0 – 7.0 mm/min) in a zone from 1.30 m – 1.85 m Y position, with several hot spots receiving up to 13.4 mm/min flux (600% of mean). Fluxes are lower in the center of the irrigated area, receiving 0.05 – 0.20 mm/min. The flux applied to the moisture probe locations varied and was highest in the area surrounding the A1 probe array.

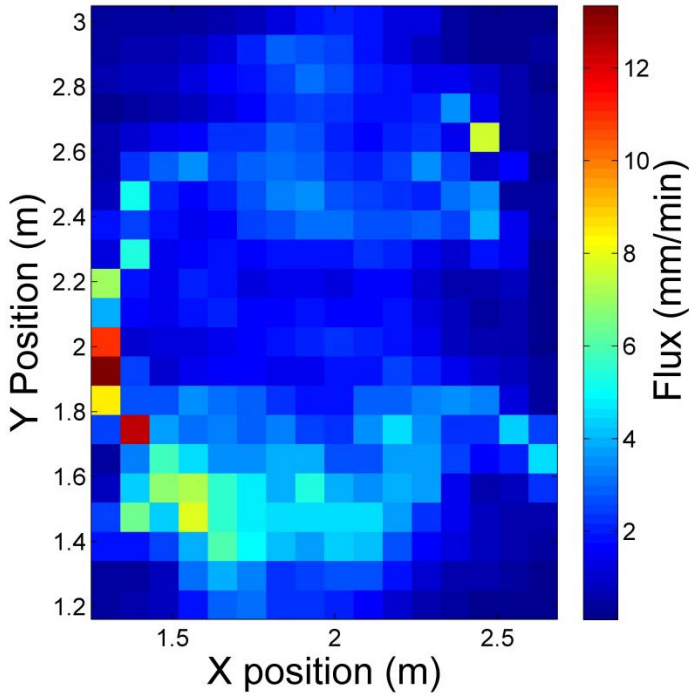

Figure 3.2. Irrigation flux distribution, in mm/min, within the irrigated area.

3.4.2 Moisture Probe Data

Water content measurements during the experiment are grouped by position and shown in Figure 3.3. Initial water content values do not display a clear trend with depth or position and varied from from 0.034 to 0.083 vol/vol. Water content behind the wetting front was also variable from probe to probe, with a mean of 0.188 vol/vol and range of 0.13 to 0.27 vol/vol. The sand did not approach the saturation value of 0.35 at any location or depth. The wetting front generally advanced more rapidly in the A1-A3 probe arrays than in the B1-B3 probe arrays, and was fastest in the A1 array. A probe (B1, 0.20 m depth) displays rapid fluctuations in water content (Figure 3.3f) indicative of instrument error.

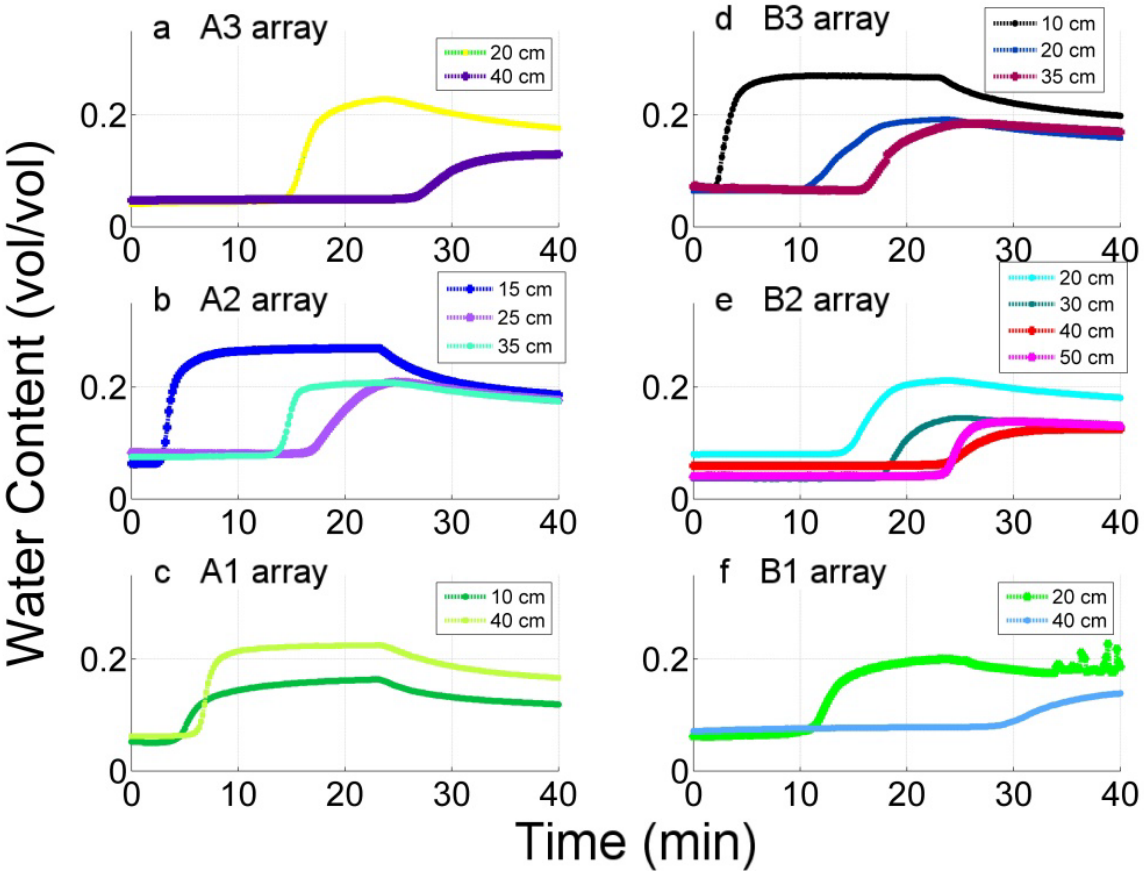

Figure 3.3. Water content probe measurements grouped by location.

The water content probe measurements indicate that the wetting front did not consistently pass shallower probes sooner than deeper probes. The wetting front passed the shallow probes (≤ 0.15 m depth) from 2.3 to 4.8 minutes, 0.20 m depth after 9.5 to 14.2 minutes, 0.25 – 0.35 m depth between 13.3 and 17.5 minutes, and 0.40 – 0.50 m depth between 5.3 and 28 minutes. The wetting front reached the A1(0.1m) probe at 4.3 minutes and the A1(0.4m) probe shortly after at 5.3 minutes. Preferential flow was evident in array A2 as the wetting front bypassed the shallower 0.25 m probe, arriving at 16 minutes, while the deeper 0.35 m probe measured the wetting front at 13 minutes.

Wetting was slower in array A3 than A1 and A2 and was more consistent with arrays B1-B3.

Table 3.3. Wetting front velocities from surface to water content probe.

Probe	Wetting velocity (mm/min)	Probe	Wetting velocity (mm/min)
A1(0.10m)	20.8	B1(0.40m)	13.9
A1(0.40m)	60.0	B2(0.20m)	13.2
A2(0.15m)	47.5	B2(0.30m)	16.8
A2(0.25m)	14.6	B2(0.40m)	16.3
A2(0.35m)	25.4	B2(0.50m)	20.8
A3(0.20m)	12.9	B3(0.10m)	42.9
A3(0.40m)	15.6	B3(0.20m)	16.2
B1(0.20m)	18.5	B3(0.35m)	21.7
Mean velocity	23.6 mm/min		

Estimates of the wetting front velocity in each array location were determined from the elapsed time from the sand surface to each probe and are contained in Table 3.3. The mean velocities were higher in the A arrays than B arrays, with the A1 probe array recording the highest propagation velocity of 60 mm/min. The trends in the Table 3.3 velocities are consistent with the flux patterns in Figure 3.2. Flux is highest above the A1 probes and propagation velocities are highest in this location during the experiment. Fluxes above the other probe arrays are more uniform, though the influence of a "hot-spot" at [2.45 m, 2.64 m] receiving 7.6 mm/min may account for the greater wetting front velocity observed in the B3 probes of 18.0 – 42.9 mm/min.

Table 3.4. Elapsed time between start of irrigation and observed drainage from the tank.

Drainage Bay	Drainage Observed (min)
DB1	21 min
DB2	31 min
DB3	40 min
DB4	35 min

Observed drainage sequences from the tank, contained in Table 3.4, describe trends of infiltration averaged over a larger volume than the water content probes and are less exact in time. However, they illustrate propagation of percolated water most rapidly in DB1 and DB2 consistent with the greater wetting velocities in the A1-A3 probe arrays. Drainage from DB1 was first at 21 min and was last observed at approximately twice these times from DB3 at 40 min. Drainage from DB4 closely followed DB2, with 4 minutes elapsed time during the experiment.

The water content probe data, observed drainage sequence, and wetting front propagation velocities describe a flow regime in which wetting of the sand and propagation of a wetting front is spatially non-uniform and strongly determined by the applied flux. The "southwest region of the irrigated area, i.e. around water content probe array A1 and drainage bay DB1 (see Figure 3.1a) reliably demonstrates the fastest transport of water through the sand, and wetting fronts in water content probes are generally sharp and suggest flow of water was downward with little lateral flow. However, the water content probes demonstrate that flow bypassed portions of the sand, though the mechanism by which this occurred cannot be inferred directly from the data.

3.4.3 Ground Penetrating Radar Profiles

Processing steps prior to analysis consist of an initial time-zero correction. All profiles are displayed without gain or additional processing applied. GPR data were collected using two survey geometries: the common midpoint (CMP) survey and constant-offset profile (COP). Arrivals in these profile types are generally common to one another; however, the appearance of a specific arrival will vary with respect to its dimension in the data, whether source-receiver offset or lateral position. The annotations used to denote unique arrivals in radar images are contained in Table 3.5.

Table 3.5. Description of annotated arrivals appearing in radar images.

Label	Description
G	Ground wave
B	Base of sand reflection
M	Base of gravel reflection
W	Wetting front reflection
D	Diffractions (from wetting front)

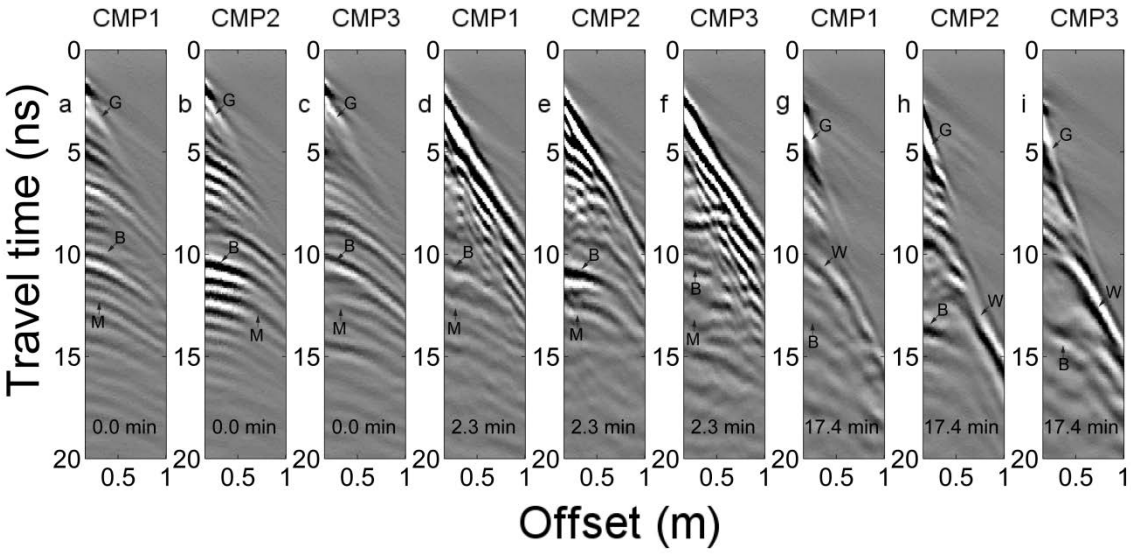

Figure 3.4. CMPs collected: (a-c) prior to irrigation of the tank, (d-f) after 1.3 minutes of irrigation (g-i) after 16.4 minutes of irrigation. Arrivals present in the profiles include the ground wave (G), reflection from the base of sand (B), and base of gravel reflection (M), and wetting front (W).

CMPs collected initially (i.e., prior to irrigation at 0 minutes) are shown in Figure 3.4a-c, after 1.3 minutes of irrigation are shown in Figure 3.4d-f, and after 16.4 minutes of irrigation are shown in Figure 3.4g-i. The initial CMPs show the arrivals observed under static, dry conditions within the tank. These include the direct ground wave (G) and several reflection events occurring from 6-14 ns. A reflection from the base of sand-top of gravel interface within the tank (B) is initially present in CMP1-CMP3 at approximately 9-10 ns travel time. Other reflections at 6-8 ns travel time are particularly strong in CMP2 and CMP3. These arrivals have an apparent depth of 35-40 cm, but are not originating from a known material interface within the soil column. Reflections originating from the base of the dry gravel beneath the sand arrive later, from approximately 12 to 14 ns.

Once irrigation begins, the B arrivals display irregularity in travel time with offset. A complicated set of arrivals are present following irrigation, from 1.7 to 4.0 minutes experiment time (0.7 to 3.0 minutes of irrigation) and appear concurrent with the ground wave and as late as 13 ns at the far offsets where they obscure the B arrival, particularly in CMP3 . After 4.0 minutes experiment time, these arrivals are no longer seen and another transient arrival with an irregular moveout is present which increases in travel time with increasing experimental time. As changes to the system are only due to irrigation, this arrival in interpreted as a reflection from the wet-dry interface along the bottom of the wetted zone and is labeled as W in Figures 3.4g-i. Reflection amplitudes

from this interface as well as the B arrival vary across offset and fluctuate during the experiment. The reflection moveout for both B and W do not follow a hyperbolic trajectory. After 15 minutes, the wetting front arrival is more clearly defined, especially in CMP3 around 10 ns. It appears to arrive concurrently with arrival B in CMP1 around 21 mins, in CMP2 after 22 mins, while remaining distinct from B in CMP3, suggesting that there is a variable rate of wetting front propagation within the irrigated area.

COPs collected prior to and at several times during irrigation are contained in Figures 3.5a-g, and the collections of traces with common position and offset (i.e., trajectory plots) are shown in Figures 3.5i-h. In these images, the non-uniform spatial propagation of transient arrivals is more clearly interpreted than from the CMPs. The direct ground wave (G) constitutes the first significant arrival at 1.5 ns. The sub-horizontal base of sand arrival B is present across the profile at 10 ns travel time and other moderately continuous reflectors are present within the sand. Upon irrigation, the early arrivals (2-5 ns) display a strong increase in amplitude coincident with overlapping, moderate amplitude diffraction tails (D arrivals in Figure 3.5b) that likely originate in the high amplitude wetted zone around 2-3 ns travel time. The D arrivals are first visible after 2 minutes experiment time (1 minute of irrigation) and persist until 10 minutes experiment. The wetting front reflection W is not easily distinguished from other arrivals until 8-10 minutes into the experiment at about 6 ns travel time. It remains generally coherent across the profile and increases in travel time with a consistent rate. At 14.3 minutes (Figure 3.5d), W displays significant discontinuity across the profile and is less distinct below Y = 1.90 m and between 2.20 m - 2.30 m position. The portion of the

wetting front arrival from 1.50 m - 1.65 m position increases travel time ahead of the rest of the front, arriving at 10 ns at Y = 1.50 m - 1.65 m and 7.8 – 9.0 ns along the remainder of the profiled area. Arrival B has a similar discontinuity across the profile, arriving latest at the lower Y positions.

W and B continue to arrive at later times throughout the experiment with greater discontinuity across the profile. This is most evident in the trajectory images in Figure 3.5g-I, where arrival W shows the steepest trajectory (i.e. the greatest rate of increase in travel time) at Y position 1.60 m. Arrival W intersects arrival B around 23 minutes into the profile at this location, while remaining separated by about 1 ns at Y = 2.00 m and by 4 ns at Y = 2.40 m. Together, the COPs and trajectory images display evidence of non-uniform propagation of transient arrivals with an increase in the apparent propagation rate as Y position increases.

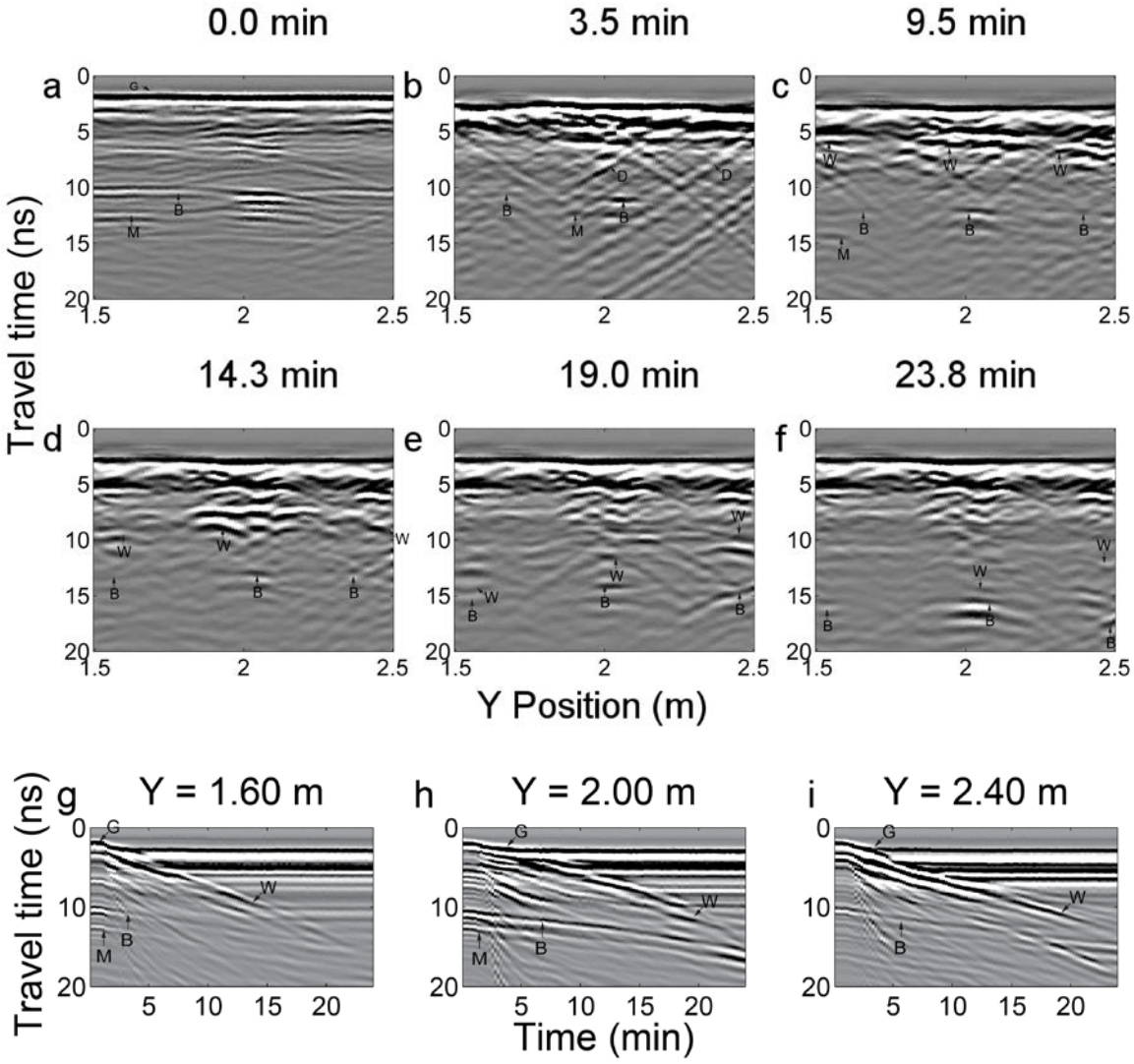

Figure 3.5. The COP-Y constant offset profiles collected (a) prior to and (b-f) during irrigation and the trajectory plots (g-i) at the locations of water content probe arrays.

3.4.4 Velocity Analysis

The RMS velocities evaluated using the base of sand reflection from CMP picks and travel-time derived velocities using picks of the base of sand reflection from COPs are shown in Figure 3.6 along with the estimated average velocity converted from the mean of all water content probes. Initial RMS velocity estimates were not uniform: 0.133 m/ns,

0.147 m/ns, and 0.130 m/ns in CMP1, CMP2, and CMP3, respectively. Final velocities were also unequal: 0.099 m/ns in CMP1, 0.087 m/ns in CMP2, and 0.093 m/ns in CMP3. The initial converted velocity from the water content probe data is 0.144 m/ns and final velocity of 0.099 m/ns. These values were obtained by first determining the volume-weighted average of water content measures in the probes. The weighting factor was determined by dividing volume of three-dimensional region nearest to each probe by the total volume of the irrigated zone (i.e. 1.35 m^3). Each water content measurement was multiplied by the weighting factor, and all measurements were summed to create a weighted average which was converted to velocity using the Ferre form of the Topp equation (Equation 3.7).

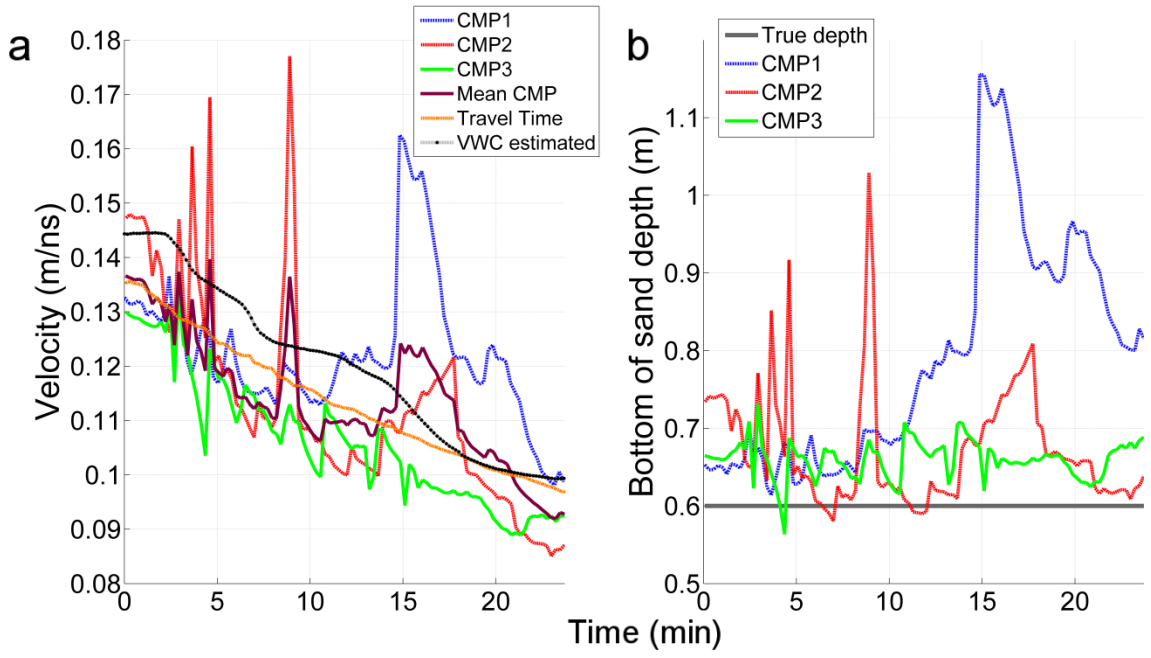

Figure 3.6. a) RMS velocity estimated from NMO analysis of CMP's, average velocity from travel time changes, and estimated mean velocity converted from

water content measurements. b) Estimated depth to the bottom of sand reflector, true depth is 0.60 m.

The general trend of Figure 3.6 shows a decrease in RMS velocity in all three CMPs during the experiment due to the increase in bulk water content of the sand with a slope approximating that of the water content velocity. The RMS velocities show fairly good agreement with the estimated mean velocity overall; however, the RMS velocities were generally lower than the estimated mean by 0.005-0.015 m/ns. Initially, two of three RMS velocities were around 0.01 m/ns slower than the estimated mean, and final RMS velocities were all less than the estimated mean by as much as 0.014 m/ns in CMP2. The agreement is best in CMP3, which is consistently lower than the water content velocity trend by about 0.015 m/ns. The travel-time velocity estimation shows a steady decrease in velocity, which can be seen in Figure 3.6a. The velocity shows a near-linear decrease from 0.135 m/ns to 0.097 m/ns during the experiment and is lower than the water content velocity by 0.002 to 0.010 m/ns.

Depth to the reflecting interface at 0.60 m depth can be estimated from the CMPs as an assessment of picking quality. Initial base of sand depth estimates in Figure 3.6b varied, from 0.653 to 0.734 m (CMP1 and CMP2, respectively). The interface depth was consistently overestimated with values typically 0.05-0.10 m above true depth. CMP3 displayed the most consistent value through experiment with a mean of 0.66 m. Large errors were present, such as in CMP1 at 15 minutes, where estimated depth was 1.15 m, a 92% overestimate, which corresponds to the sharp rise in velocity observed in Figure 3.6a.

3.4.5 Comparison of Bulk Water Content Estimates

Bulk water content estimates from the water content probe data and converted from velocities are shown in Figure 3.7. The bulk water content was estimated using a volume-weighting approach, where the three-dimensional area nearest each probe was divided by the total effective irrigated volume (i.e. 1.35 m^3). The water content measurements were multiplied by the weighting factor and summed to provide an estimate of bulk water content. Estimates from the CMPs tend to be greater than the average water content probe measurements. CMP3, which displays the most consistent water content trend, was about 0.03 vol/vol higher than mean probe measurements during the experiment. Fluctuations in values of water content in Figure 3.7 correspond to large observed discrepancies in RMS velocity and reflector depth (Figure 3.6) and result in unrealistic estimates of water content. The CMP1 and CMP2 estimates, for instance, drop below the residual soil moisture at around 4.5, 8, and 15-17 minutes. The travel time estimated water content shows the best agreement with probe measurements and varies from 0.007 to 0.024 vol/vol (3.4 – 29.4% error).

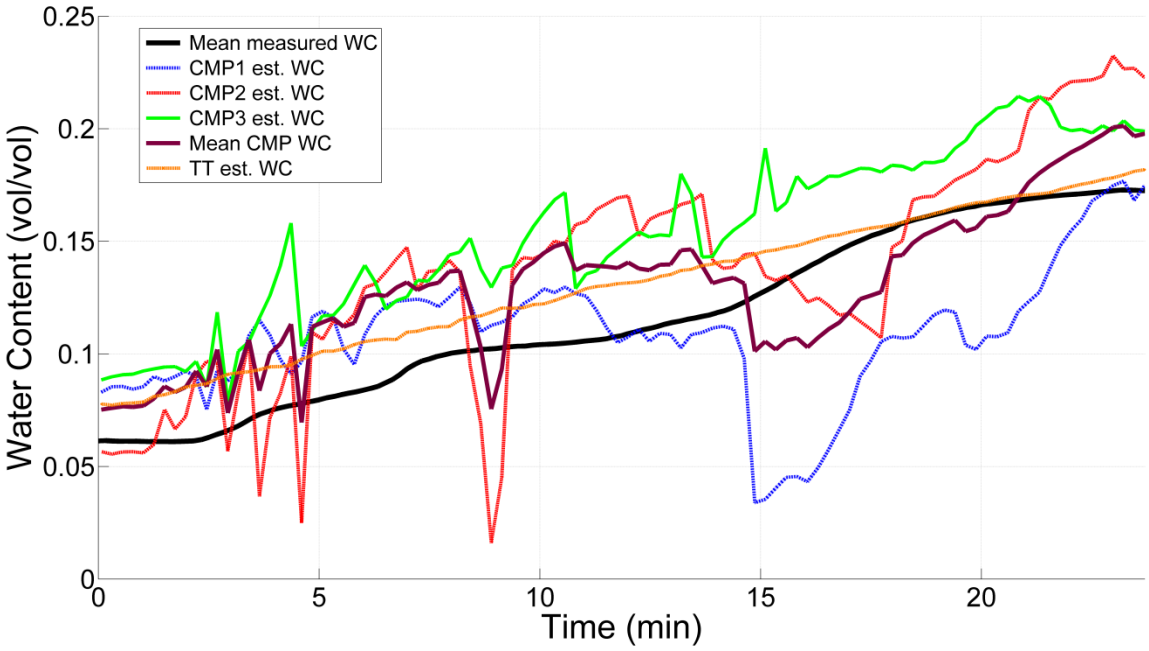

Figure 3.7. Volume-weighted bulk volumetric water content from moisture probes compared to estimated bulk water content from RMS velocities in each CMP, mean RMS velocity converted to water content, and travel time velocity analysis.

3.5 Discussion

The effect of non-uniform flow on multi-offset based velocity estimation is apparent in the analysis. CMP1, collected nearest the wetting front heterogeneity, likely had the most severe deviation from the ideal geometry and uniform lateral velocity assumptions of the Dix equation. This interpretation is suggested by the variability in B arrival travel time in the CMPs and supported by the variable travel times of arrival W in COPs and good agreement with the wetting patterns observed in the water content probes at [1.50 m, 1.60 m]. The wetting front trends in the water content probes indicate more uniformly propagating fronts in the vicinity of CMP2 and CMP3 which accounts for the more stable estimates of velocity from NMO analysis in these locations.

Velocities determined from the reflector picks were influenced by the quality of the reflection in the data. Strong wave interference and low reflection amplitudes created significant difficulty in identification of the wavelet across offset. The benefits of the data collection method used in this chapter are that the short interval between replicate profiles enhances tracking of a particular arrival through the time-lapse data. Additionally, the ability to verify identification of arrivals in multiple dimensions increases the quality of the interpretation. For instance, the trajectory plots shown in Figure 3.5 were particularly important in validating B arrival picks made in CMPs which were low-amplitude or obscured by other arrivals..

When significant heterogeneity in the wetting front is expected, the single-offset velocity estimation methods utilized here may provide better characterization of the apparent velocity and bulk water content. The travel time velocities, when averaged across all positions in the profile, most closely matched the trend and values of the water content probe measurements. Averaging the velocities from CMP's does not produce a velocity estimate which matches the water content probes as well, as Figure 3.7 shows, as the velocity spikes strongly skew the mean. The averaging of multiple measurements in the profiled area likely in the single-offset method smoothed the individual velocity fluctuations of any individual trace. Thus, determination of bulk parameters may be better determined by averaging across the volume using single offset measurements than using a single multi-offset measurement and better suited to describing variability within the volume. The advantage of this methodology is, however, reliant on presence of the sand-gravel interface reflection and the *a priori* knowledge of the interface depth. Reliance of

reflector depth estimates from the CMP data directly may introduce significant error into the single-offset analysis. This method is based on the Dix equation which assumes that offsets are small relative to reflector depth and the system is composed of horizontal layers, and it is acknowledged that these if non-uniform flow is present these assumptions are not met. However, errors in fitting Equation 3.2 may become significant if the wetting front is non-uniform and moveout is irregular. The alternative method enables velocity to be estimated at a much higher spatial density than with sparse multi-offset measurements and may mitigate the impacts of irregular moveout.

3.6 Conclusion

The results and analysis of this experiment demonstrate the influence of non-uniform propagation of a wetting front on estimates of apparent velocity within bulk water content within the layer. Good agreement was found in using the average of single-offset velocity estimates to capture increases in apparent velocity and bulk moisture, with variation from probe measurements reaching 0.013 m/ns (9% error) and 0.024 vol/vol (29.4%) but typically varying by 0.005 m/ns and 0.01 vol/vol. NMO-based velocity estimates were influenced by the deviation of moveout from ideal conditions. A CMP collected where the wetting front advanced more uniformly displayed the decreasing velocity trend apparent in water content probe data, whereas CMPs collected nearer to wetting front heterogeneity showed large fluctuations in velocity estimates and deviate from the decreasing velocity trend. Where continuous reflections within a study area are present, the methodology proposed provides an alternative to multi-offset velocity estimation for estimating the bulk parameters of the flow system while retaining the

ability to capture the spatial variability in transient arrivals and the possibility to interpret non-uniform and preferential flow phenomena directly.

3.7 Works Cited

Allroggen, N., van Schaik, N., Tronicke, J., 2015. 4D ground-penetrating radar during a plot scale dye tracer experiment. Journal of Applied Geophysics, 118: 139-144. DOI:10.1016/j.jappgeo.2015.04.016

Arcone, S.A., Peapples, P.R., Liu, L.B., 2003. Propagation of a ground-penetrating radar (GPR) pulse in a thin-surface waveguide. Geophysics, 68(6): 1922-1933. DOI:10.1190/1.1635046

Becht, A., Appel, E., Dietrich, P., 2006. Analysis of multi-offset GPR data: a case study in a coarse-grained gravel aquifer. Near Surface Geophysics, 4(4): 227-240.

Booth, A.D., Clark, R., Murray, T., 2010. Semblance response to a ground-penetrating radar wavelet and resulting errors in velocity analysis. Near Surface Geophysics, 8(3): 235-246. DOI:10.3997/1873-0604.2010008

Bradford, J.H., 2008. Measuring water content heterogeneity using multifold GPR with reflection tomography. Vadose Zone Journal, 7(1): 184-193. DOI:10.2136/vzj2006.0160

Brosten, T.R. et al., 2009. Multi-offset GPR methods for hyporheic zone investigations. Near Surface Geophysics, 7(4): 247-257.

Buchner, R., Barthel, J., Stauber, J., 1999. The dielectric relaxation of water between 0°C and 35°C. Chemical Physics Letters, 306(1–2): 57-63. DOI:http://dx.doi.org/10.1016/S0009-2614(99)00455-8

Davis, J.L., Annan, A.P., 1989. GROUND-PENETRATING RADAR FOR HIGH-RESOLUTION MAPPING OF SOIL AND ROCK STRATIGRAPHY. Geophysical Prospecting, 37(5): 531-551. DOI:10.1111/j.1365-2478.1989.tb02221.x

Dix, C.H., 1955. Seismic velocities from surface measurements. Geophysics, 20: 68-86.

Ferre, P.A., Rudolph, D.L., Kachanoski, R.G., 1996. Spatial averaging of water content by time domain reflectometry: Implications for twin rod probes with and without dielectric coatings. Water Resources Research, 32(2): 271-279. DOI:10.1029/95wr02576

Garambois, S., Senechal, P., Perroud, H., 2002. On the use of combined geophysical methods to assess water content and water conductivity of near-surface formations. Journal of Hydrology, 259(1-4): 32-48. DOI:10.1016/s0022-1694(01)00588-1

Grote, K., Hubbard, S., Harvey, J., Rubin, Y., 2005. Evaluation of infiltration in layered pavements using surface GPR reflection techniques. Journal of Applied Geophysics, 57(2): 129-153. DOI:10.1016/j.jappgeo.2004.10.002

Grote, K., Hubbard, S.S., Rubin, Y., 2002. GPR monitoring of volumetric water content in soils applied to highway construction and maintenance. The Leading Edge, pp. 482-485.

Haarder, E.B., Looms, M.C., Jensen, K.H., Nielsen, L., 2011. Visualizing Unsaturated Flow Phenomena Using High-Resolution Reflection Ground Penetrating Radar. Vadose Zone Journal, 10(1): 84-97. DOI:10.2136/vzj2009.0188

Hendrickx, J.M.H., Flury, M., Xx, 2001. Uniform and preferential flow mechanisms in the vadose zone. Conceptual Models of Flow and Transport in the Fractured Vadose Zone: 149-187.

Jacob, R.W., Hermance, J.F., 2004. Assessing the precision of GPR velocity and vertical two-way travel time estimates. Journal of Environmental and Engineering Geophysics, 9(3): 143-153.

Lunt, I.A., Hubbard, S.S., Rubin, Y., 2005. Soil moisture content estimation using ground-penetrating radar reflection data. Journal of Hydrology, 307(1-4): 254-269. DOI:10.1016/j.hydrol.2004.10.014

Mangel, A.R., Lytle, B.A., Moysey, S.M.J., 2015. Automated high-resolution GPR data collection for monitoring dynamic hydrologic processes in two and three dimensions. The Leading Edge, 34(2): 190-196. DOI:http://dx.doi.org/10.1190/tle34020190.1

Mangel, A.R., Moysey, S.M.J., Ryan, J.C., Tarbutton, J.A., 2012. Multi-offset ground-penetrating radar imaging of a lab-scale infiltration test. Hydrology and Earth System Sciences, 16(11): 4009-4022. DOI:10.5194/hess-16-4009-2012

Mount, G.J., Comas, X., Cunningham, K.J., 2014. Characterization of the porosity distribution in the upper part of the karst Biscayne aquifer using common offset ground penetrating radar, Everglades National Park, Florida. Journal of Hydrology, 515: 223-236. DOI:10.1016/j.jhydrol.2014.04.048

Steelman, C.M., Endres, A.L., 2012. Assessing vertical soil moisture dynamics using multi-frequency GPR common-midpoint soundings. Journal of Hydrology, 436: 51-66. DOI:10.1016/j.jhydrol.2012.02.041

Steelman, C.M., Endres, A.L., Jones, J.P., 2012. High-resolution ground-penetrating radar monitoring of soil moisture dynamics: Field results, interpretation, and comparison with unsaturated flow model. Water Resources Research, 48: 17. DOI:10.1029/2011wr011414

Stoffregen, H., Yaramanci, U., Zenker, T., Wessolek, G., 2002. Accuracy of soil water content measurements using ground penetrating radar: Comparison of ground penetrating radar and lysimeter data. Journal of Hydrology, 267: 201-206.

Topp, G.C., Davis, J.L., Annan, A.P., 1980. Electromagnetic Determination of Soil-Water Content - Measurements in Coaxial Transmission Lines. Water Resources Research, 16(3): 574-582. DOI:10.1029/WR016i003p00574

Truss, S., Grasmueck, M., Vega, S., Viggiano, D.A., 2007. Imaging rainfall drainage within the Miami oolitic limestone using high-resolution time-lapse ground-penetrating radar. Water Resources Research, 43(3): 15. DOI:10.1029/2005wr004395

Turesson, A., 2006. Water content and porosity estimated from ground-penetrating radar and resistivity. Journal of Applied Geophysics, 58(2): 99-111. DOI:10.1016/j.jappgeo.2005.04.004

Yilmaz, O., 2001. Seismic Data Analysis: Processing, Inversion, and Interpretation of Seismic Data. Society of Exploration Geophysicists, Tulsa, OK, 2065 pp.

CHAPTER 4
ASSESSMENT OF TRAVEL-TIME VELOCITY ANALYSIS METHODS FOR RESOLVING NON-UNIFORM FLOW PHENOMENA WITH GROUND PENETRATING RADAR

4.1 Abstract

Migration processing techniques can improve the resolution of ground penetrating radar (GPR) profiles by relocating scattered energy to its true position in the subsurface (Yilmaz, 1987). This chapter examines the use of 2D migration techniques on simulated data from forward modeling of a numerical flow simulation and empirical time-lapse GPR data from a lab-scale experiment using a vadose zone analog and collected during non-uniform infiltration events. The ability of the migrated images to capture dynamic flow processes is evaluated, such as tracking changes in wetting front depth over time, and the potential for resolving non-uniform flow features in 2D is examined. The travel-time velocity analysis methods developed in Chapter 3 are used to determine the wave velocity structure for both cases, and the time-domain GPR profiles are depth migrated using the 2D velocity models, resulting in images of infiltrating water with respect to depth. These 2D profiles are compared with the numerical flow simulation and *in situ* water content probes to assess the resulting accuracy. A reasonably good agreement is found in both cases, with the simulated images producing results similar to an "ideal" case and much improvement over migrating with a constant velocity. The empirical GPR images show wetting front movement at rates close to those observed in water content probes.

4.2 Introduction

Preferential flow is defined as “all phenomena where water and solute move along certain pathways, while bypassing a fraction of the porous matrix,” and a major cause of preferential flow is heterogeneities in the pore structure, such as macropores or material boundaries (Hendrickx et al., 2001). Flow instabilities resulting in fingered flow can also contribute to preferential flow in media which are essentially homogenous above the pore scale. The rapid transport of water and solutes due to preferential flow is of concern in many areas relating to groundwater quality and quantity and contaminant flow and transport. Geophysical sensing methods, such as surface-based ground penetrating radar (GPR) offer a means of non-invasively capturing spatially continuous data, unlike *in situ* hydrologic instruments, and have been applied to the problem of monitoring unsaturated flow in the vadose zone (Binley et al., 2001; Cassiani and Binley, 2005; Looms et al., 2008; Steelman and Endres, 2012; Steelman et al., 2012). In particular, time lapse measurements using GPR have been utilized for identifying the mechanisms of non-uniform and preferential flow in the unsaturated zone (Allroggen et al., 2015; Haarder et al., 2011; Truss et al., 2007).

Preferential flow occurred in all the time lapse studies, though the success in directly imaging preferential flow phenomena with GPR varied. Truss, et al., (2007) tracked infiltrating bulbs of into limestone with known dissolution features. 2D profiles were collected every 3 during over two natural infiltration events for 70 minutes, and a full 3D profile was collected hourly during a forced infiltration experiment lasting four hours. From these data, the authors inferred preferential flow based variable changes in the

travel time to static reflectors prior to and following infiltration and on the presence of diffraction hyperbolas within the GPR data. This interpretation was verified by excavation of the areas profiled with GPR which contained rubble and tree roots, and finger-sized dissolution features forcing flow along preferential pathways. In contrast, Allroggen et al., (2015) and Haarder et al., (2011), performed dye-staining infiltration experiments in which the excavated soil profiles contained numerous preferential flow features. The GPR data did not contain any direct evidence of preferential flow as it occurred (e.g. diffraction hyperbolas) but the patterns in travel-time shifts due to velocity decreases from increases in water content were used to infer the movement of water and verified by patterns of dye-staining in the soil.

The circumstances under which preferential flow features can be directly resolved using GPR remains to be answered. The resolution of GPR images is limited by the signal frequency, and therefore individual flow features (e.g. macropores) may lie beyond the resolving power, though other non-uniform flow features such as unstable wetting fronts may be captured with GPR and contain valuable insights into flow dynamics (Jol, 2009). When flow is strongly non-uniform it is likely that GPR profiles will become complicated by interfering arrivals and strong vertical and lateral contrasts in wave velocity will distort reflections in the time domain and make direct interpretation difficult.

Migration processing, which improves the resolution of the images by moving reflected energy from its apparent location to the true location of the reflecting interface, may improve the interpretability of time-lapse images of infiltration (Yilmaz, 2001).

Examples in the literature of migrating GPR data often focus on improving images for stratigraphic interpretation (Fisher et al., 1992b; Gomez-Ortiz et al., 2006; Neal and Roberts, 2001) or characterization of static systems (Bradford, 2008; Bradford and Harper, 2005). A model of the wave velocity in the profiled area is required to perform migration. In the time-lapse studies, wave velocities for migration have been assumed constant across the profiled area and obtained from analysis of diffractions (Truss et al., 2007), from borehole tests (Haarder et al., 2011), or from multi-offset GPR estimates (Allroggen et al., 2015). The effect of variability in the velocity structure during non-uniform flow events on the accuracy and interpretability of the final migrated image has not been investigated

The objective of this chapter is to examine the use of migration techniques on time-lapse GPR data collected during infiltration events to quantitatively describe changes in the flow system, such as wetting front depth, and evaluate the potential for resolving non-uniform flow features in migrated GPR data. The travel-time velocity analysis methods developed in Chapter 3 are used to determine the 2D wave velocity structure for both synthetic GPR data obtained from forward modelling of a numerical flow simulation and experimental GPR data collected during infiltration into a vadose zone analog. The time-domain GPR profiles are depth migrated using the 2D velocity models, resulting in images of infiltrating water with respect to depth.

4.2.1 Migration Methods for Image Enhancement

GPR images of the subsurface from reflection profiles are visualizations of energy recorded at the surface. Due to irregularities in reflecting surfaces, the presence of

scattering objects, and other structural features, the energy recorded at the surface does not strictly come from directly underneath the receiver. The result is that GPR images will often have arrivals which obscure features of interest and decrease the resolution of the image, such as diffraction hyperbolas. Migration is a process which relocates recorded energy in time or space to its true position and improves the image resolution by collapsing diffraction hyperbolas and moving dipping reflections to their proper location (Yilmaz, 1987). This is a standard practice in the seismic exploration industry, where complex geological structures with strong velocity contrasts (e.g. salt bodies) often distort images severely, and many of the migration techniques have been applied to GPR data. The conditions required to migrate GPR data are that the wave propagation kinematics are described by principles of geometrical optics and that wave propagation is non-dispersive (Fisher et al., 1992b).

The improper placement of reflections originates when traces are plotted in their relative positions which contain reflected events not originating from directly beneath the source-receiver pair. For example, the permittivity model in Figure 4.1a contains an inclined interface separating low- and high-permittivity layers from 5-8 m depth and two high-permittivity anomalies at 2-3 m depth. Simulated GPR measurements, plotted as a constant-offset profile with amplitudes plotted relative to their lateral position and two-way travel time, show the characteristic diffraction hyperbolas created by objects below the resolving power of the emitted wave. The depth migrated profile in Figure 4.1c shows the collapse of the diffraction hyperbolas to their proper depth and lateral position.

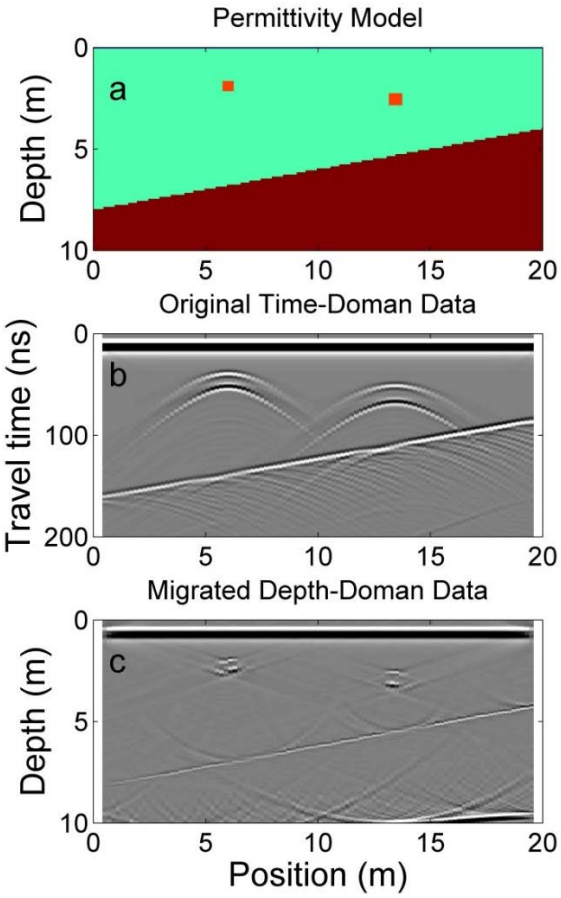

Figure 4.1. Migration example: (a) A permittivity model of the subsurface showing two contrasting layers, the shallower layer having embedded anomalies with contrasting permittivity, (b) the resulting constant offset profile, and (c) a depth migrated profile.

Many migration processing algorithms convert the data from the time-domain to the depth-domain. Time-domain data, as the COP in Figure 4.1b, plot recorded amplitudes relative to their ground position and the travel time of the emitted wave. Depth-domain profiles, such as Figure 4.1c show the recorded amplitudes relative to their true depth. In this chapter the split-step algorithm of Stoffa, et al. (1990) as implemented in Seismic Un*x is used to migrate both simulated and empirical GPR images from the time-domain to the depth-domain. This method is an enhancement of frequency-wavenumber (*f*-k)

migration which accounts for lateral velocity variation (Stoffa et al., 1990) and has been demonstrated as an applicable method for GPR (Fisher et al., 1992a).

4.3 Methods

Numerical and empirical (lab-based) experiments were conducted to evaluate the potential of migration to improve the interpretation of time-lapse GPR data collected during an infiltration event. In both cases, the infiltration was non-uniform as the irrigation source covered only a portion of the soil surface and, in the experimental case, the flow was non-uniform. The numerical tests provide a baseline for evaluating the value of migration under ideal conditions, whereas the empirical study provides insights relevant to a realistic field scenario.

4.3.1 Numerical Experiment

Simulations consist of an unsaturated (Richard's equation) flow model in HYDRUS 2D (Simunek et al., 1999) coupled to a 2D finite-difference time-domain code implemented in MATLAB (Irving and Knight, 2006). The flow model domain, shown in Figure 4.2, is 4.0 m x 0.6 m [width x height]. A finite-element mesh is generated using a targeted element size of 0.04 m. The sides and portions of the top boundary are specified as no-flow boundaries.

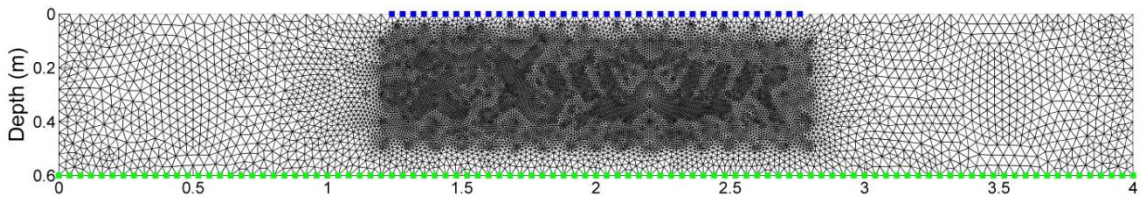

Figure 4.2. Finite-element mesh used in HYDRUS-2D simulation. Nodes shown in blue are constant-flux and in green are seepage face boundaries.

Drains in the tank are simulated using seepage face boundary nodes along the bottom of the model in which water leaves the model domain from the node upon reaching saturation (i.e. the pressure head is zero along the seepage face). Constant flux nodes are assigned to the top boundary from 1.24 to 2.76 m position, corresponding to the irrigated portion of the sand tank and with the effective flux rate from lab experiments of 0.0036 m/min. Flow is simulated for 22 minutes, which is approximately equal to a period of irrigation used in the lab experiment. The mesh is refined in the interior of the domain with element sizes of 0.01 m.

Hydrologic parameters for the sand were taken from laboratory tests as reported in Mangel et al., (2012), and are contained in Table 4.1. A random, normally-distributed saturated hydraulic conductivity field is used in the model using the mean and standard deviation from lab tests to incorporate slight variability in the flow system. Initial pressure heads within the sand are set equal to the height above the seepage face boundary, thus initial water content along the soil profile vary from the residual and saturated values (0.06 to 0.38 vol/vol, respectively) from top to bottom.

Table 4.1. Hydraulic parameters used in HYDRUS-2D flow simulation.

Residual water content Θ_r (vol/vol)	Saturated water content Θ_s (vol/vol)	Saturated hydraulic conductivity K_S (cm/min)	Standard deviation of K_S (cm/min)	Air-entry parameter α (1/cm)	Shape parameter n
0.06	0.38	4.6	0.33	0.058	4.09

The water content distributions output from HYDRUS-2D are interpolated to a regular grid of 0.01 m cells to form the GPR model domain. Additions to the model domain allow for interaction of GPR waves with the tank boundaries and consist of a 0.20 m thick region added to the top and sides to simulate air and a region 0.30 m thick added to the bottom to simulate the gravel underlying the sand within the tank. Beyond these regions absorbing perfectly matched layer (PML) boundary conditions are used to remove the effect of reflections from the edge of the simulated domain (Irving and Knight, 2006). Dielectric permittivity values of 1 and 4.5 are used in the air and gravel regions, respectively, and held constant. The water content values output from HYDRUS-2D are converted to dielectric permittivity using Ferre's approximation of the Topp equation (Ferre et al., 1996). As this model is focused on wave kinematics and not on preserving exact amplitude information, electrical conductivity and magnetic permeability are assumed constant. Conductivity was set to 0 mS/m in air and 1 mS/m in sand and gravel, and the magnetic permeability of free space (1.256×10^{-6} H/m) is assigned at all locations.

4.3.2 Empirical Experiment

A forced infiltration experiment was conducted in a wooden tank measuring 4 m x 4 m and filled with 0.60 m of homogenous river sand (Figure 4.3). The tank is equipped with a drainage system consisting of 16 – 1 m x 1 m cells which drain independently to the exterior of the tank, and an impermeable liner separates the sand from a gravel-filled zone used to support the drains. Irrigation for the experiments was applied using two 1.5 m-long sprayer arrays consisting of micro-sprayers mounted to PVC pipes. The micro

sprayers collectively irrigate a central area measuring approximately 2.25 m^2. The volumetric flux applied to the sand surface was controlled at 8 liters/min, or an effective flux of 3.56 mm/min across the irrigated area.

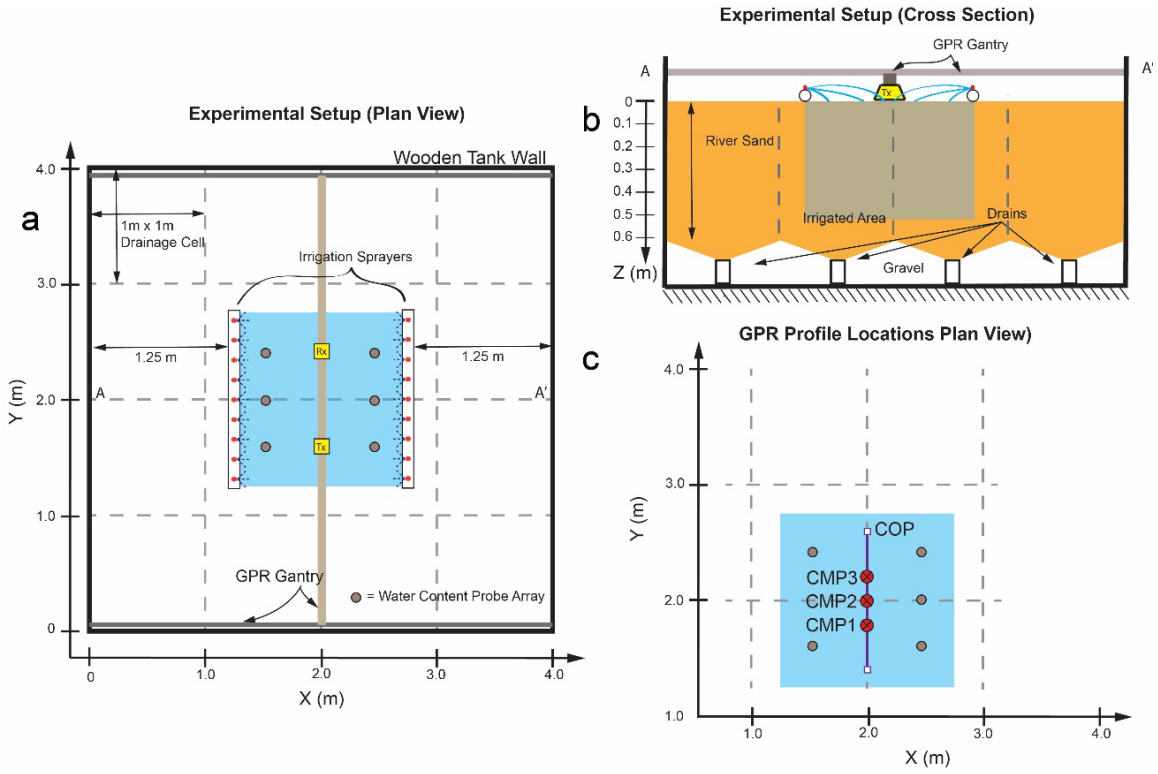

Figure 4.3. Experimental setup. a) Plan view of the tank showing positions of the irrigation sprayers, drainage bays (DB1-DB4), automated GPR gantry, and six vertical arrays of water content probes at various depths in the sand (A1-B3). b) Cross-section through the tank center. c) Detail of the irrigated area and positions of GPR profiles collected during the experiment.

Time-lapse GPR data were continuously collected within the irrigated area as a cycle of three common midpoint (CMP) surveys followed by one constant offset profile (COP) using an automated gantry system to automatically position the antennas as shown in Figure 4.3c and described in Table 4.2. Offsets for the CMPs varied from 0.16 to 1.00

m, and the COP offset was 0.16 m. Traces were collected every 0.01 m. The four-profile cycle was repeated 100 times over approximately 23 minutes, with 14-15 seconds elapsing per cycle and 142,695 traces collected in total.

Table 4.2. Locations of profiles collected during the infiltration experiment.

Initial X-Y position (m)	Final X-Y Position (m)	Offset (m)
[2.00, 1.75]	[2.00, 1.75]	0.16 – 1.00
[2.00, 2.00]	[2.00, 2.00]	0.16 – 1.00
[2.00, 2.25]	[2.00, 2.25]	0.16 – 1.00
[2.00, 1.50]	[2.00, 2.50]	0.16

A detailed description of the automated gantry system can be found in Mangel et al., 2015. These experiments were performed with an updated version of the gantry system utilizing a fiberglass central rail, rather than aluminum, to minimize interference. Sensors and Software 1000 MHz shielded antennas were used to obtain the highest-resolution data possible. A time sampling window of 25 ns was used along with 4 stacks per trace. Prior to irrigation, the sand surface was raked flat to ensure good coupling of the radar antennas with the ground. Irrigation began one minute after the start of GPR data collection and terminated after 23 minutes.

4.3.3 GPR Analysis

The synthetic GPR data simulated in the numerical experiment and real GPR data observed in the empirical experiment are analyzed in the same way. Processing steps include a time-zero correction applied to all GPR data. The reflection data are analyzed using the single-offset travel-time method of velocity analysis as described in Chapter 3.2.3 to create a vertical distribution of wave velocity for each position in the GPR

profiles for both the numerical and experimental data sets which are subsequently smoothed in 2D to remove sharp velocity contrasts. Picks of the base of sand and wetting front reflections were made using a semi-automated cross correlation method in which initial automated picks are made from profiles of replicate traces at each location plotted with respect to experimental time, here termed trajectory images, and manually adjusted. The arrivals of interest had fairly low amplitude in many traces from the experimental GPR profiles, and diffractors at early travel times also obscure the wetting front arrival making the wetting front particularly difficult to pick. Thus, the profiles are initially time migrated in Seismic Un*x, using a constant velocity determined iteratively to produce the most visually coherent wetting front arrivals. The time-migrated profiles are then used for picking and velocity model creation. The GPR data are then depth migrated using the split-step algorithm of Stoffa, et al. (1990) as implemented in Seismic Un*x..

4.4 Results

4.4.1 Numerical Simulations

The simulated data are shown in Figure 4.4, with the flow models contained in Figure 4.4a-d and the common offset GPR profiles in Figure 4.4e-h. The initial water content conditions in the sand are laterally uniform. (Figure 4.4a). The infiltrating bulb of water propagates with an apparent velocity of 0.02 m/min determined by tracking between subsequent time steps, and the bulb extends laterally 0.15 m beyond the applied flux zone (represented by the solid black line in Figure 4.4b-d). As the wetted bulb propagates beyond 0.40 m depth, it interacts with the capillary fringe causing the contrast

in water content to decrease until the wetting front is no longer distinguished (not shown).

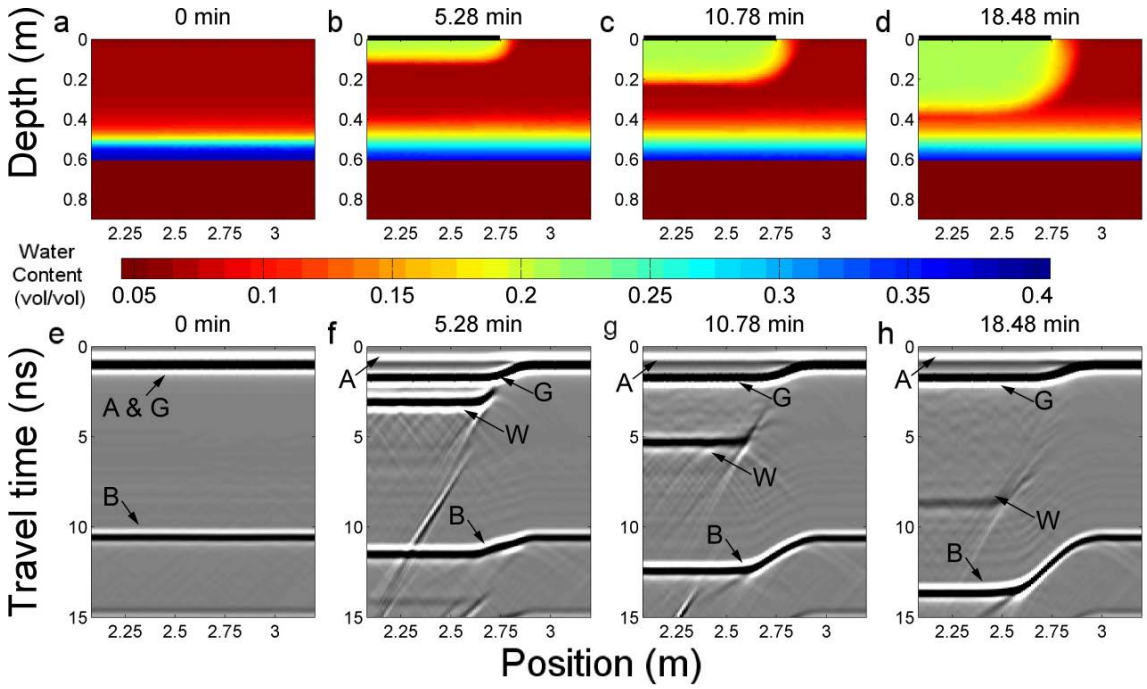

Figure 4.4. Unsaturated flow simulation for representative times (a-d) and corresponding GPR forward model constant offset profiles (e-h). Thick black line across (c-d) indicates irrigated zone.

In the corresponding GPR profiles, prior to infiltration (Figure 4.4e) the air and ground wave arrivals overlap between 0-1.5 ns and the reflections from the base of sand and base of gravel arrive at 10 and 15 ns, respectively. As infiltration commences, the wetted zone of soil expands downward and outward in a bulb and the arrivals from the air wave (labeled A, visible from 0-0.6 ns) can be distinguished from the ground wave (labeled G, visible from 1-2.4 ns) within the wetted zone (i.e., lateral positions less than 2.75 m) due to the decrease in GPR velocity caused by higher water contents in this region (Figure 4.4f). A reflection from the bottom of the wetted bulb is also visible

during the infiltration event; this arrival increases in travel time and weakens in amplitude as the wetting front propagates downward (labeled W in Figures 4.4f-h). A diffraction artifact associated with scattering from the edge of the wetted zone is apparent at the edge of this reflection. The reflection from the base of the sand (labeled B) does not change over the course of the irrigation event in the dry region of the domain, but arrival times increase in the irrigated area due do a decrease in average velocity above the reflector. There is a transition zone between the wet and dry regions, where the bottom of tank reflection appears to be inclined, though this is an artifact resulting from the velocity contrast in this area.

The velocity models used to produce the reflection images in Figure 4.4 (i.e., the models derived from the HYDRUS simulation) are used as inputs to the migration to evaluate the best possible image improvement and highlight potential limitations. Figures 4.5a-d show these "true" velocity models and Figures 4.5e-h show the corresponding GPR profiles obtained using Stoffa's (1990) split-step migration algorithm. The base of sand arrival is perfectly located at its true depth of 0.60 m in the initial profile (Figure 4.5e). The migrated images obtained after the initiation of irrigation, however, contain arc-shaped artifacts (i.e., "smiles") originating from the bottom of sand reflection near the edge of the wetted zone (c.f. Figure 4.4e which has no such arrival). These artifacts are the result of the sharp lateral velocity contrast at the edge of the wetted zone.

The wetting front arrival in the simulated GPR profiles are generally consistent with the width, shape, and depth of the low velocity bulb from the input models, which is represented by a blue line in Figure4.5f-h. Errors in depth of the migrated arrival are

generally around 0.01 m. The presence of migration artifacts complicates the image, but these do not severely limit the interpretability of the profiles. While the migration algorithm does not account for direct arrivals (i.e., the air and ground wave), they were not removed from the data prior to migration as the wetting front reflection could not be discriminated from these arrivals at early time. As a result, there is a consistent artifact at the top of the image associated with the air and groundwave migration that was produced by the velocity contrast in the air above the ground surface and the wetted zone. This shift in the direct arrivals is not meaningful.

The ideal migration case (i.e., using the velocity models derived from the flow simulation) results in high-quality migrated images. The overall geometry and position of reflectors in the profiles are true to the input models with small errors in position and depth. Although the strong lateral velocity contrast results in poor imaging of the edge of the low-velocity zone, it's size, shape, and location are accurate to the input models . The presence of artifacts does not significantly reduce the interpretability of the profiles.

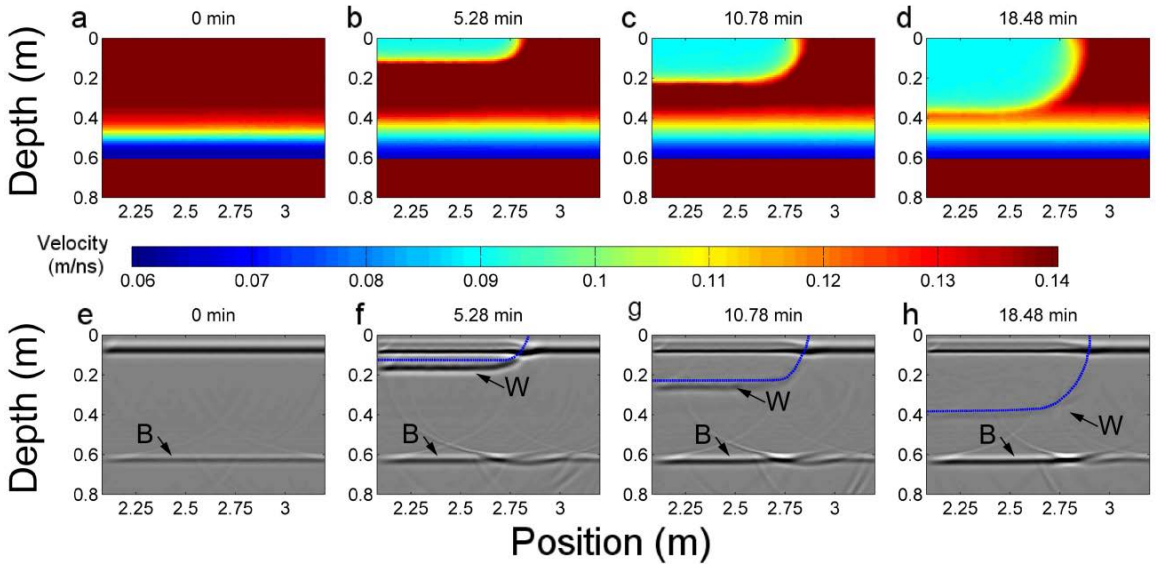

Figure 4.5. HYDRUS flow simulation output converted to velocity (a-d) and corresponding depth migrated profiles (e-h) which represent the optimal outcome of the migration.

Constant RMS velocity profiles for each time step are used to migrate the GPR profiles for a comparative dataset to identify the benefits and shortcomings originating from migration with a heterogeneous velocity structure. Figure 4.6a-d show GPR profiles obtained by migrating using the mean RMS velocity within the profiled area determined from the travel time velocity analysis. As before, the air and ground wave arrivals are not muted prior to migration and exist as an artifact across the top of Figures 4.6e-h. The base of sand arrival erroneously shows increasing travel time as the extent of the low-velocity zone increases. Prior to irrigation, the arrival is continuous across the profile at 0.64 m. Upon wetting, the arrival increases in depth within and beyond the area receiving irrigation (i.e., at positions up to 3 m). At 18.48 minutes, the base of sand arrival has a maximum depth of 0.71 and a pronounced incline to shallower depths beyond the irrigated area.

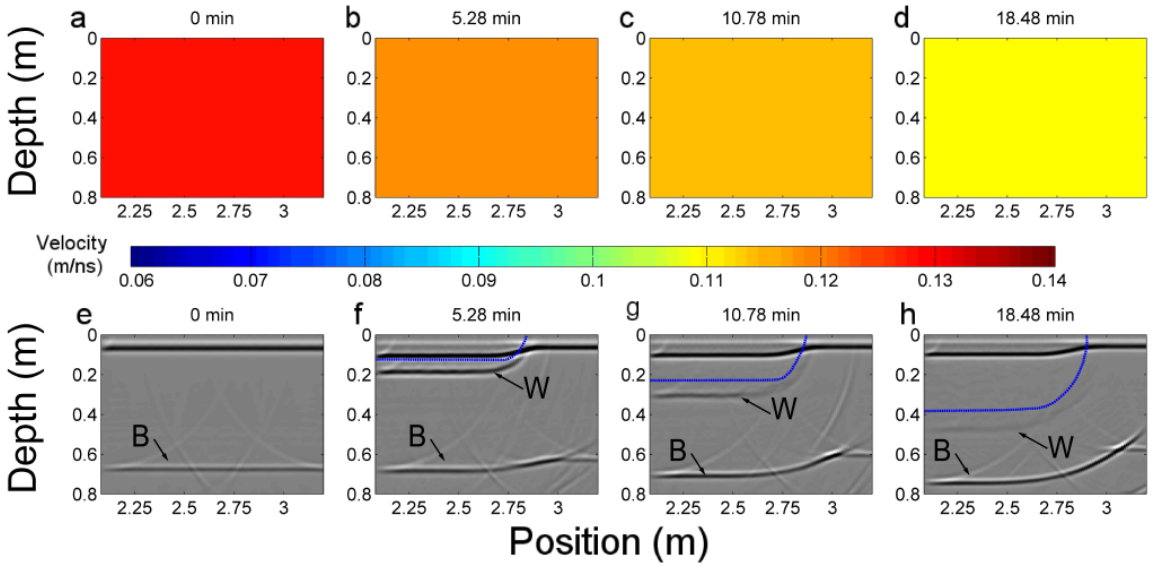

Figure 4.6. Constant RMS velocity models (a-d) and corresponding depth migrated profiles (e-h) with the true wetting front depth from flow simulation plotted as blue line.

The shape of the wetting front arrival is consistent with the previous migrated GPR profiles and input models but has significant errors in depth. The errors in depth of this arrival decrease over time as the contrast between the low velocity behind the wetting front and the mean RMS velocity declines. The first arrival energy in the irrigated area at 5.28 minutes is located at 0.15 m depth (50% overestimate compared to the model depth), at 0.28 m at 10.78 minutes (27% overestimate) and 0.44 m at 18.48 minutes (13% overestimate). In Figure 4.6h, the wetting front arrival is located at 2.95 m position which is beyond the width of the low-velocity zone in the input model in Figure 4.6d and the wetting front arrival in “ideal” migrated image in Figure 4.6h.

Not accounting for the low velocity zone results in poor accuracy of the reflector locations in the migrated images. The base of sand arrival is most accurate at early times

and becomes increasingly distorted as a result of the static velocity. Interpretation of the migrated images would erroneously suggest that the base of sand surface was changing depth over time. The wetting front arrival more closely matches the model input at later times when the contrast between the mean RMS velocity and the low-velocity zone decreases. These images demonstrate that the large heterogeneity in velocity structure needs to be accounted for the migration operation to produce good results.

The quality of the velocity models created from travel time analysis and subsequent migrated GPR profiles can be evaluated using the "ideal" velocity case and constant RMS velocity case as a baseline. The velocity models created from travel time analysis of the wetting front and base of sand reflections are shown in Figure 4.7a-d. The initial RMS velocity is used for all locations and thus the vertical velocity gradient seen in Figure 4.7a is not represented in the velocity model. Following irrigation, the low-velocity zone in Figure 4.7b is very consistent in size and depth to the input velocity model except at the edge of the irrigated zone. The low-velocity zone has velocities around 0.06 to 0.07 m/ns, which are lower than the true velocity of 0.09 m/ns (Figure 4.7b). The velocity analysis does not capture the decreased velocity above the sand-gravel interface from 0.4 to 0.6 m depth resulting in underestimation of the velocity behind the wetting front. As irrigation continues (Figures 4.7 c,d), the shape of the low-velocity zone becomes irregular, particularly at positions greater than 2.5 m. The low-velocity zone thickness slightly underestimates the true thickness in the model at positions lower than 2.5 m, and significant discrepancies (0.05 to 0.10 m) in thickness exist between 2.5 m position and the edge of the low-velocity zone.

The migrated GPR profiles are shown in Figure 4.7e-h. These images are comparable in quality to the images produced by migrating with the "true" velocity model, albeit with errors in the position of reflectors, and are a significant improvement in accuracy over images created by migrating with a constant velocity. Initially, the depth to the base of the sand layer in the migrated profile is overestimated by 5%, i.e. at 0.63 m depth versus the true depth of 0.60 m (Figure 4.7e). After irrigation begins, the base of sand reflection contains an abrupt shift in depth at 2.67 m position and additional "smiles" are now present which were not observed in the "ideal" migration case. During irrigation, the arrival is consistently within 0.03 m of the true depth despite irregularity in shape. The arrival remains laterally continuous until about 18 minutes into irrigation (Figure 4.7h) where irregularities in the shape of the low-velocity zone cause a pronounced discontinuity in the arrival.

The shape of the wetting front arrival shows good agreement with the "ideal" migrated images and reasonably good agreement to the input model. The arrival is laterally continuous in all the images, though spurious shifts in the depth of the arrival are apparent in Figures 4.7g-h due to the irregularities in the low-velocity zone. The first arrival energy is shallower than the true wetting front depth in all cases, though errors decrease with time. At 5.28 minutes, the migrated wetting front arrival at a depth of 0.08 m, 33% shallower than the true depth of 0.12 m in the flow model (Figure 4.7b) and in the "ideal" migration case (Figure 4.5h). In Figures 4.7g-h, the wetting front is located at 0.15 m depth (33% error) and 0.32 m depth (15% error).

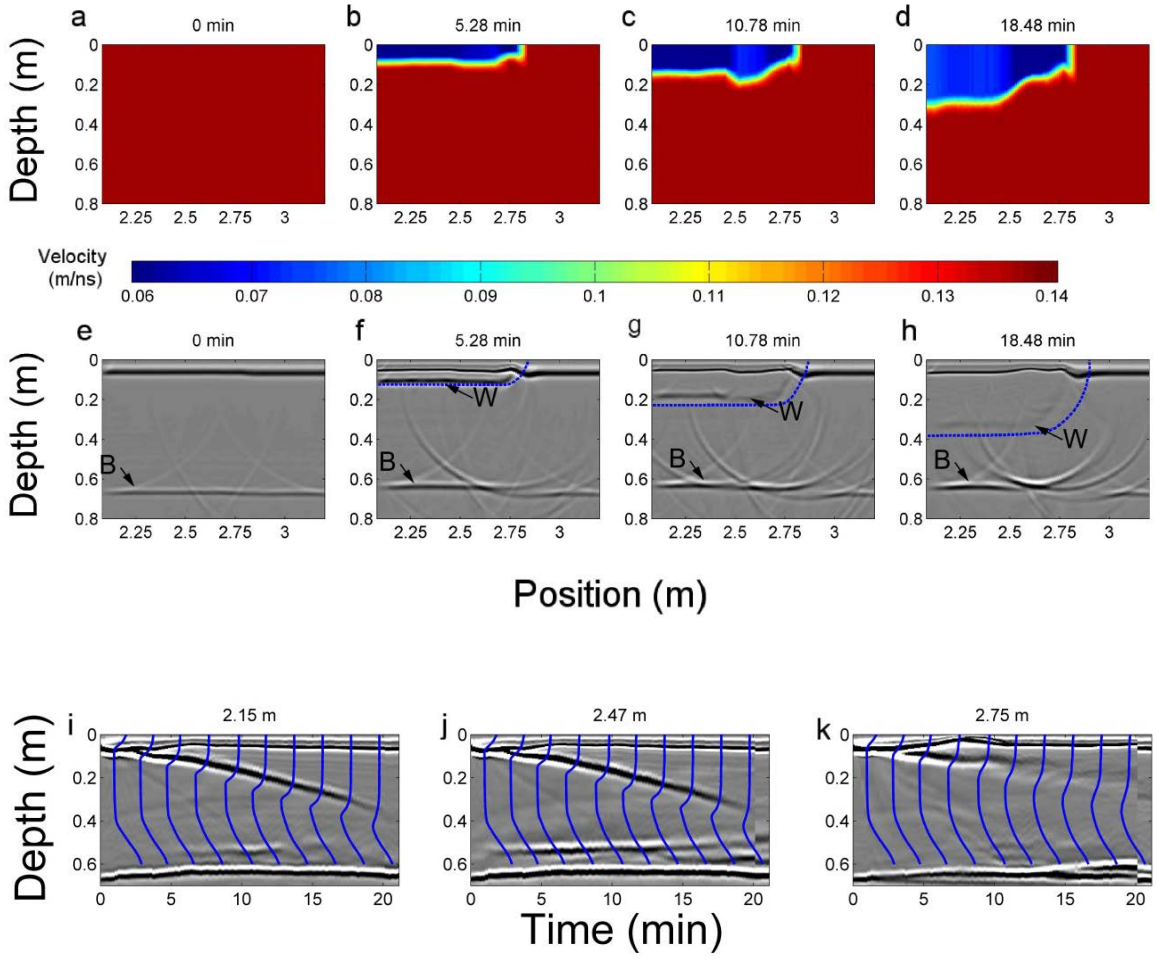

Figure 4.7. Velocity models created by tracking wetting front arrival travel times (a-d) and corresponding depth migrated profiles (e-h). Migrated synthetic trajectory images at (i) 2.15 m (j) 2.47 m and (c) 2.75 m positions, each with the hydrologic model output superimposed on the corresponding time.

The migrated trajectory images (Figure 4.7i-k) provide an additional comparison of the water content profiles from the flow model and the migrated position of the wetting front arrival. The first break of the wetting front arrival (Figure 4.7i, j) corresponds with the first increase in water content (i.e., the wetting front) in the flow simulation. The trajectory plot for 2.75 m (Figure 4.7k) displays the poorer focusing of energy within the

corner of the infiltrating bulb than at lower positions and discontinuities in the visible wetting front arrival (e.g. 11.2, 12.5, 14.8 minutes) yet, when compared to the flow model, still captures the wetting front propagation well, especially up to 14 min, after which errors of about 0.10 m in depth are visible.

Despite the irregularities in the shape and magnitude of the low-velocity zone, the analysis resulted in velocity models and migrated images which can be used to track the propagating wetting front with reasonable accuracy. During the simulation, errors in depth were from 0.03 to 0.06 m in the lateral portion of the wetting front (15% to 33% error), but the wetting front propagation velocity in the migrated profiles is 0.018 m/min, very close to the actual value of 0.02 m/min observed in the flow simulation. The mean wetting front velocity derived from the time-lapse velocity models (Figure 4.7a-d) is 0.01 m/min and varies from 0.005-0.04 m/min. The velocity models and migrated GPR images show similar temporal changes to the underlying flow system.

4.4.2 Experimental Results

The empirical time-domain GPR data are shown in Figures 4.8a-g and their complexity implies a more complicated flow system than the simulations above. The direct ground wave (G) constitutes the first significant arrival at 1.5 ns. The sub-horizontal base of sand arrival B is present across the profile at 10 ns travel time and other moderately continuous reflectors are present within the sand, including a reflection labeled M from the base of the gravel layer below the sand within the tank. The wetting front reflection W is not easily distinguished from other arrivals until 8-10 minutes into the experiment (Figure 4.8c) at about 6 ns travel time. W and B increase in travel time

during the experiment and with increasing discontinuity over time. The portion of the wetting front arrival from 1.50 m – 1.65 m position increases travel-time ahead of the rest of the front (Figure 4.8d,e), and by 23.8 minutes W is no longer distinguishable from B at 16 ns near the left margin of the profile in Figure 4.8f while W and B are separated by 1-4 ns at other locations. This separation is distinct in the trajectory plots in Figures 4.8j-i. The non-uniform increases in travel-time of arrivals from the base of sand and the wetting front are interpreted as evidence of non-uniform wetting across the profiled area, which is consistent with variations in the flow behavior inferred from the water content probe data and drainage from the tank. The general continuity of the wetting front reflection across the profiles and lack of individual diffraction features suggest that the wetting front was locally continuous and discrete flow features were not present within the profiled area, though the potential exists as results presented in Chapter 2 demonstrate.

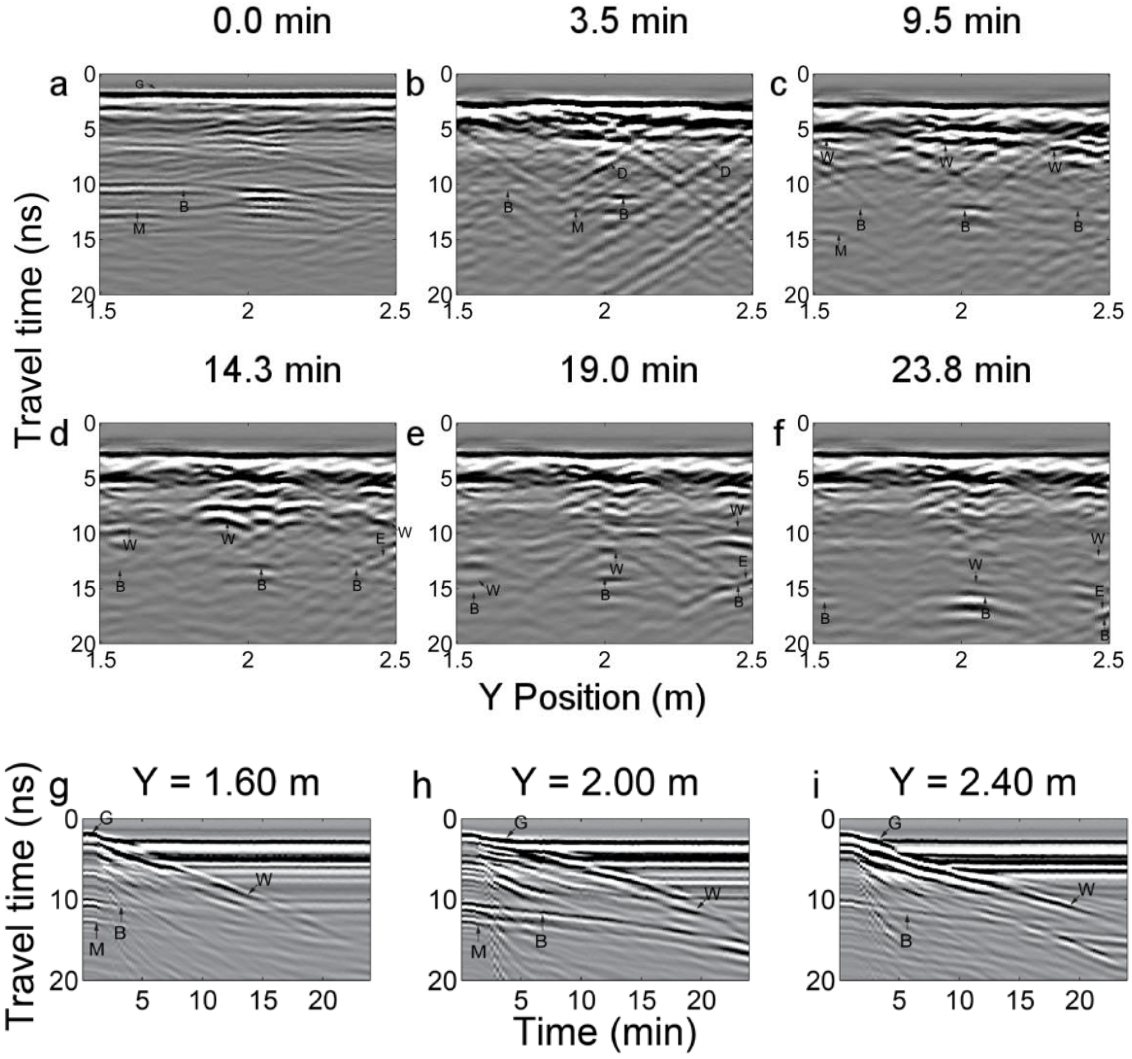

Figure 4.8. The COP-Y constant offset profiles collected (a) prior to and (b-f) during irrigation and the trajectory plots (g-i) at the locations of water content probe arrays.

Analysis of the GPR data results in the 2D velocity models shown in Figure 4.9a-d in which a low-velocity zone increasing in thickness is observed which corresponds to movement of the wetting front through the sand. Velocities within this zone are generally from 0.08 to 0.11 m/ns, corresponding to a water content of approximately 0.14 to 0.26 vol/vol. The interface between high and low velocities increases with depth at a generally

uniform rate from 0 to 10.5 minutes (Figure 4.9a, b), after which the interface dips toward the left in the images, which is consistent with patterns of arrivals in the reflection profiles.

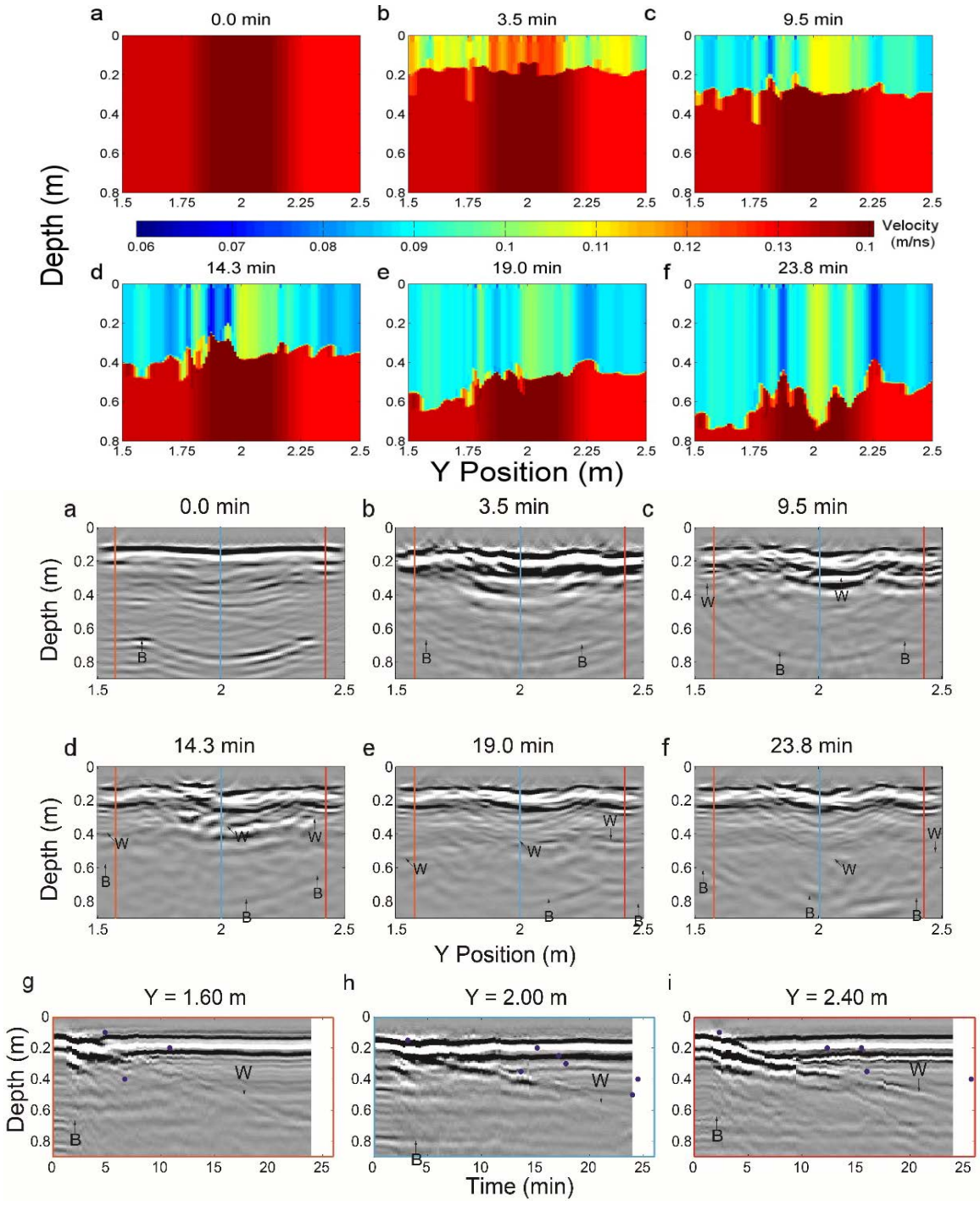

Figure 4.9. a-f) Velocity models created from travel time analysis of GPR data collected during infiltration, migrated GPR images at e) Y = 1.60 m f) Y = 2.00 m and g) Y = 2.40 m. Plotted points show the time at which the wetting front passed probes adjacent to the GPR line.

The migrated GPR profiles are shown in Figure 4.9a-f and trajectory images at Y positions of 1.60 m, 2.00 m, and 2.40 m, corresponding to the positions of water content probe arrays, are contained in Figure 4.9g-i. The base of sand arrival is initially continuous in Figure 4.9a but appears to be deepest in the center of the profile. Depth of the reflector is estimated with errors of 8-25% (i.e., at depths from 0.55 m to 0.75 m). The wetting front reflections are, upon irrigation, initially coincident with the ground wave arrival at 0.10 m depth and by 3 to 5 minutes are visible as separate arrivals which increase in depth over time.

The wetting front arrival time observed at each water content probe is plotted as a point on the appropriate trajectory image. Reasonable agreement is seen in between the migrated wetting front arrival depths and wetting front depths observed in probes. The migrated images show the front deeper than probes with a mean discrepancy of 0.08 m. The wetting front arrival is best resolved in Figure 4.9f and g which show a strong similarity between the increasing depth of the wetting front arrival and the observed front in probes. The wetting front arrival increases in depth at an apparent rate of 0.028 m/min at Y = 1.60 m, 0.018 m/min at Y = 2.00 m, and 0.016 m/min at Y = 2.40 m. The mean and median wetting front velocities from Experiment 1 are 0.027 m/min and 0.019 m/min, respectively, and the apparent velocities in the trajectory images are within the observed velocities from water content probes (Chapter 2.3.2, Table 2.3).

An exception to the overestimation of wetting front depth is seen in the trajectory image at Y = 1.60 m, where the wetting front has passed a water content probe at 0.40 m depth after 6.7 minutes, although the wetting front arrival in the GPR image is at only

0.26 m. The wetting front next passes a probe at 0.20 m depth after 10.8 minutes whereas the migrated wetting front arrival is at a depth of 0.38 m. In Figure 4.9h, the wetting front intersects the base of sand at around 22 minutes, though the wetting front is observed in another 0.40 m probe after 28 minutes (not shown). The underestimation of the wetting front depth in the migrated data is likely due to a zone of rapid wetting front propagation observed in both the water content probe and GPR data from a separate experiment performed under the same irrigation conditions. A set of GPR profiles from this experiment in Figures 4.10a-d show the wetting front arrivals consistently increasing in travel time except around X = 1.50 m position, where a much more rapid increase is evident. The wetting front merges with the base of sand arrival at 21 minutes from positions of 1.50 m – 1.70 m, but the arrivals are separated by 5 ns travel time at 2.50 m position. The wetting front is therefore through the soil column at X = 1.50 m and is approximately halfway through the soil column at positions of X = 2.0 m and above. If similar wetting geometry is assumed between the experiments, the wetting front at X = 2.0 m (i.e., the location of the migrated trajectory images) is not advancing as rapidly as inferred from the water content probes at Y = 1.60 m and the wetting front at 6.7 minutes is not as deep in the profiled area as suggested by the probe.

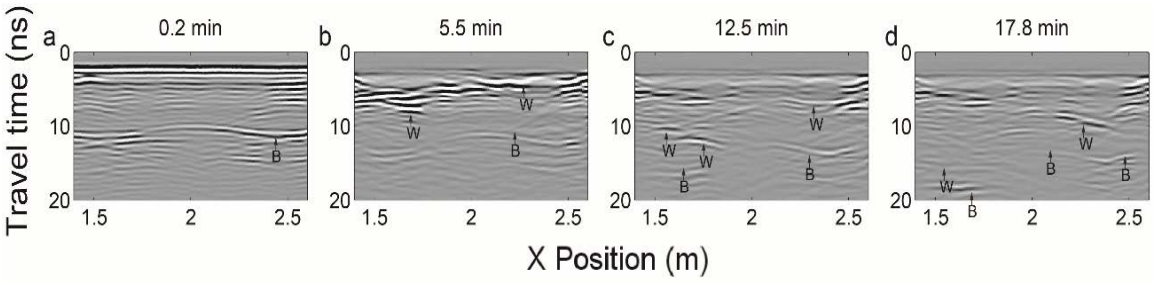

Figure 4.10. COPs from a separate lab experiment under similar applied flux conditions collected along X = 1.70 m in which the wetting front arrival (W) increases in travel time more rapidly at Y = 1.50 m than in other locations, suggesting a zone of rapid water flow not evident from the migrated GPR data.

4.5 Discussion

The results of the velocity analysis and migration of the synthetic data demonstrates that velocity models created from the analysis of single-offset data were generally consistent with the true velocity field and the final migrated images are able to produce a reasonable image of the wetting front. Even under optimal conditions (i.e. migrating with the "true" velocity) the resulting images are not perfect and contain artifacts stemming from the strong velocity contrasts. The wave coverage along the near-vertical edges of the infiltrating bulb generated by a single source, however, is too sparse to properly image the feature, as the simulated wavefield for a source at 2.75 m position in Figure 4.11 illustrates. The emitted wavefront (labeled F_i) at 2.32 ns intersects the bottom edge of the wetted zone located at 2.75 m (Figure 4.11b) and at 3.35 ns a reflected wavelet is seen (labeled F_r, Figure 4.11c). The emitted wavefront passes perpendicular to the vertical portion of the wetted zone the reflected F_r arrives at the ground surface at positions of 2.45 m and below (Figure 4.11e-f). No energy is directly reflected to the source position and is thus not present in the GPR data.

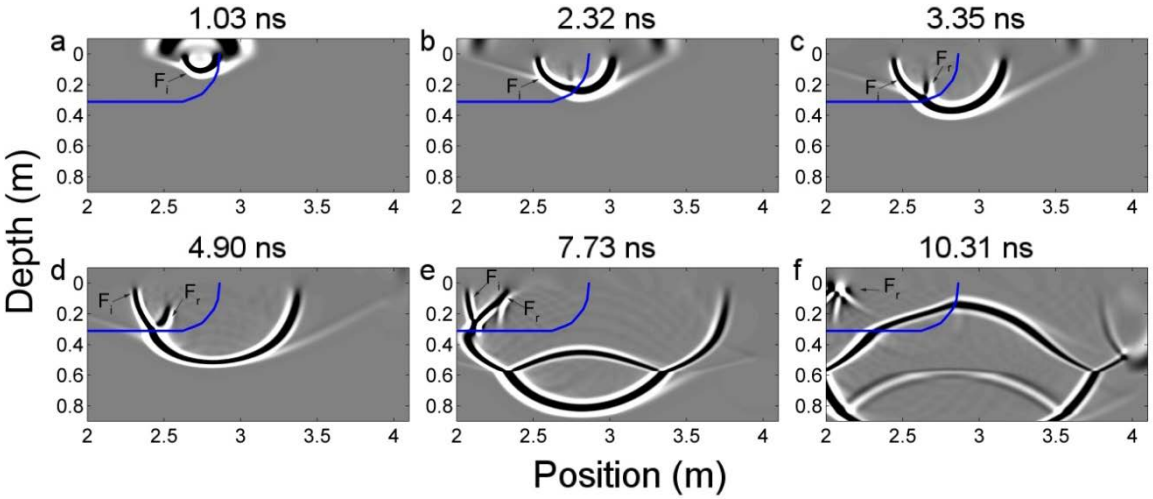

Figure 4.11. The simulated wavefield for a source located close to the edge of the wetted bulb. Energy is directly reflected from the edge of the bulb to distant sources and no primary reflection from the vertical edge of the bulb is generated.

The lack of a primary reflection from the vertical edge of the wetted zone and broadly scattered energy is a limitation which cannot overcome by migration. Even in the ideal case (i.e., where velocity is known exactly as in Figure 4.5) errors in imaging the corner of the wetted zone are apparent and the vertical side is not resolved. The lack of primary reflection coupled with a sharp lateral velocity contrast creates a complex interface which cannot be properly migrated by the methods here. Collecting multi-offset data may provide the wave coverage needed to sample the vertical edge of the bulb. More advanced velocity analysis, such as reflection tomography, coupled with migration could improve the quality of velocity models. Migration techniques which account for energy other than primary reflections, such as reverse-time or full waveform inversion methods, may produce higher quality images, though the trade-off in data collection time may prevent imaging rapid flow events. The results of this simple model suggest that

acquiring images of complex non-uniform flow features with GPR faces significant challenges and may lie beyond the ability of GPR to resolve.

This work investigates flow along a 2D profile, though the results of lab experimented presented in Chapter 2 demonstrate the complicated 3D nature of flow, both in water content probe measurements and particularly in the GPR profiles. The GPR data presented here do not show effects of discrete flow phenomena yet they may be present beyond the profiled area. Thus, the influence of 3D flow effects on the recorded GPR data and efficacy of 2D migration under these conditions remains unknown. The resulting images, however, retain interpretability and show responsiveness to the wetting dynamics. The apparent wetting velocity at Y = 1.60 m derived from the migrated images is higher than the other locations, and the close agreement between GPR and probe velocities at all locations demonstrate that the non-uniformity of the infiltrating front is well described by the GPR data.

4.6 Conclusion

The methods developed in this study are suitable for tracking the propagation of non-uniform wetting fronts with GPR. Here, the data are converted from time to depth domain via depth migration which accounted for the vertical and lateral velocity shifts with reasonable accuracy, resulting in an interpretable image of the propagating wetting front with respect to depth. The trajectory images, in particular, show good agreement of wetting front depths and wetting velocities to independent measurements, demonstrating the sensitivity of the migrated images to the wetting dynamics. Thus, features which may

be unremarkable or not captured in the initial data set (e.g. capillary barriers) and their impact on the flow system can be interpreted from the time lapse data.

The method takes advantage of rapid temporal sampling and a well-characterized subsurface reflector to create the velocity models. These requirements may be met in a variety of situations where appropriate reflectors at known depths are present. Future time-lapse studies may consider adoption of reflection tomography methodology or 3D data collection. The multi-fold data coverage of reflection tomography methods may enable better resolution of the velocity field and, coupled with depth migration, could improve the resolution of GPR images particularly when discrete flow features are present. 3D data collection would capture the complexities of flow and 3D migration methods could properly account for these effects on the GPR data. The increase in time required for collecting these data may limit the practicality of capturing transient flow phenomena.

4.7 Works Cited

2009. Ground Penetrating Radar Theory and Applications. Elsevier Science, 1-526 pp.

Allroggen, N., van Schaik, N., Tronicke, J., 2015. 4D ground-penetrating radar during a plot scale dye tracer experiment. Journal of Applied Geophysics, 118: 139-144. DOI:10.1016/j.jappgeo.2015.04.016

Binley, A., Winship, P., Middleton, R., Pokar, M., West, J., 2001. High-resolution characterization of vadose zone dynamics using cross-borehole radar. Water Resources Research, 37(11): 2639-2652. DOI:10.1029/2000wr000089

Bradford, J.H., 2008. Measuring water content heterogeneity using multifold GPR with reflection tomography. Vadose Zone Journal, 7(1): 184-193. DOI:10.2136/vzj2006.0160

Bradford, J.H., Harper, J.T., 2005. Wave field migration as a tool for estimating spatially continuous radar velocity and water content in glaciers. Geophysical Research Letters, 32(8): 4. DOI:10.1029/2004gl021770

Cassiani, G., Binley, A., 2005. Modeling unsaturated flow in a layered formation under quasi-steady state conditions using geophysical data constraints. Advances in Water Resources, 28(5): 467-477. DOI:10.1016/j.advwatres.2004.12.007

Ferre, P.A., Rudolph, D.L., Kachanoski, R.G., 1996. Spatial averaging of water content by time domain reflectometry: Implications for twin rod probes with and without dielectric coatings. Water Resources Research, 32(2): 271-279. DOI:10.1029/95wr02576

Fisher, E., McMechan, G.A., Annan, A.P., 1992a. ACQUISITION AND PROCESSING OF WIDE-APERTURE GROUND-PENETRATING RADAR DATA. Geophysics, 57(3): 495-504. DOI:10.1190/1.1443265

Fisher, E., McMechan, G.A., Annan, A.P., Cosway, S.W., 1992b. EXAMPLES OF REVERSE-TIME MIGRATION OF SINGLE-CHANNEL, GROUND-PENETRATING RADAR PROFILES. Geophysics, 57(4): 577-586. DOI:10.1190/1.1443271

Gomez-Ortiz, D. et al., 2006. Characterization of volcanic materials using ground penetrating radar: A case study at Teide volcano (Canary Islands, Spain). Journal of Applied Geophysics, 59(1): 63-78. DOI:10.1016/j.jappgeo.2005.07.007

Haarder, E.B., Looms, M.C., Jensen, K.H., Nielsen, L., 2011. Visualizing Unsaturated Flow Phenomena Using High-Resolution Reflection Ground Penetrating Radar. Vadose Zone Journal, 10(1): 84-97. DOI:10.2136/vzj2009.0188

Hendrickx, J.M.H., Flury, M., Xx, 2001. Uniform and preferential flow mechanisms in the vadose zone. Conceptual Models of Flow and Transport in the Fractured Vadose Zone: 149-187.

Irving, J., Knight, R., 2006. Numerical modeling of ground-penetrating radar in 2-D using MATLAB. Computers & Geosciences, 32(9): 1247-1258. DOI:10.1016/j.cageo.2005.11.006

Looms, M.C., Jensen, K.H., Binley, A., Nielsen, L., 2008. Monitoring unsaturated flow and transport using cross-borehole geophysical methods. Vadose Zone Journal, 7(1): 227-237. DOI:10.2136/vzj2006.0129

Neal, A., Roberts, C.L., 2001. Internal structure of a trough blowout, determined from migrated ground-penetrating radar profiles. Sedimentology, 48(4): 791-810. DOI:10.1046/j.1365-3091.2001.00382.x

Simunek, J., Sejna, M., van Genuchten, M.T., 1999 The Hydrus-2D software package for simulating two-dimensional movement of water, heat, and multiple solutes in variably saturated media. Version 2.0. International Ground Water Modeling Center, Colorado School of Mines, Golden, Colorado, pp. 251.

Steelman, C.M., Endres, A.L., 2012. Assessing vertical soil moisture dynamics using multi-frequency GPR common-midpoint soundings. Journal of Hydrology, 436: 51-66. DOI:10.1016/j.jhydrol.2012.02.041

Steelman, C.M., Endres, A.L., Jones, J.P., 2012. High-resolution ground-penetrating radar monitoring of soil moisture dynamics: Field results, interpretation, and comparison with unsaturated flow model. Water Resources Research, 48: 17. DOI:10.1029/2011wr011414

Stoffa, P.L., Fokkema, J.T., Freire, R.M.D., Kessinger, W.P., 1990. SPLIT-STEP FOURIER MIGRATION. Geophysics, 55(4): 410-421. DOI:10.1190/1.1442850

Truss, S., Grasmueck, M., Vega, S., Viggiano, D.A., 2007. Imaging rainfall drainage within the Miami oolitic limestone using high-resolution time-lapse ground-penetrating radar. Water Resources Research, 43(3): 15. DOI:10.1029/2005wr004395

Yilmaz, O., 2001. Seismic Data Analysis: Processing, Inversion, and Interpretation of Seismic Data. Society of Exploration Geophysicists, Tulsa, OK, 2065 pp.

CHAPTER 5
CONCLUSIONS

This thesis investigated the ability of time-lapse ground penetrating radar (TLGPR) to monitor lab-scale forced infiltration events for capturing evidence of non-uniform and preferential flow phenomena directly from arrivals in the GPR images while simultaneously characterizing parameters of the flow system, such as bulk water content and rates of wetting front movement. This was accomplished with the aid of migration processing techniques to improve the quality of GPR images for identification and tracking of transient arrivals related to wetting in the soil. A novel method was developed to characterize the 2D velocity structure of a soil and used to migrate the GPR images. This method incorporates traditional multi-offset measurements to characterize the depth to a potentially unknown static reflector and root mean square (RMS) velocity above the reflector with incremental changes in travel time to the static reflector and a transient reflector (i.e. the wetting front) determined from constant offset profiles to determine incremental changes in velocity above and below the transient arrival.

The arrivals in constant offset profiles collected from Experiment 1 are interpreted to show abundant evidence of non-uniform wetting features. The presence of diffraction hyperbolas during wetting indicates that the wetting front did not advance uniformly and was split into discrete lobes or channels, at least for some time. The profiles presented contain these transient hyperbolas and suggest both vertically and horizontally discrete flow occurred during the experiment. In particular, collecting perpendicular profiles helped to identify and track these arrivals through the 3D environment. The flow was

observed to bypass a large part of the soil matrix during the experiments and supports the interpretation of diffraction hyperbolas as discrete flow features.

Continuation of these data collection methods for identification of preferential flow could incorporate dye-staining experiments with the GPR data collection to tie specific arrivals in GPR profiles with the true wetting pattern. The vadose zone analog used in these experiments is an excellent environment for this type of work as irrigation experiments can be easily repeated and supporting sensors can be installed to gather comprehensive data about the flow regime. It also enables use of engineered structures which will induce particular types of preferential flow to better understand how they will be manifest in GPR data.

The 2D migration workflow presented herein was evaluated to determine whether it could improve the interpration of flow phenomena and quantitatively describe changes in the flow system. The migrated GPR images presented were moderately successful in creating clear and accurate images of an infiltrating front. The best results were obtained from the simulated data, which showed that the analysis could produce images of similar quality to the “ideal” case where the velocity structure was known perfectly. The wetting front depth was subject to errors in depth up to 33%, but the estimated wetting front velocity of 0.018 m/min was very near the true rate of 0.02 m/min. A reasonable result was created using the empirical data, though the complexity of even this simple lab environment results in more complicated images. Errors in depth to the static reflector and wetting front (estimated from water content probes) were up to 25%, similar to the numerical results. However, a similarly good agreement in the wetting front movement

rate was found, with rates of 0.016 to 0.028 m/min similar to the median observed in water content probes of 0.019 m/in. This suggests the velocity analysis methods may be subject to errors at a specific time, particularly due to challenges in picking the wetting front arrival in the radar data, but that the time-lapse velocity tracking is responsive to the changing system. This demonstrates that there is value in continued research into applications of migration techniques for unsaturated flow characterization, determination of soil flow parameters, and studies of preferential flow.

The single-offset velocity analysis method developed herein was used to determine the bulk water content of the soil and compared to estimates from multi-offset GPR data and a volume-weighted average of water content probes. The single-offset estimates were much closer to the water content probes than the multi-offset estimates, with errors of 3.4% to 29.4% but consistently around 10%. The single-offset estimate, due to it's averaging across the irrigated area, provides a clear and consistent trend over the experiment and had errors generally around 10% vol/vol (range from 3.4% to 29.4%). The multi-offset analysis shows very noisy estimates due to the challenge of picking the wetting front arrival in larger offsets. The mean of multi-offset estimates does little to reduce the noise. Whether the single-offset method provides better estimates than a dense multi-offset sampling (i.e. a line of CMPs with center points at the same spatial interval as the COPs) is not possible to deduce from this limited data, it does support the benefit to single-offset sampling as the time required to capture multi-offset data is significantly higher and potentially not possible with rapid flow as in these experiments. Future work can apply the methods developed in this thesis to additional simulations of various flow

regimes to better characterize the limitations and conditions where it can best be applied. This would also include simulations of different wavelength GPR to determine whether the transient arrivals from wetting can be successfully picked and tracked with lower or higher frequency antennas. These experiments demonstrate that it is possible to quantify changes in bulk water content within the soil while simultaneously capturing wetting parameters which can be used to fit flow models, given that there is a continuous reflecting interface. Geologic scenarios where this can be expected are when a geologic contact is present, a change in depositional environment, sediment size or sorting, or potentially an engineered interface.

The migration algorithm used during this analysis was selected for its ability to account for lateral velocity change.

A significant limitation to this work is the three-dimensional non-uniformity of the flow system which was beyond the scope of the analysis. It was observed in the empirical experiment, and future work requires evaluation of true 3D monitoring and analysis method to characterize unsaturated flow. This work would significantly benefit from an automated antenna positioning system similar to the gantry in these experiments. It is critical to accurately and quickly place the antennas, enabling repeated time-lapse sampling of a rapidly changing flow system on the order of seconds to minutes, and enabled the TLGPR data collection presented here. Future development of this system could incorporate additional antennas for true multi-fold data collection. The analysis of wavefield patterns in Chapter 4 demonstrated that single-offset data collection geometry was not adequate to record the arrival of a direct reflection from the near-vertical edge of

the wetted zone. However, with multiple receiving antennas there is a possibility to record these signals and, consequently, perform migration processing technique to properly locate the energy within the subsurface and produce a coherent image of the wetted zone. There is a wealth of future research in combining 3D monitoring and migration analysis with multi-fold data collection to evaluate the potential success of GPR to image and characterize unsaturated flow processes.